McNeill, L.C., Dugan, B., Petronotis, K.E., and the Expedition 362 Scientists
Proceedings of the International Ocean Discovery Program Volume 362
publications.iodp.org

https://doi.org/10.14379/iodp.proc.362.102.2017

Expedition 362 methods[1]

L.C. McNeill, B. Dugan, K.E. Petronotis, J. Backman, S. Bourlange, F. Chemale, W. Chen, T.A. Colson, M.C.G. Frederik, G. Guèrin, M. Hamahashi, T. Henstock, B.M. House, A. Hüpers, T.N. Jeppson, S. Kachovich, A.R. Kenigsberg, M. Kuranaga, S. Kutterolf, K.L. Milliken, F.L. Mitchison, H. Mukoyoshi, N. Nair, S. Owari, K.T. Pickering, H.F.A. Pouderoux, S. Yehua, I. Song, M.E. Torres, P. Vannucchi, P.J. Vrolijk, T. Yang, and X. Zhao[2]

Keywords: International Ocean Discovery Program, IODP, *JOIDES Resolution*, Expedition 362, Site U1480, Site U1481, Sumatra, Sumatra subduction zone, Sunda subduction zone, Andaman-Nicobar Islands, Wharton Basin, Indo-Australian plate, Bengal Fan, Nicobar Fan, Himalaya, Ninetyeast Ridge, Sumatra-Andaman 2004 earthquake, shallow seismogenic slip, décollement, megathrust, tsunami, forearc, Neogene, late Miocene, Late Cretaceous, subduction input sediment, diagenesis, sediment gravity flow, pelagic, oceanic crust, volcanic ash, mud, clay, silt, sand, siliciclastic, calcareous ooze, chalk

Contents

Introduction

This section provides an overview of operations, depth conventions, core handling, curatorial procedures, and analyses performed on the R/V *JOIDES Resolution* during International Ocean Discovery Program (IODP) Expedition 362. This information will help the reader understand the basis of our shipboard observations and preliminary interpretations. It will also enable interested investigators to identify data and to select samples for further study. The information presented here concerns shipboard operations and analyses described in the two site chapters.

Site locations

GPS coordinates from precruise site surveys were used to position the vessel at Expedition 362 sites. A SyQwest Bathy 2010 CHIRP subbottom profiler was used to monitor seafloor depth on the approach to each site to confirm the depth estimates from precruise surveys. Once the vessel was positioned at a site, the thrusters were lowered and a positioning beacon was dropped to the seafloor. Dynamic positioning control of the vessel uses navigational input from the GPS system and triangulation to the seafloor beacon, weighted by the estimated positional accuracy. The final hole position is the mean position calculated from the GPS data collected over a significant portion of the time during which the hole was occupied.

Drilling operations

The advanced piston corer (APC), half-length advanced piston corer (HLAPC), extended core barrel (XCB), and rotary core barrel (RCB) systems were used during Expedition 362.

The APC and HLAPC systems cut soft-sediment cores with minimal coring disturbance relative to other IODP coring systems. After the APC/HLAPC core barrel is lowered through the drill pipe and lands above the bit, the drill pipe is pressured up until the two shear pins that hold the inner barrel attached to the outer barrel fail. The inner barrel then advances into the formation and cuts the core (Figure **F1**). The driller can detect a successful cut, or "full stroke," by observing the pressure gauge on the rig floor because the excess pressure accumulated prior to the stroke drops rapidly.

APC refusal is conventionally defined in one of two ways: (1) the piston fails to achieve a complete stroke (as determined from the pump pressure and recovery reading) because the formation is too hard, or (2) excessive force (>60,000 lb) is required to pull the core barrel out of the formation. When a full stroke could not be achieved, one or more additional attempts were typically made, and each time the bit was advanced by the length of the core barrel. Note that this resulted in a nominal recovery of ~100% based on the assumption that the barrel penetrated the formation by the length of core recovered. During Expedition 362, there were a number of partial strokes that returned nearly full core liners. In these cases,

[1] McNeill, L.C., Dugan, B., Petronotis, K.E., Backman, J., Bourlange, S., Chemale, F., Chen, W., Colson, T.A., Frederik, M.C.G., Guèrin, G., Hamahashi, M., Henstock, T., House, B.M., Hüpers, A., Jeppson, T.N., Kachovich, S., Kenigsberg, A.R., Kuranaga, M., Kutterolf, S., Milliken, K.L., Mitchison, F.L., Mukoyoshi, H., Nair, N., Owari, S., Pickering, K.T., Pouderoux, H.F.A., Yehua, S., Song, I., Torres, M.E., Vannucchi, P., Vrolijk, P.J., Yang, T., and Zhao, X., 2017. Expedition 362 methods. *In* McNeill, L.C., Dugan, B., Petronotis, K.E., and the Expedition 362 Scientists, *Sumatra Subduction Zone*. Proceedings of the International Ocean Discovery Program, 362: College Station, TX (International Ocean Discovery Program). https://doi.org/10.14379/iodp.proc.362.102.2017

[2] **Expedition 362 Scientists' addresses.**

MS 362-102: Published 6 October 2017

Figure F1. APC system used during Expedition 362. ID = inner diameter.

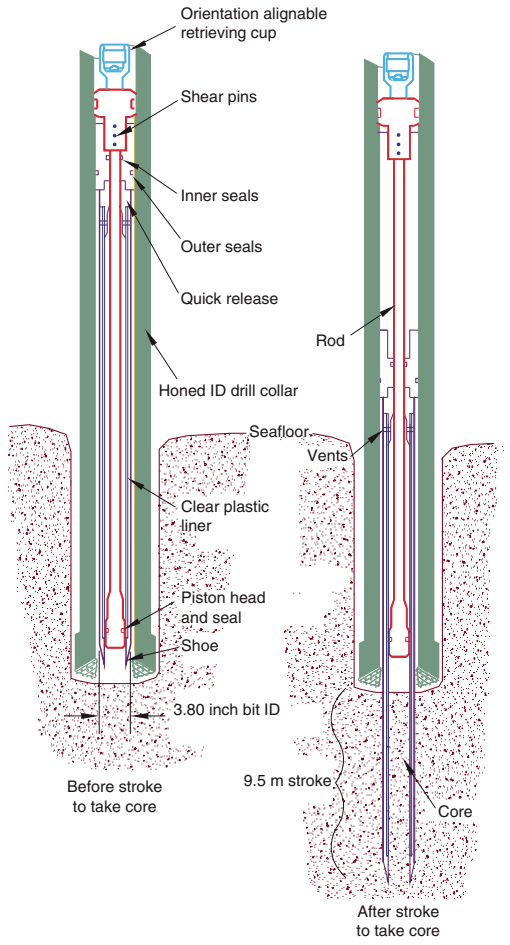

Figure F2. XCB system used during Expedition 362.

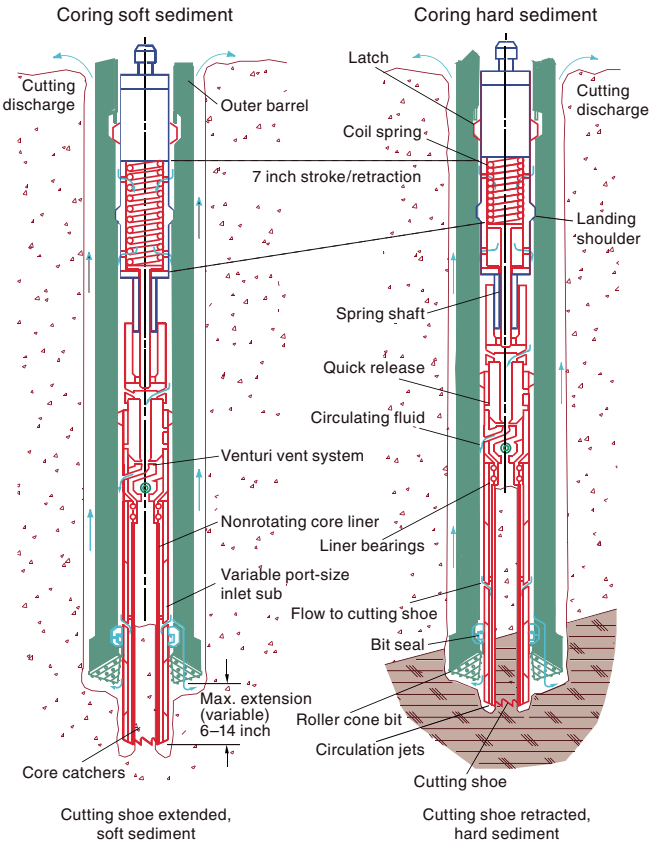

the partial strokes were not viewed as refusal and additional APC cores were attempted. When a full or partial stroke was achieved but excessive force could not retrieve the barrel, the core barrel was "drilled over," meaning that after the inner core barrel was successfully shot into the formation the drill bit was advanced to total depth to free the APC barrel.

The standard APC system uses a 9.5 m long core barrel, whereas the HLAPC system uses a 4.7 m long core barrel. In most instances, the HLAPC was deployed after the standard APC consistently had <50% recovery. During use of the HLAPC, the same criteria were applied in terms of refusal as for the APC system. Use of the HLAPC allowed for significantly greater APC sampling depths to be attained than would have otherwise been possible.

When the HLAPC system had insufficient recovery, the XCB system was typically used. In our case, however, the XCB system was not able to recover the unconsolidated sands encountered at depths where the XCB would normally be used. To recover some amount of sediment, we employed a hybrid strategy of advancing 9.7 m where the upper 4.7 m was cored with the HLAPC system and the lower 5 m was drilled without recovery. This allowed us to advance 9.7 m in a similar amount of time as it would have taken to recover an XCB core, and to also comply with the IODP safety protocol.

The XCB system was used to advance the hole when HLAPC refusal occurred before the target depth was reached, or when drilling conditions required it. The XCB is a rotary system with a small cutting shoe that extends below the large rotary APC/XCB bit (Figure F2). The smaller bit can cut a semi-indurated core with less torque and fluid circulation than the main bit, potentially improving recovery. The XCB cutting shoe extends ~30.5 cm ahead of the main bit in soft sediments but is allowed to retract into the main bit when hard formations are encountered. XCB core barrels are 9.5 m long.

The bottom-hole assembly (BHA) used for APC and XCB coring was composed of an 11 7/16 inch (~29.05 cm) drill bit, a bit sub, a seal bore drill collar, a landing saver sub, a modified top sub, a modified head sub, five 8¼ inch control length drill collars, a tapered drill collar, two stands of 5½ inch transition drill pipe, and a crossover sub to the drill pipe that extended to the surface.

The RCB system is a rotary system designed to recover firm to hard sediments and igneous basement. The BHA, including the bit and outer core barrel, is rotated with the drill string while bearings allow the inner core barrel to remain stationary (Figure F3). RCB core barrels are 9.5 m long.

The RCB BHA included a 9⅞ inch drill bit, a bit sub, an outer core barrel, a modified top sub, a modified head sub, a variable number of 8¼ inch control length drill collars, a tapered drill collar, two stands of 5½ inch drill pipe, and a crossover sub to the drill pipe that extended to the surface.

Nonmagnetic core barrels were used in APC, HLAPC, and RCB deployments. APC cores were oriented with the Icefield MI-5 and FlexIT core orientation tools when coring conditions allowed. Formation temperature measurements were taken with the advanced piston corer temperature tool (APCT-3), and one deployment was attempted with the temperature dual-pressure (T2P) tool (see **Downhole measurements**). Information on recovered cores, drilled intervals, tool deployments, and related information are provided in the Operations section of each site chapter.

Figure F3. RCB system used during expedition 362. OD = outer diameter.

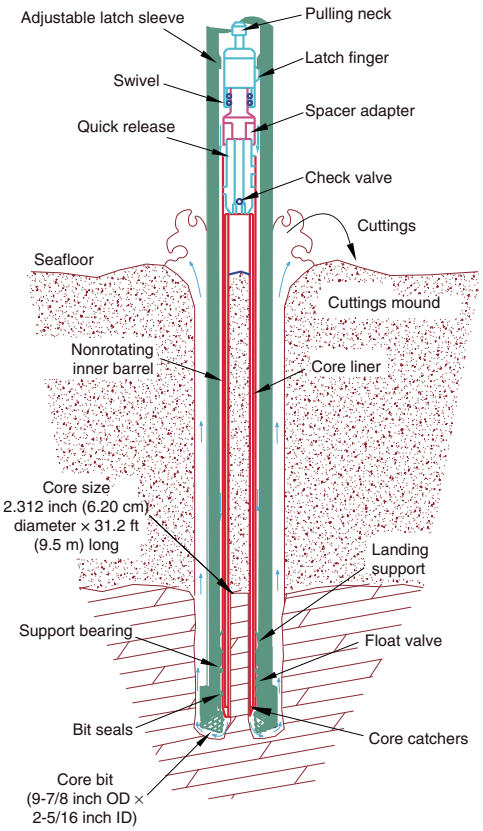

IODP depth conventions

The primary depth scales used are based on the length of the drill string deployed (e.g., drilling depth below rig floor [DRF] and drilling depth below seafloor [DSF]), the length of core recovered (e.g., core depth below seafloor [CSF] and core composite depth below seafloor [CCSF]), and the length of logging wireline deployed (e.g., wireline log depth below rig floor and wireline log depth below seafloor) (see IODP Depth Scales Terminology at **http://www.iodp.org/policies-and-guidelines**). In cases where multiple logging passes are made, wireline log depths are mapped to one reference pass, creating the wireline log matched depth below seafloor. All depth units are in meters. The relationship between scales is defined either by protocol, such as the rules for computation of CSF from DSF, or by user-defined correlations, such as core-to-log correlation. The distinction in nomenclature should keep the reader aware that a nominal depth value in different depth scales usually does not refer to the exact same depth below seafloor.

Depths of cored intervals are measured from the drill floor based on the length of drill pipe deployed beneath the rig floor (DRF scale). The depth of the cored interval is referenced to the seafloor (DSF scale) by subtracting the seafloor depth of the hole from the DRF depth of that interval. Standard depths of cores in meters below the seafloor (CSF-A scale) are determined based on the assumption that (1) the top depth of a recovered core corresponds to the top depth of its cored interval (at the DSF scale) and (2) the recovered material is a contiguous section even if core segments are separated by voids when recovered. Standard depths of samples and associated measurements (CSF-A scale) are calculated by adding the offset of the sample or measurement from the top of its section and the lengths of all higher sections in the core, to the top depth of the core.

If a core has <100% recovery, for curation purposes all cored material is assumed to originate from the top of the drilled interval as a continuous section. In addition, voids in the core are closed by pushing core segments together, if possible, during core handling at the core receiving area. Therefore, the true depth interval within the cored interval is unknown. This should be considered a sampling uncertainty in age-depth analysis or in correlation of core data with downhole logging data.

When core recovery is >100% (the length of the recovered core exceeds that of the cored interval), the CSF depth of a sample or measurement taken from the bottom of a core will be deeper than that of a sample or measurement taken from the top of the subsequent core (i.e., the data associated with the two core intervals overlap at the CSF-A scale). This can happen when a soft to semisoft sediment core recovered from below the seafloor expands upon recovery, for example due to release of gas or removal of overburden pressure (typically by a few percent to as much as 15%). Therefore, a stratigraphic interval may not have the same nominal depth at the DSF and CSF scales in the same hole.

During Expedition 362, unless otherwise noted, depths below rig floor are reported as meters below rig floor (mbrf), core depths below seafloor are reported as meters below seafloor (mbsf), and downhole wireline depths are reported as mbsf. A core composite depth scale (CCSF) was constructed for Site U1480 to mitigate coring gap problems and to create a continuous stratigraphic record for the upper ~30 m. Core depths from adjacent holes were vertically shifted using core-based physical property data, verified with core photos. This process produced a CCSF depth scale, which is defined in **Core-log-seismic integration** in the Site U1480 chapter (McNeill et al., 2017). In **Biostratigraphy** in the Site U1480 chapter (McNeill et al., 2017), core composite depths are reported as meters composite depth (mcd).

Curatorial procedures and sample depth calculations

Numbering of sites, holes, cores, and samples followed standard IODP procedure. A full curatorial identifier for a sample consists of the following information: expedition, site, hole, core number, core type, section number, section half, piece number (hard rocks only), and interval in centimeters measured from the top of the core section. For example, a sample identification of "362-U1480E-2H-5W, 80–85 cm" indicates a 5 cm sample removed from the interval between 80 and 85 cm below the top of Section 5 (working half) of Core 2 ("H" designates that this core was taken with the APC system) of Hole E at Site U1480 during Expedition 362 (Figure **F4**). The "U" preceding the hole number indicates the hole was drilled by the U.S. platform, the *JOIDES Resolution*. The drilling system used to obtain a core is designated in the sample identifiers as follows: H = APC, F = HLAPC, R = RCB, and X = XCB. Integers are used to denote the "core" type of drilled intervals (e.g., a drilled interval between Cores 2H and 4H would be denoted by Core 31).

Core handling and analysis

Sediment

When the core barrel reached the rig floor, the core catcher from the bottom of the core was removed and a whole-round sample was extracted for paleontologic analysis. Next, the sediment core was extracted from the core barrel in its plastic liner. The liner

Figure F4. IODP convention for naming sites, holes, cores, sections, and samples.

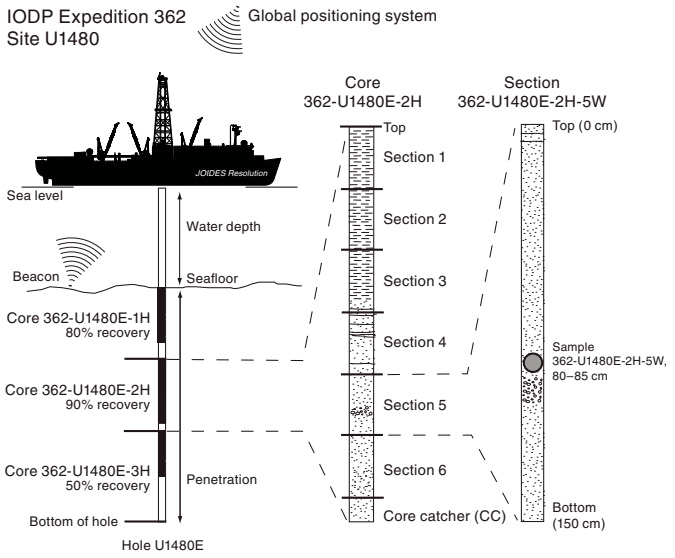

was carried from the rig floor to the core receiving area on the catwalk outside the core laboratory, where it was split into ~1.5 m sections.

Once the core was cut into sections, whole-round samples were taken for interstitial water chemical analyses and for postcruise mechanical and physical property experiments. Syringe samples were taken for headspace gas analyses according to the IODP hydrocarbon safety monitoring protocol. Once all catwalk samples were collected, blue (uphole direction) and clear (downhole direction) liner caps were glued with acetone onto the cut liner sections. Yellow caps were used to denote missing intervals where whole-round samples were removed. Rhizon sampling was also conducted in one hole.

The core sections were placed in a core rack in the laboratory. When the core sections reached equilibrium with laboratory temperature (typically after 2 h), they were run through the Whole-Round Multisensor Logger (WRMSL) for *P*-wave velocity (*P*-wave logger [PWL]), magnetic susceptibility, and gamma ray attenuation (GRA) bulk density (see **Physical properties**). The core sections were also run through the Natural Gamma Radiation Logger (NGRL), and thermal conductivity measurements were typically taken once per core when the material was suitable.

The core sections were then split lengthwise from bottom to top into working and archive halves. Investigators should note that older material can be transported upward on the split face of each section during splitting.

The working half of each core was described by the structural geologists. Discrete samples were then taken for moisture and density (MAD) and paleomagnetic analyses, for shipboard analyses such as X-ray diffraction (XRD) and carbonate, and for shore-based studies based on the sampling plan agreed upon by the science party and shipboard curator. Sampling of certain intervals was delayed until personal samples could be prioritized. Samples were not collected when the lithology was unsuitable or the core was severely deformed. Discrete strength and *P*-wave velocity measurements were made when the lithology permitted.

The archive half of each core was scanned on the Section Half Imaging Logger (SHIL) and measured for point magnetic susceptibility (MSP) and reflectance spectroscopy and colorimetry (RSC) on the Section Half Multisensor Logger (SHMSL). Labeled foam pieces were used to denote missing whole-round intervals in the SHIL images. The archive-half sections were then described visually and by means of smear slides for sedimentology. Finally, the magnetization of archive-half sections and working-half discrete pieces was measured with the cryogenic magnetometer and spinner magnetometer.

Hard rock

Pieces were extracted from the core liner on the catwalk or directly from the core barrel on the rig floor. The pieces were pushed to the bottom of 1.5 m liner sections, and the total rock length was measured. The length was entered into the database as "created length" using the SampleMaster application. This number was used to calculate recovery. The liner sections were then transferred to the core splitting room.

Oriented pieces of core were marked on the bottom with a wax pencil to preserve orientation. Adjacent but broken pieces that could be fit together along fractures were curated as single pieces. The structural geologist on shift confirmed piece matches and marked the split line on the pieces, which defined how the pieces were to be cut into two equal halves. The aim was to maximize the expression of dipping structures on the cut face of the core while maintaining representative features in both archive and working halves. A plastic spacer was secured with acetone to the split core liner between individual pieces or reconstructed contiguous groups of subpieces. These spacers can represent substantial intervals of no recovery. The length of each section of core, including spacers, was entered into the database as "curated length," which commonly differs by several centimeters from the length measured on the catwalk. Finally, the depth of each piece in the database was recalculated based on the curated length.

The core sections were placed in a core rack in the laboratory. When the core sections reached equilibrium with laboratory temperature (typically after 2 h), the whole-round core sections were run through the WRMSL (for GRA density and magnetic susceptibility only) and the NGRL (see **Physical properties**).

Each piece of core was split with a diamond-impregnated saw into an archive half and a working half, with the positions of plastic spacers between pieces maintained in both halves. Pieces were numbered sequentially from the top of each section, beginning with the number 1. Separate subpieces within a single piece were assigned the same number but lettered consecutively (e.g., 1A, 1B, etc.). Pieces were labeled only on the outer cylindrical surfaces of the core. If it was evident that an individual piece had not rotated around a horizontal axis during drilling, an arrow pointing to the top of the section was added to the label. The piece's oriented character was recorded in the database using the SampleMaster application.

The working half of each core was first described by the structural geologists. Samples were then taken for thin section preparation and shipboard paleomagnetic and physical properties analyses. The archive half of each core was scanned on the SHIL and measured for MSP and RSC on the SHMSL. Thermal conductivity measurements were made on selected archive-half samples (see **Physical properties**). The archive halves were then described visually for petrology, followed by microscopic description of thin sections taken from the working half. Finally, the magnetization of archive-half sections, archive-half pieces, and discrete samples taken from the working half was measured with the cryogenic magnetometer and spinner magnetometer.

Sampling for shore-based studies was delayed until the end of hard rock coring. Sampling was conducted based on the sampling plan agreed upon by the science party and shipboard curator.

When all steps were completed, cores were wrapped, sealed in plastic tubes, and transferred to cold storage space aboard the ship. At the end of the expedition the cores were sent to storage at the IODP Kochi Core Center in Japan.

Drilling and handling core disturbance

Cores may be significantly disturbed and contain extraneous material as a result of the coring and core handling process (Jutzeler et al., 2014). In formations with loose sand layers, sand from intervals higher in the hole may be washed down by drilling circulation, accumulate at the bottom of the hole, and be sampled with the next core. The uppermost 10–50 cm of each core must therefore be examined critically during description for potential "fall-in." Common coring-induced deformation includes the concave-downward appearance of originally horizontal bedding. Piston action can result in fluidization ("flow-in") at the bottom of APC cores. Retrieval from depth to the surface can result in elastic rebound. Gas that is in solution at depth may become free and drive apart core segments within the liner. When gas content is high, pressure must be relieved for safety reasons before the cores are cut into segments. This is accomplished by drilling holes into the liner, which forces some sediment as well as gas out of the liner. These disturbances are described in each site chapter and graphically indicated on the visual core descriptions.

Authorship of chapters

The separate sections of the site chapters were written by the following scientists (authors are listed in alphabetical order; see **Expedition 362 science party** for contact information):

Background and objectives: Dugan, McNeill, Petronotis
Operations: Midgley, Petronotis
Sedimentology and petrology: Chemale, Kutterolf, Milliken, Mukoyoshi, Pickering, Pouderaux
Structural geology: Hamahashi, Kenigsberg, Shan, Vannucchi, Vrolijk
Biostratigraphy: Backman, Chen, Kachovich, Mitchison
Paleomagnetism: Yang, Zhao
Geochemistry: House, Hüpers, Owari, Torres
Physical properties: Bourlange, Colson, Frederik, Guèrin, Henstock, Jeppson, Kuranaga, Nair, Song
Downhole measurements: Guèrin
Core-log-seismic integration: Henstock

Sedimentology and petrology

This section outlines procedures used to document the composition, texture, and sedimentary structures of the sediment, sedimentary rock, and igneous rock recovered during Expedition 362. For the level of core disturbance, see **Structural geology**. The procedures include visual core description, smear slide and petrographic thin section analysis, digital color imaging, color spectrophotometry, and XRD and carbonate analysis.

Core sections from the archive halves were used for sedimentological and petrographic observation. Sections dominated by unlithified sediment were split using a thin wire held in high tension. The split surface of the archive half was then assessed for quality (e.g., smearing or surface unevenness) and, if necessary, gently scraped with a glass slide. Hard rock was split with a diamond-impregnated saw. After splitting, the archive half was imaged by the SHIL and then analyzed for color reflectance and magnetic susceptibility using the SHMSL (see **Physical properties**). The archive-half section was in some cases reimaged when visibility of sedimentary structures or fabrics improved following treatment of the split core surface. Following imaging, the archive-half sections of the sediment cores were macroscopically described for lithologic and sedimentary features aided by use of a 20× wide-field hand lens and binocular microscope.

Lithostratigraphic units were defined following visual inspection and smear slide analysis, and, where relevant, thin section analysis. Visual inspection of sediments and sedimentary rocks yielded information particularly concerning lithologic variation, color, sedimentary structures, and drilling disturbance, whereas smear slide analysis was used to identify sedimentary constituents including microfossils. For igneous rocks, initial analysis focused on visual inspection where intervals of igneous rock were recognized on the basis of minerals, texture, grain size, color, contacts, chilled margins, and changes in primary and secondary mineralogy. Selected thin sections provided important detailed descriptions of mineral composition, texture, and evidence for alteration. All of the descriptive data were entered into DESClogik (see **IODP use of DESClogik** for details). Based on preliminary visual descriptions and physical property data, samples were taken from the working-half sections to make thin sections and to provide samples for XRD. All descriptions and sample locations were recorded using curated depths and documented on visual core description (VCD) graphic reports (Figures **F5**, **F6**, **F7**).

Visual core descriptions

Principal lithologies

Lithologic description was based on visual core description, supported by smear slide analysis of dominant and minor lithologies, bulk analysis of mineralogy by XRD, and bulk analysis of carbonate content.

The basic lithologic groups used in Expedition 362 core description for sediments and sedimentary rocks were modified from the scheme of Mazullo and Graham (1988) (Figure **F8**). If the sediment contained <50% biogenic debris (calcareous or siliceous), then it was classified as either siliciclastic (implied terrigenous) or volcanogenic, based on whichever nonbiogenic component had greater abundance. Sediment with >50% biogenic debris was classified pelagic, and as either biocalcareous or biosiliceous, based on the biogenic component that was most abundant. Shallow-water (neritic) carbonate sediment was not recovered during this expedition.

All sediment/sedimentary rock samples were classified based on texture (Figure **F9**; see also Shepard, 1954). Siliciclastic sediment/sedimentary rock was classified primarily based on texture alone, with compositional modifiers as appropriate. Components present in amounts of 25%–50% are primary modifiers (e.g., biocalcareous silty clay and tuffaceous silty clay), whereas components of 5%–25% are secondary modifiers (e.g., clayey silt with glauconite). Pelagic sediment was classified as ooze based on the dominant allochem (e.g., biosiliceous ooze and calcareous ooze).

Most of the sediment/sedimentary rock categories shown in Figure **F9** contain >50% particles of <62.5 µm size (silt and clay). When referring to fine-grained sediment or sedimentary rock collectively, the term "mud" (mudstone) is applied. The term "sand" (sandstone) refers to materials with ≥50% sand-size particles. Cases in which sandy sediment or sedimentary rock contains ≥25% silt +

Figure F5. Graphic patterns for sedimentary lithologies encountered during Expedition 362.

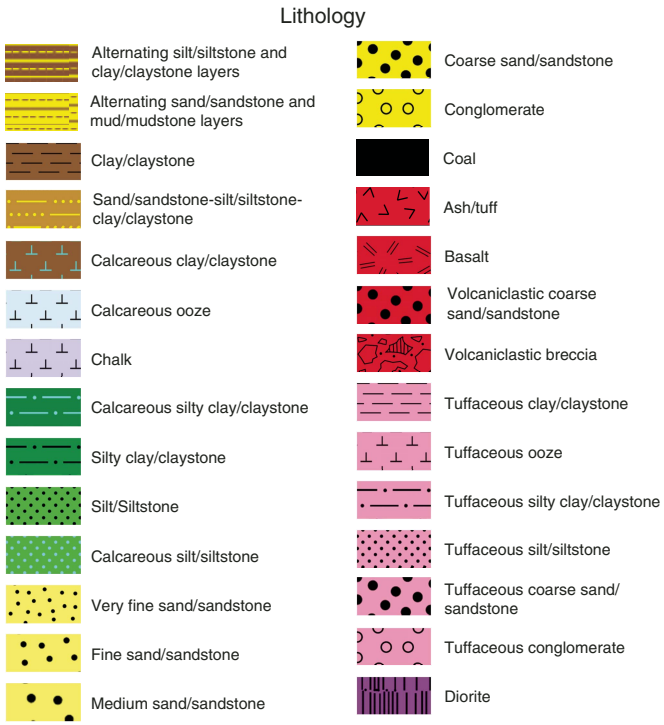

clay, the term "muddy sand" (sandstone) is used to refer to these poorly sorted sands (sandstones), collectively.

All grain size designations followed the conventional Wentworth (1922) scheme as depicted by Folk (1980). Maximum grain size was described based on the terms in the Wentworth grain size classification.

Color was determined qualitatively for core intervals using Munsell Color Charts (Munsell Color Company, Inc., 2000). Visual inspections of the archive-half sections were used to identify compositional and textural elements of the sediment and sedimentary rock, including rock fragments, sedimentary structures, and diagenetic features such as color mottling and the results of element mobility in diagenesis (e.g., manganese oxide segregation).

Sediment and sedimentary rock were classified using an approach that integrated the nature of volcanic particles into the sedimentary descriptive scheme. Sediment and sedimentary rock were divided into four lithologic classes based on composition (types of particles) (Table **T1**):

1. Volcaniclastic sediment and rock of pyroclastic origin with ≥75% volcaniclastic or pyroclastic particles;
2. Tuffaceous/volcaniclastic sediment and rock of sedimentary origin (25%–75% volcaniclastic or pyroclastic particles);
3. Siliciclastic sediment and sedimentary rock with <25% volcaniclastic and tuffaceous particles and <5% biogenic particles; and
4. Pelagic to hemipelagic sediment (rock) with <25% volcaniclastic and tuffaceous particles and ≥5% biogenic particles.

Within each class, the principal lithology name was based on particle size. In addition, appropriate prefixes and suffixes were applied. For example, the prefix tuffaceous was used for the tuffaceous lithologic classes, and prefixes that indicate the dominant biogenic component as determined by microscopic examination were used for pelagic/hemipelagic sediment and sedimentary rock. Suffixes were also used to indicate minor components within each principal lithologic type.

To emphasize the differences in composition of the recovered volcaniclastic sandstones, the rocks were further classified using the scheme of Fisher and Schmincke (1984). In general, coarser grained sedimentary rock (63 µm to 2 mm average grain size) was designated as "sand" where the volcaniclastic components were <25% of the total clasts. Volcaniclastic rocks can be (1) reworked and commonly altered heterogeneous assemblages of volcanic material, including lava, tuff fragments, and compositionally different ash lenses/particles; or (2) fresh or relatively unaltered, compositionally homogeneous, unconsolidated pyroclastic material directly resulting from explosive eruptions on land or effusive/explosive vents on the seafloor. Pyroclasts are composed of volcanogenic material that was fragmented during explosive eruption.

Where there are ≥25% volcaniclasts but <25% pyroclasts, the sediment or sedimentary rock was designated as volcaniclastic sand/sandstone. Where the clast composition is 25%–75% pyroclasts, the sediment/sedimentary rock was classified as tuffaceous sand/sandstone. However, if the clast composition is ≥75% pyroclasts, it was classified using the volcanological terms ash/tuff (<2 mm), lapilli/lapillistone (2–64 mm), bombs, or blocks/pyroclastic breccia/agglomerate (modified after Fischer and Schmincke, 1984).

Breccia-conglomerate is composed of predominantly rounded and/or subrounded clasts (≥50 vol%) and subordinate angular/subangular clasts. Breccia is predominantly composed of angular and subangular clasts (≥50 vol%). The description was refined by indicating whether the fabric is either clast supported or matrix supported. For the equivalent pyroclastic lithologic class the term agglomerate or pyroclastic breccia was used in place of conglomerate and breccia, respectively (Fisher and Schmincke, 1984) (Table **T1**). Depending on grain size, degree of compaction, and lithification, the nomenclature was adjusted accordingly.

Figure F6. Legend for sedimentary and tectonic structures used in all Expedition 362 sediment, sedimentary rock, and igneous rock descriptions as well as identification symbols used to document sample locations that were recorded using curated depths on VCD graphic reports.

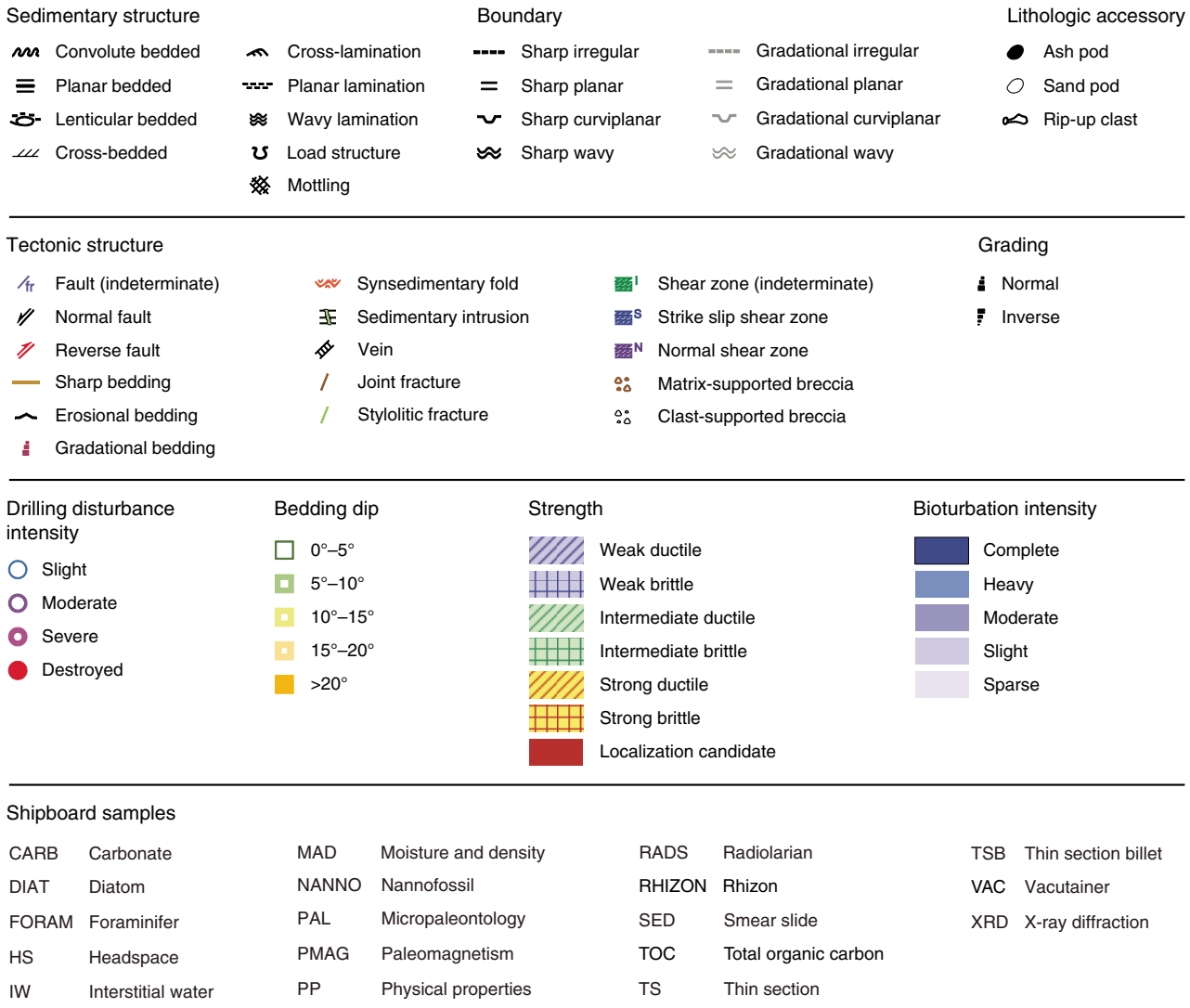

Sedimentary textures, structures, and fabric

For relatively coarse grained material (coarse-grained sand and above), sediment grain size, particle shape, and sorting were determined using the Wentworth scale (Wentworth, 1922). However, for finer grained sediments the textural analysis required inspection at high magnification, which was performed on smear slides and thin sections (see below). The classification of sorting and rounding used the scheme of Folk (1980) (Figure **F10**).

Sedimentary structures described in the cores included bedding, grading (normal and reverse), soft-sediment deformation, bioturbation, and diagenetic effects. Bed thickness (see Ingram, 1954) are defined as follows:

Very thick bedded = >100 cm.
Thick bedded = >30–100 cm.
Medium bedded = >10–30 cm.
Thin bedded = >3–10 cm.
Very thin bedded = 1–3 cm.
Laminae = <1 cm.

The lower contacts of stratification features were described based on geometry (irregular, planar, curviplanar, and wavy), shape or form (sharp, gradational, hardground, and bioturbated), and orientation (subhorizontal, inclined, horizontal, subvertical, and vertical). Sediment grading was described as ungraded, normally graded (fining upward), and inversely graded.

Designation of lithification state followed the somewhat subjective physical property test applied during Expeditions 353 and 354 (Clemens et al., 2016; France-Lanord et al., 2016). If a core of siliciclastic sediment cannot be easily deformed by pushing on it with a finger, it is designated as "-stone," as in claystone, silty claystone, sandstone, and so on. The general term mudstone is used when referring collectively to lithified fine-grained lithologies. Following the same criteria, lithified ash is designated "tuff." Lithified calcareous ooze is designated "chalk." It is important to recognize that lithification state is a transient property that changes across contrasting pressure/temperature/fluid regimes and also evolves as cores dry and age. Most of the sediment encountered during this expedition could be dispersed into its constituent detrital particles for smear

Figure F7. Example of an Expedition 362 VCD sheet for an entire core.

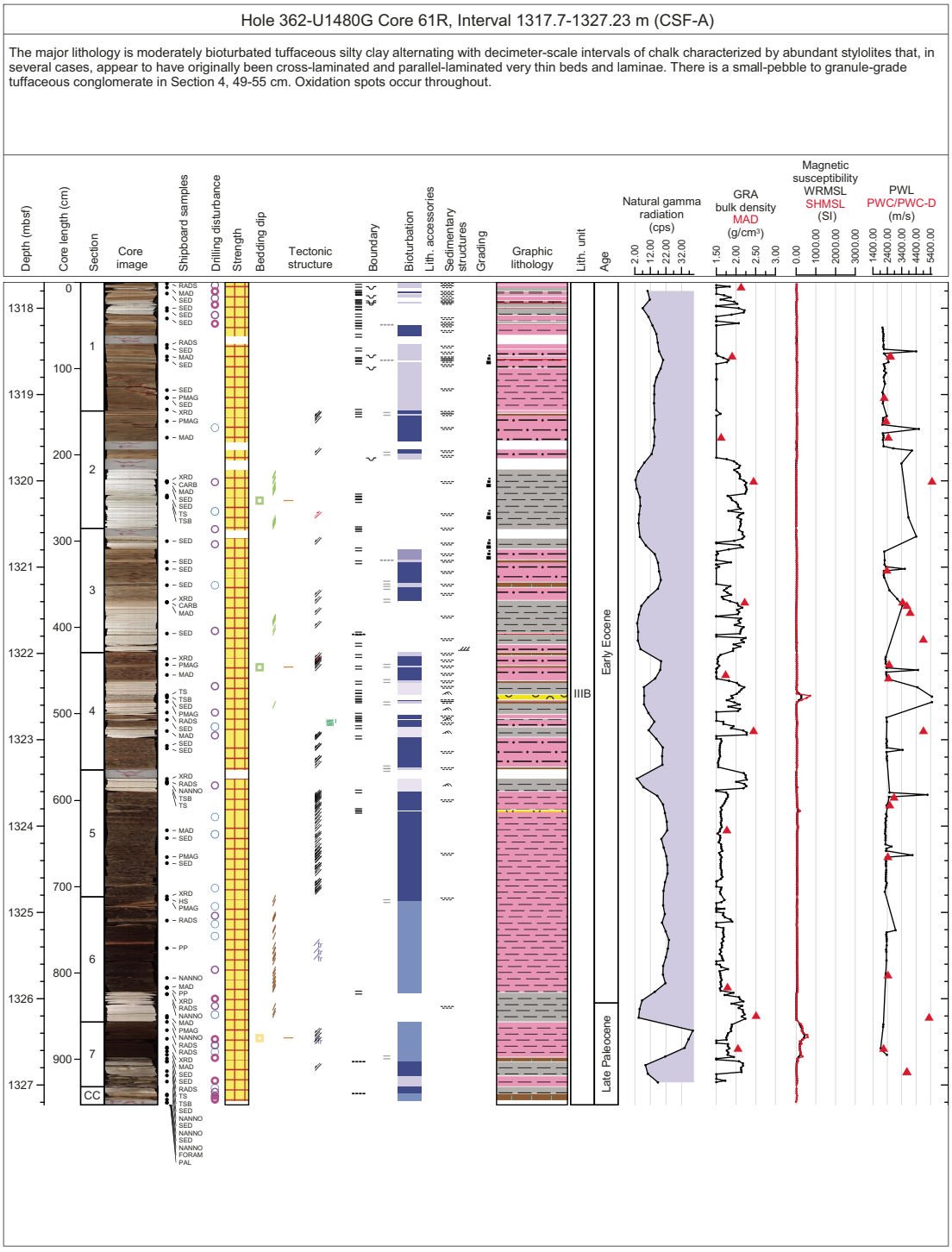

slide preparation. Some, but not all, of the sediment designated as "stone" disaggregated with some difficulty but still sufficiently for smear slide examination.

Bioturbation

Bioturbation intensity in deposits was measured and shown on the VCDs using the semiquantitative ichnofabric index as described by Droser and Bottjer (1986, 1991) and the thickness of the bioturbated section. The indexes refer to the degree of biogenic disruption of primary fabric, such as lamination, and range from 1 for nonbioturbated sediment to 6 for total homogenization:

1 = No bioturbation is recorded; all original sedimentary structures are preserved.
2 = Discrete, isolated trace fossils recorded; up to 10% of original bedding is disturbed.
3 = Approximately 10%–40% of original bedding is disturbed; burrows are generally isolated but locally overlap.

Figure F8. Basic lithologic groups used during Expedition 362 for sedimentary core description. Modified from the scheme of Mazullo and Graham (1988).

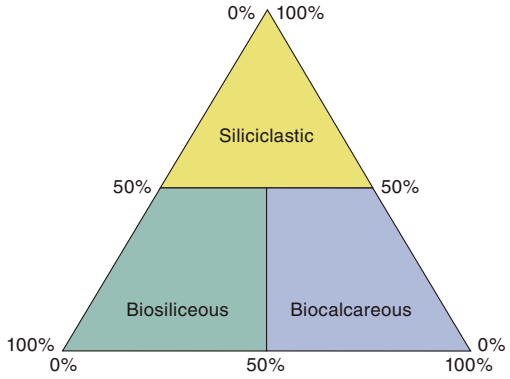

Figure F9. Classification of sediment based on texture only (Shepard, 1954).

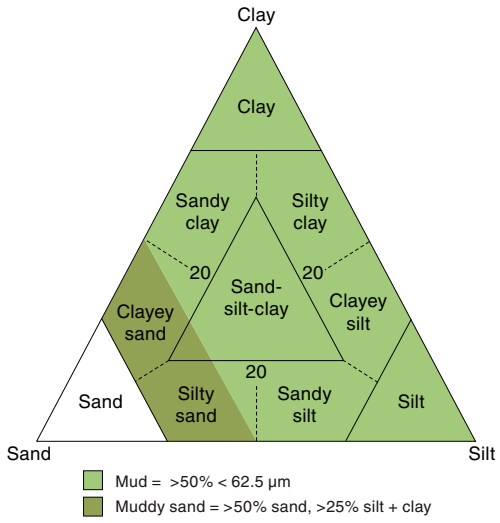

4 = Last vestiges of bedding are discernible; approximately 40%–60% disturbed; burrows overlap and are not always well defined.
5 = Bedding is completely disturbed, but burrows are still discrete in places and the fabric is not mixed.
6 = Bedding is nearly or totally homogenized.

The ichnofabric index in cores was identified with the help of visual comparative charts (Heard et al., 2008, 2014) (Figure **F11**). Any distinct burrows that could be identified as particular ichnotaxa were also recorded. On the VCDs, the six above bioturbation indexes are shown in a separate column as varying color density with the following terms:

1 = no bioturbation (no color).
2 = sparse.
3 = slight.
4 = moderate.
5 = heavy.
6 = complete.

Smear slides and thin sections

Smear slides are useful for identifying and reporting basic sediment attributes, but the results are semiquantitative at best (cf. Marsaglia et al., 2013, 2015). We estimated the abundance of biogenic, volcanogenic, and siliciclastic constituents using a visual comparison chart (Rothwell, 1989), with an emphasis on major lithologies. If a distinct minor lithology was abundant, an additional smear slide was made for that interval.

Visual estimates for normalized percentages of sand, silt, and clay (Terry and Chilingar, 1955) were recorded along with abundance for the individual observed grain types. The component categorization applied to smear slides is shown in Figure **F12**. Smear slides sampled from tephra layers were described using a customized categorization of ash components (Figure **F13**). In smear slides of ash, visual estimates of component abundance were made semiquantitatively and given the following ratings:

R = rare (<1 vol%).
C = common (1–10 vol%).
A = abundant (>10–50 vol%).
D = dominant (>50–80 vol%).
M = major (>80 vol%).

The relative abundance of major components was validated by XRD (see **X-ray diffraction**) and by the absolute weight percent of carbonate determined by coulometric analysis (see **Geochemistry**).

Smear slides were observed in transmitted light using an Axioskop 40A polarizing microscope (Carl Zeiss) equipped with a Flex Spot digital camera.

Description of both sedimentary and igneous lithologies in thin section followed standard protocols as described during Integrated Ocean Drilling Expedition 344 (Harris, et al., 2013). The general techniques described above for smear slide analysis were also applied to thin section description of sedimentary lithologies. The composition and proportion (modal) of primary and secondary (altered/hydrothermal) minerals in the igneous rocks were further defined by using microscopic examination. Textural domains of igneous rocks were defined after MacKenzie et al. (1982).

IODP use of DESClogik

Data for the macroscopic and microscopic descriptions of recovered cores were entered into the IODP Laboratory Information Management System (LIMS) database using the IODP data-entry software DESClogik. DESClogik is a core-description software used to store macroscopic and/or microscopic descriptions of cores. Data were entered in the Sediment tab of the Macroscopic template. Core description data are available through the Descriptive Information LIMS Report (**http://web.iodp.tamu.edu/DESCReport**). A single row in DESClogik defines one descriptive interval, which is commonly one bed but may also be used, for example, to designate marked color variation that may be of diagenetic origin. In addition, the position of each smear slide or petrographic thin section is shown in the VCDs with a sample code of "SED" or "TS," respectively. The VCDs were generated using the plotting software Strater.

X-ray diffraction

Material for XRD was obtained from a 5 cm^3 sample. All samples were vacuum dried, crushed for 3 min with a ball mill, and

Table T1. Classification of volcanic lithologies, Expedition 362. Modified after Fisher and Schmincke (1984). **Download table in .csv format.**

Grain size	Tephra	Tuffite	Volcaniclastic deposit	Epiclastic deposit
> 64 mm	Pyroclastic breccia	Tuffaceous conglomerate	Volcaniclastic conglomerate	Conglomerate
2–64 mm	Lapillistone/lapilli tuff	Tuffaceous breccia	Volcaniclastic gravel	Gravel
64 µm–2 mm	Coarse ash/tuff	Tuffaceous sand	Volcaniclastic sand	Sandstone
2–64 µm	Fine ash/tuff	Tuffaceous silt	Volcaniclastic silt	Siltstone
< 2 µm	Volcanic dust	Tuffaceous clay	Volcaniclastic clay	Claystone
Amount of pyroclasts:	≥75%	<75% to >25%	≤25%	≤25%
Amount of volcaniclastics:			≥25%	≤25%

Figure F10. Classification of sediment sorting and roundness using the scheme of Folk (1980).

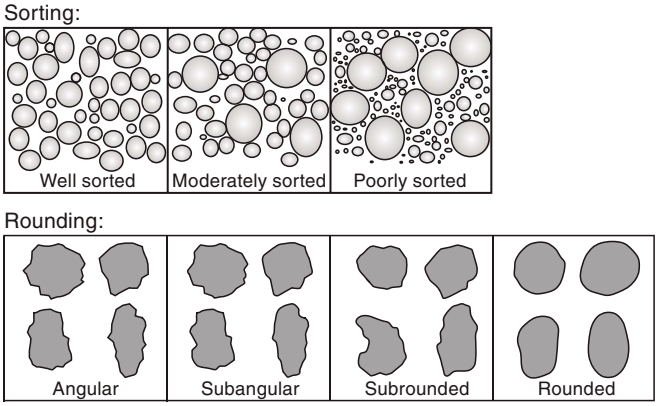

mounted as randomly oriented bulk powders. Routine powder XRD analyses of bulk powders were performed using a Bruker D4 Endeavor diffractometer. XRD instrument settings were as follows:

Generator = 40 kV.
Current = 40 mA.
Tube anode = Cu.
Wavelength = 1.54060 Å (Kα1) and 1.54443 Å (Kα2).
Step spacing = 0.008°2θ.
Scan step time = 0.648 s.
Divergent slit = automatic.
Irradiated length = 10 mm.
Scanning range = 2°–40°2θ.
Spinning = yes.

The principal goal of XRD analysis is to estimate relative weight percentages of total clay minerals (smectite + illite + kaolinite), quartz, plagioclase (representing feldspar), and calcite from the areas of relevant peaks. Peaks used are shown in Table **T2**. Gross peak intensities (counts) were determined using the Bruker software package, DIFFRAC EVA.

Ten XRD standards made from artificial mineral mixtures (Table **T3**) were used to determine simple second-order polynomial regressions describing the relationship between peak intensity and mineral abundance (Table **T4**). Weight percentages of minerals calculated using the regression equations were normalized to 100%. Errors were assessed from the difference between the analyzed standard compositions and compositions calculated from the regressions (Table **T5**). Finally, weight percentages indicated by peak areas of the unknowns were assessed from the regression equations and also normalized to 100%.

Average errors (regression estimates versus true weight percent) of the standard mineral mixtures were

Total clay minerals = 2.6%.
Quartz = 1.1%.
Plagioclase = 1.1%.
Calcite = 2.1%.

The method described is semiquantitative and results should be interpreted with caution. It is important to keep in mind that other phyllosilicates (e.g., micas) may be represented in the value for total clay minerals, especially in silt- and sand-rich materials, and may skew results to higher total clay values because of their strong crystallinity. The contrast in peak response between poorly crystalline minerals at low diffraction angles (e.g., clay minerals) and highly crystalline minerals at higher diffraction angles (e.g., quartz and plagioclase) also impacts these results. Overall, calculated mineral abundances should be regarded as relative percentages within the four-component system of clay minerals + quartz + plagioclase + calcite. The closeness of these estimates to absolute percentages within the total solids depend on the abundance of amorphous solids (e.g., biogenic opal and volcanic glass) and the total of all other minerals that occur in minor or trace quantities.

Sediment-process interpretations

To interpret the likely sediment transport and deposition processes for the range of sediment gravity flows encountered during Expedition 362, we adopted the terminology of Pickering and Hiscott (2015; outlined in Figure **F14**). Conventional usage is adopted for grain settling from suspension fallout to produce hemipelagic and pelagic deposits.

Figure F11. Visual comparative charts used to show the ichnofabric index (a measure of bioturbation intensity) in Expedition 362 cores (from Heard et al., 2008, 2014). Core width is 6.5 cm. Panels 2/6, 3/6, and 4/6 show additional examples of index 6 bioturbation.

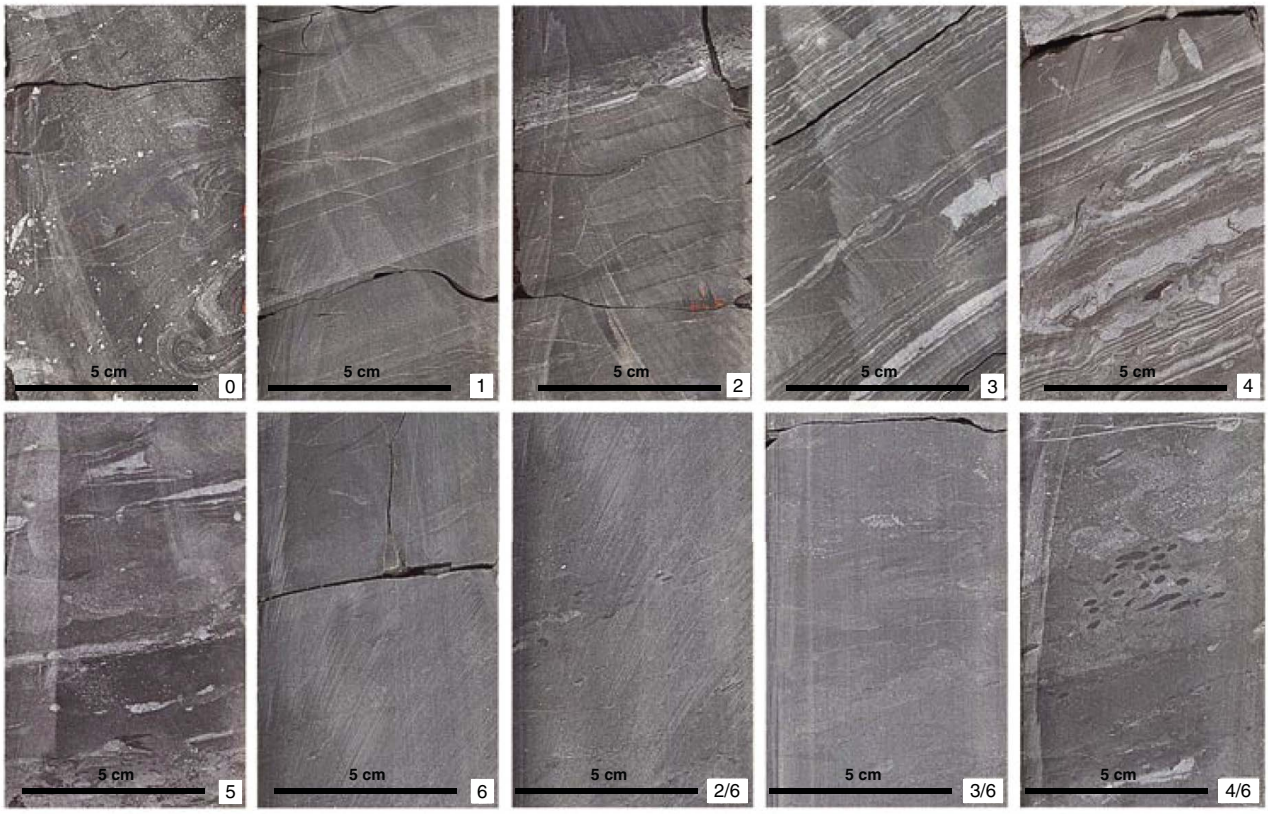

Figure F12. Smear slide component categories for sediment description, Expedition 362.

Sediment Smear Slide / Thin Section Description Sheet

Date:

Expedition: Observer:

Site: Hole: Core: Sect.: Interval:

Sediment Name:

Smear Slide	Thin Section	Coarse Fraction	Grain Mount

Select one and check.

Granular Sediment			Other material	Percent Texture		
Siliciclastic	Volcaniclastic	Pelagic		Sand	Silt	Clay

Select one and check.

Percent	Composition
	Major Siliciclastic Grain Types
	Quartz
	Feldspars
	Clay minerals
	Lithic Grains
	Sedimentary Lithics
	Chert
	Mudstone
	Siltstone/sandstone
	Limestone
	Metamorphic lithic
	Plutonic lithic
	Volcaniclastic Grains
	Vitric fragments
	Clear glass
	Colored glass
	Pumice
	Volcanic lithics
	Felsitic
	Microlite
	Lathwork
	Altered volcanic(palagonite)

Percent	Composition
	Pelagic Grains
	Calcareous
	Nannofossils
	Foraminifers
	Siliceous
	Diatom
	Radiolarian
	Sillicoflagellate
	Sponge Spicule
	Other bioclasts
	Mollusk
	Echinoderm
	Benthic foraminifer
	Other bioclast (specify)
	Other carbonate allochems
	Peloid
	Intraclast
	Silt or sand-size carbonate allochem fragment (unspecified)
	Carbonate mud (apart from nannos)

Percent	Composition
	Minor Grain Types
	Dense minerals[1]
	Micas (biotite, musc, chl)[1]
	Glauconite
	Phosphate (bones, teeth, etc)
	Opaque Grain
	Marine organic matter
	Terrestrial organic matter
	Other (specify):
	Authigenic components
	Pyrite (framboids)
	Pyrite (euhedra)
	Pyrite (grain coating)
	Calcite
	Dolomite
	Zeolites
	Fe/Mn oxide
	Other (specify):

[1] List under remarks if possible

Fill percentage (Total must be 100).

Remarks:

* This form is not designed for shallow water (neritic) carbonate sediments

Figure F13. Smear slide component categories for tephra description, Expedition 362.

Sediment Smear Slide / Tephra Description

Date:

Expedition: Observer:

Site: Hole: Core: Sect.: Interval:

C/A/D/R/T	Vitric Components
	Color
	Glass (pyroclasts)
	Glass (pyroclasts), brown or colored
C/A/D/R/T	Shape
	Blocky
	Cuspate
	Pumiceous
C/A/D/R/T	Vesicle Content/Shape
	Non-vesicular
	Round
	Elliptical
	Elongate
	Tubular
C/A/D/R/T	Crystalline Lithic
	Volcanic lithic abundance (name)

C/A/D/R/T	Crystal components
	Pyroxene
	Amphibole
	Biotite
	Zircon
	Quartz
	Feldspar
	Other*
C/A/D/R/T	Admixed components
	Lithic Fragment
	Clay minerals
	Fossil debris
	Authigenic mineral*

Comments:

Remarks:

Table T2. Characteristic X-ray diffraction peaks for semiquantitative analysis of composite clay minerals, quartz, plagioclase feldspar, and calcite, Expedition 362. **Download table in .csv format.**

Mineral	Reflection	d-value (Å)	Peak limit (°2θ)
Composite clay	Multiple	4.478	19.4–20.4
Quartz	101	3.342	26.3–27.0
Plagioclase	2	3.192	27.4–28.2
Calcite	104	3.035	29.1–29.7

Table T3. Compositions of X-ray diffraction standard mineral mixtures, Expedition 362. **Download table in .csv format.**

Standard	Total clay (%)	Quartz (%)	Plagioclase (%)	Calcite (%)
Mix1	76.8	9.0	7.0	7.2
Mix2	53.5	28.0	8.3	10.2
Mix3	62.4	11.3	12.1	14.2
Mix4	48.8	6.5	26.8	18.0
Mix5	36.8	32.7	7.1	23.4
Mix6	27.9	22.4	15.2	34.5
Mix7	18.9	16.4	12.0	52.8
Mix8	15.3	6.6	5.0	73.2
Mix9	10.6	49.5	39.9	0.0
Mix10	15.1	59.9	19.8	5.2

Table T4. Normalization factors for calculation of relative mineral abundance using bulk powder X-ray diffraction analysis. Weight percent is $[a \times (\text{counts/s})^2] + (b \times \text{counts/s}) + c$, where counts/s is gross intensity of the peaks shown in Table **T2**. **Download table in .csv format.**

Mineral	*a*	*b*	*c*
Total clay	–0.3665	14.078	–52.601
Quartz	–0.0002	0.2726	–1.5266
Plagioclase	0.0092	0.7972	–2.1317
Calcite	0.0072	0.2347	–1.1442

Table T5. Error assessed by comparison of analyzed and calculated compositions of standard mineral mixtures, Expedition 362. **Download table in .csv format.**

	Peak height (gross intensity; counts/s)				Actual mineral content (%)				Calculated mineral content (wt%)			
Sample	Total clay	Quartz	Plagioclase	Calcite	Total clay	Quartz	Plagioclase	Calcite	Total clay	Quartz	Plagioclase	Calcite
Mix1	12.85	41.1	12.1	24.5	76.8	9.00	7.00	7.20	67.8	9.33	8.81	8.93
Mix2	10.32	120.5	12.7	26.8	53.5	28.0	8.30	10.2	53.7	28.4	9.43	11.1
Mix3	13.40	60.9	18.4	39.9	62.4	11.3	12.1	14.2	70.2	14.3	15.6	20.7
Mix4	9.04	33.2	24.8	36.4	48.8	6.50	26.8	18.0	44.7	7.30	23.3	17.9
Mix5	8.59	143.5	11.2	43.5	36.8	32.7	7.10	23.4	41.2	33.5	7.90	23.7
Mix6	7.01	88.3	14.8	50.9	27.9	22.4	15.2	34.5	28.1	21.0	11.7	30.3
Mix7	5.91	64.0	13.8	72.3	18.9	16.4	12.0	52.8	17.8	15.1	10.6	53.3
Mix8	5.19	23.8	7.15	86.6	15.3	6.60	5.00	73.2	10.6	4.83	4.03	71.9
Mix9	5.33	218.0	37.3	8.11	10.60	49.5	39.9	0.00	12.0	48.4	40.3	1.06
Mix10	6.14	289.5	23.4	11.0	15.1	59.9	19.8	5.20	20.0	60.6	21.6	2.31

	Normalized (wt%)				Error (actual – calculated, wt %)			
Sample	Total clay	Quartz	Plagioclase	Calcite	Total clay	Quartz	Plagioclase	Calcite
Mix1	71.5	9.83	9.29	9.41	5.34	–0.83	–2.29	–2.21
Mix2	52.3	27.7	9.19	10.8	1.19	0.30	–0.89	–0.60
Mix3	58.1	11.9	12.9	17.1	4.26	–0.55	–0.81	–2.90
Mix4	48.0	7.84	25.0	19.2	0.83	–1.34	1.80	–1.20
Mix5	38.8	31.5	7.43	22.3	–2.01	1.20	–0.33	1.14
Mix6	30.8	23.0	12.83	33.3	–2.94	–0.63	2.37	1.20
Mix7	18.4	15.6	10.97	55.1	0.52	0.81	1.03	–2.27
Mix8	11.59	5.29	4.42	78.7	3.71	1.31	0.58	–5.50
Mix9	11.8	47.6	39.6	1.04	–1.17	1.94	0.27	–1.04
Mix10	19.1	58.0	20.6	2.21	–4.02	1.87	–0.84	2.99

Figure F14. A. Summary of flow characteristics, typical deposits, and grain-support mechanisms for cohesive and frictional (noncohesive) flows modified from Mulder and Alexander (2001). B. Relative importance of particle-support mechanisms for the four varieties of sediment gravity-flows. Where orange and red symbols are superimposed, the support varies from significant to dominant. From Pickering and Hiscott (2015).

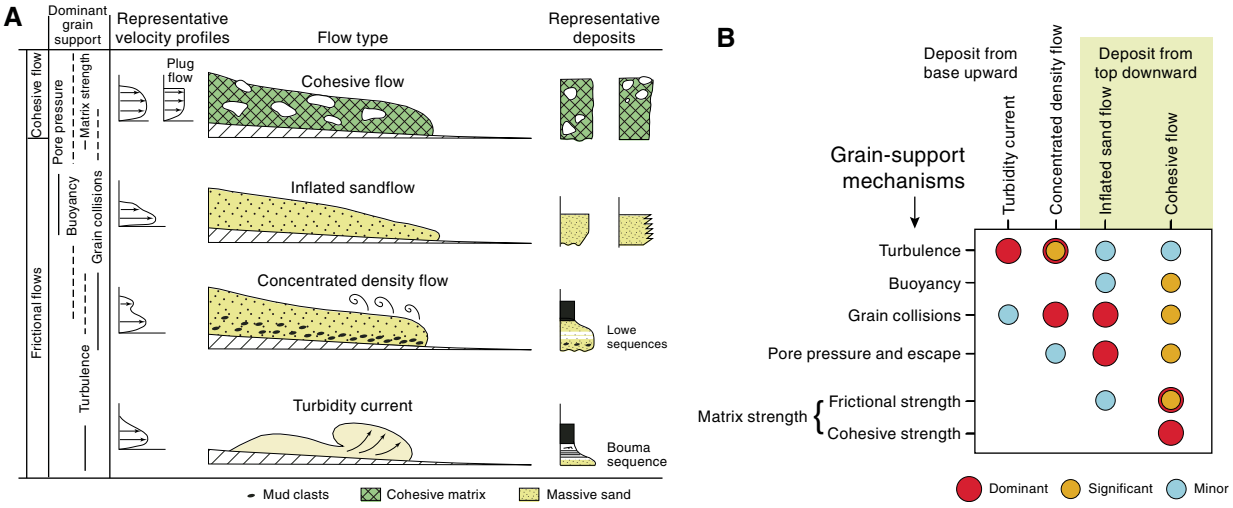

Structural geology

The principal objective of the structural geology team during Expedition 362 was to record deformation structures observed in the core, both natural and drilling induced, and to evaluate from them an early deformation history of the section and the gross strength characteristics and potential deformation mode of the cored section once it encounters the subduction zone. To achieve this objective, we made detailed structural observations following methods used in previous expeditions, but we also complemented these methods with detailed observations of drilling-induced structures. In addition, we compiled and analyzed data from drilling performance to help evaluate first-order strength trends.

The methods for documenting structural features encountered in Expedition 362 cores largely follow those of Expeditions 334, 344, and 352 (Expedition 334 Scientists, 2012; Harris et al., 2013; Reagan et al., 2015). Blenkinsop and Doyle (2010) also provide valuable information on measuring planar structures from core. Structures observed in the split cores were classified and quantified in terms of depth extent, orientation, and sense of displacement. Each structure was recorded manually on a description table sheet (Table **T6**) at the core table. For planar structures, sectional orientation measurements were transformed into dip, strike, and dip direction results using trigonometric transformations applied in an Excel spreadsheet. The resulting orientations defined in a core reference frame were then logged through the DESClogik interface to the LIMS database with all other descriptive information about each structure (see **Visual core descriptions**; Figure **F7**).

In order to address Expedition 362's technical objectives, we added some additional observations and interpretations about drilling disturbance to the structural geology work flow. Our motivation is to make as many inferences about how the cored section might deform once it reaches the Sumatra subduction zone based on the clues provided by natural and drilling-induced deformation. To better interpret the drilling-induced deformation, we calibrated the observed features against a series of drilling parameters (especially weight-on-bit [WOB], rate of penetration [ROP], and torque). The result of this analysis is a first-order speculative interpretation of the strength of the entire cored column, intended as a guide to follow-up studies.

Structural data acquisition and orientation measurements

Structural measurement methods have been important contributions to Ocean Drilling Program (ODP) legs and IODP expeditions undertaken in the past decades, and quantitative measurements have become more common in recent years. The current basis for making quantitative measurements was laid during Expedition 334 (Expedition 334 Scientists, 2012) and further modified during Expedition 344 (Expedition 344 Scientists, 2013) and Expedition 352 (Expedition 352 Scientists, 2015).

We used a plastic protractor for orientation measurements (Figure **F15**). This measurement process was performed on the working half of the split core because it provided greater flexibility in removing—and cutting, if necessary—pieces of the core for structural measurements. Orientations of planar and linear features in cores were determined relative to the core axis, which represents the vertical axis in the core reference frame, and the split line marked on the working half of the split core liner, which represents 0° (and 360°) in the plane perpendicular to the core axis (Figure **F16**). To determine the orientation of a planar structural element, apparent dips were measured in two independent sections in the core reference frame. These two apparent dips were then converted, using an Excel spreadsheet (see 362_Structure_Calculations.xlsx in STRUCTURE in **Supplementary material**) to a plane represented by a dip angle, a strike, and a dip direction (Figure **F17**). One apparent dip is represented by the intersection of the planar feature with the split face of the core and is quantified by measuring the dip direction and angle in the core reference frame (β_1; Figure **F18**). Such a measurement has a trend or azimuth of 90° or 270° and ranges in plunge or dip from 0° to 90° (β_2; Figure **F18**). A second apparent dip is represented by the intersection of the planar feature and a cut or fractured surface at a high angle to the split face of the core. In most cases this surface lies either parallel or perpendicular to the core axis. When parallel, the apparent dip trace trends 0° or 180° and plunges from 0° to 90°; when perpendicular, the trend ranges either from 0° to 90° or from 270° to 360° and plunges 0°. Linear features observed in the cores are systematically associated with planar structures (e.g., a striation on a fault plane), and their orientations were determined by measuring either the rake on the associated

Table T6. Core description categories documented by the structural geology team, Expedition 362. Data were logged in table sheets and entered in DESClogik interface. **Download table in .csv format.**

Structure	Drilling disturbance	Strength
Bedding	Type and form	Interpretation
Sharp	Faulted	Weak
Gradational	Fractured (centerline, petal, core edge, saddle)	Intermediate
Erosional	Brecciated	Strong
	Shear zone	
Fault	Upward-arching beds contacts	Deformation mode
Normal	Mingling and distortion of different beds	Brittle
Reverse	Biscuit (convex, flat, concave)	Ductile
Strike-slip	Soupy	
Indeterminate	Gas expansion	Deformation style
	Core extension	Uniform deformation
Fracture	Void	Localization deformation
Joint	Basal flow-in	
Stylolite	Mid-core flow-in	
	Fall-in	
Fold	Sandy sediment injected between segmented mud units	
Concentric		
Chevron	Intensity	
Box	Slight	
Synsedimentary	Moderate	
Kink	Severe	
	Destroyed	
Shear zone		
Normal	Mechanism	
Reverse	Brittle	
Strike-slip	Ductile	
Indeterminate	Indeterminate	
Deformation band		
Shear band		
Cataclastic		
Riedel		
S-C		
Compaction		
Other structural feature		
Foliation		
Vein		
Sedimentary dike		
Matrix-supported breccia		
Clast-supported breccia		
Apparent offset		
Slickenlines		
Structural geometry		
Planar		
Curved		
Wavy		
Anastomosing		
Polygonal		
Broad		
Closed		
Open		
Overturned		
Tight		
Upright		
Breccia clast size		
Uniform		
Variable		

Figure F15. Protractor used to measure apparent dips, trends, plunges, and rakes on planar and linear features in a split core, Expedition 362.

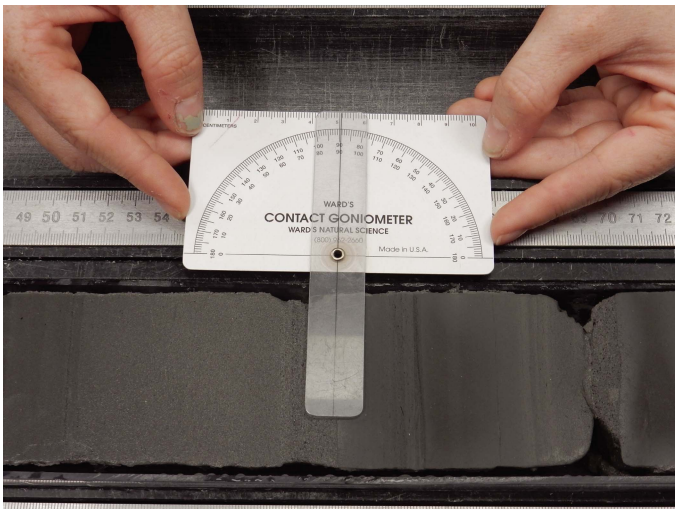

Figure F16. Diagram of core reference frame and *x*-, y-, z-coordinates used in orientation data calculations, Expedition 362.

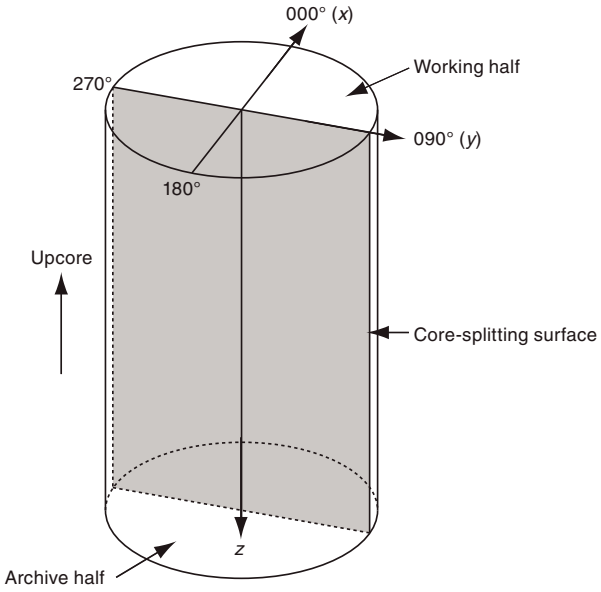

plane or the trend and plunge in the core reference frame. In postcruise research further orientation corrections may be made using paleomagnetic data (Figure **F17**). During Expedition 362, we measured rake for striations on fault surfaces (Figure **F19**) and azimuth and plunge for other lineations.

Description and classification of structures

We constructed a structural geology template for DESClogik that aids the description and classification of observed structures. We define the terminology used to describe deformation structures, both for clarity and as the basis for differentiating natural structures from drilling-induced features. We adopt a descriptive hierarchy (Table **T6**) for our structural classification in which we first define a structure type (e.g., fault, fracture, fold, shear zone, bedding, etc.) and then add a secondary descriptor to further classify the structure (e.g., normal, reverse, strike slip, or indeterminate). An indeterminate

Figure F17. Lower hemisphere equal area projections showing the procedure for converting 2-D measured data to 3-D data, Expedition 362. Plane attitude determined using two apparent dips on two surfaces. Striation on the plane is also plotted. In postcruise analysis, the data may be further corrected using paleomagnetic data.

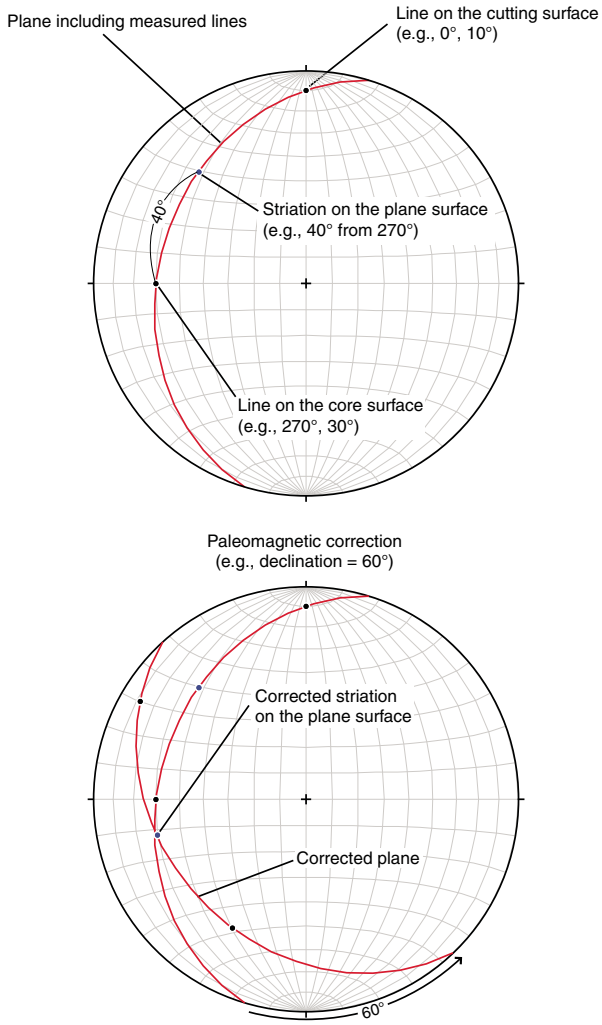

Figure F18. Calculation of plane orientation (shaded) from two apparent dips, Expedition 362. Intersections of split core surface, section perpendicular to split core surface, and section parallel to core direction with plane of interest are shown. (α_1, β_1) and (α_2, β_2) are the azimuths and dips of traces of the plane on two sections, v_1 and v_2 are unit vectors parallel to traces of the plane on two sections, and v_n is the unit vector normal to plane.

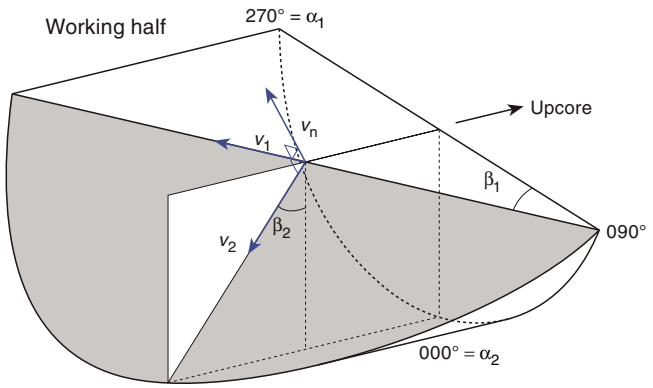

Figure F19. Apparent rake measurement of striations on a fault surface from 270° direction of split core surface trace, Expedition 362. ϕ_a = apparent rake, v_n = unit vector normal to fault plane, v_c = unit vector normal to split core surface, v_i = unit vector parallel to the intersection line between fault plane and split core surface.

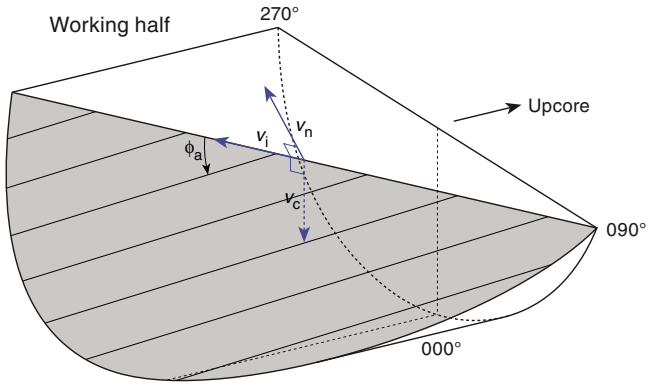

nate fault is one in which a structural surface has slickenlines that suggest displacement but without sufficient markers to define the sense of slip. A series of additional qualifying observations are also defined according to the structure defined (e.g., for fractures we include descriptors of fracture geometry and a description of open or closed).

Veins are defined as extensional fractures that are healed with minerals precipitated from a fluid. The lithology of the host rock and the mineralogy of the vein minerals are included in the comments section of the vein description, and the orientations of veins, foliations, and other structural features are part of the routine structural description.

Recognizing that there is often uncertainty in objectively defining structures as either natural (sedimentary or tectonic) or drilling induced, we categorize an interpretation confidence for each observation both to minimize the potential for any conflict and to maintain all observations in the database that remain equivocal; the intent is to provide the means to include or exclude observations in postcruise analyses based on different confidence thresholds. For deformation structures such as faults, the confidence scale is defined from 0 to 1, where 0 = no confidence (i.e., a fault is drilling induced with 100% certainty) that the observed structure is natural (tectonic or synsedimentary), and 1 = perfect confidence. We approach each structure (e.g., a fracture) initially with a confidence of 0.5 and look for observations to shift our confidence one way or another. For example, if we observe a fracture in the center of the core with petal fractures at its end, we shift to a confidence value <0.5 (i.e., it looks like a drilling-induced fracture). In practice, confidence values range from 0.1 to 0.9 in order to maintain some possibility that any individual structure may have a component of natural or drilling-induced deformation.

A second confidence criterion is recorded for faults in order to define the confidence in that the sense of slip is uniquely determined by the observations. For example, the highest confidence is assigned if offset marker horizons are visible in the core and striations define slip direction (e.g., dip-slip versus strike-slip).

For folds, the confidence factor reflects our ability to distinguish between tectonic and synsedimentary folds, whereas for bedding, confidence reflects our ability to assign the measured dip entirely to structural dip free from sedimentary dips (most importantly for low dips). For example, bedding surfaces associated with an erosional contact are likely to relate to depositional onlap or downlap, and we consult with the sedimentology group to help assess the likelihood and magnitude of possible sedimentary dips.

Calculation of plane orientation

For planar structures (e.g., bedding or faults), two measured apparent dips on two different surfaces are converted into the core reference frame as azimuths (measured clockwise from north, looking down) and plunges (Figures **F16**, **F17**, **F18**). A coordinate system was defined in such a way that the positive *x*-, *y*-, and *z*-directions coincide with north, east, and vertical downward, respectively. If the azimuths and plunges of the two apparent dips are given as (α_1, β_1) and (α_2, β_2), respectively, as in Figure **F18**, then the unit vectors representing these two lines, v_1 and v_2, are

$$v_1 = \begin{pmatrix} l_1 \\ m_1 \\ n_1 \end{pmatrix} = \begin{pmatrix} \cos\alpha_1 \cos\beta_1 \\ \sin\alpha_1 \cos\beta_1 \\ \sin\beta_1 \end{pmatrix}$$

and

$$v_2 = \begin{pmatrix} l_2 \\ m_2 \\ n_2 \end{pmatrix} = \begin{pmatrix} \cos\alpha_2 \cos\beta_2 \\ \sin\alpha_2 \cos\beta_2 \\ \sin\beta_2 \end{pmatrix}.$$

The unit vector normal to the plane, v_n (Figure **F18**), is then defined as

$$v_n = \begin{pmatrix} l_n \\ m_n \\ n_n \end{pmatrix} = \frac{v_1 \times v_2}{|v_1 \times v_2|},$$

where

$$v_1 \times v_2 = \begin{pmatrix} \begin{vmatrix} m_1 m_2 \\ n_1 n_2 \end{vmatrix} \\ \begin{vmatrix} n_1 n_2 \\ l_1 l_2 \end{vmatrix} \\ \begin{vmatrix} l_1 l_2 \\ m_1 m_2 \end{vmatrix} \end{pmatrix} = \begin{pmatrix} m_1 n_2 - m_2 n_1 \\ n_1 l_2 - n_2 l_1 \\ l_1 m_2 - l_2 m_1 \end{pmatrix}.$$

The azimuth, α_n, and plunge, β_n, of v_n are given by

$$\alpha_n = \tan^{-1}\left(\frac{m_n}{l_n}\right), \quad \beta_n = \sin^{-1} n_n.$$

The dip direction, α_d, and dip angle, β, of this plane are α_n and $90° + \beta_n$, respectively, when β_n is <0° (Figure **F20A**). They are $\alpha_n \pm 180°$ and $90° - \beta_n$, respectively, when $\beta_n \geq 0°$ (Figure **F20B**). The right-hand rule strike of this plane, α_s, is then given by $\alpha_d - 90°$.

Calculation of slickenline rake

For a fault with striations, the apparent rake angle of the striation, ϕ_a, was measured on the fault surface from either the 90° or 270° direction of the split-core surface trace (Figures **F17**, **F19**). Fault orientation was measured as described above. Provided that v_n and v_c are unit vectors normal to the fault and split core surfaces, respectively, the unit vector of the intersection line, v_i, is perpendicular to both v_n and v_c (Figure **F20**) and is therefore defined as

$$v_i = \begin{pmatrix} l_i \\ m_i \\ n_i \end{pmatrix} = \frac{v_n \times v_c}{|v_n \times v_c|},$$

where

$$v_c = \begin{pmatrix} 1 \\ 0 \\ 0 \end{pmatrix}$$

and

$$v_n \times v_c = \begin{pmatrix} \begin{vmatrix} m_n & 0 \\ n_n & 0 \end{vmatrix} \\ \begin{vmatrix} n_n & 0 \\ l_n & 1 \end{vmatrix} \\ \begin{vmatrix} l_n & 1 \\ m_n & 0 \end{vmatrix} \end{pmatrix} = \begin{pmatrix} 0 \\ n_n \\ -m_n \end{pmatrix}.$$

Knowing the right-hand rule strike of the fault plane, α_s, the unit vector, v_s, toward this direction is then

$$v_s = \begin{pmatrix} \cos\alpha_s \\ \sin\alpha_s \\ 0 \end{pmatrix}.$$

The rake angle of the intersection line, ϕ_i, measured from the strike direction is given by

$$\phi = \cos^{-1}(v_s \times v_i),$$

because

$$v_s \times v_i = |v_s||v_i|\cos\phi_i = \cos\phi_i \therefore |v_s| = |v_i| = 1.$$

Drilling deformation

One of the objectives of Expedition 362 includes characterizing the strength of the drilled sedimentary section in order to extrapolate those properties into the deformation environment of the Sumatra subduction zone. To help serve this objective, we seek to extract information about the relative strength and the deformation mode of the recovered materials by recording drilling deformation and considering the deformation experiment that drilling imposes on the sediments. Faults, fractures, breccias, and shear zones interpreted as drilling induced yield the most pertinent information about deformation mode, and the variation in lithology that supports those structures provides information about relative strengths. Drilling-induced folded and distorted beds developed in APC cores, which include upward-arching beddings that are caused by materials being forced into the core barrel (Figure **F21**), suggest that the material is weak and ductile. Another example is mingled and distorted beddings that are likely caused by suction of the materials into the core barrel during APC coring, and is perhaps an extreme version of upward-arching beds (Figure **F22**). Various flow structures (e.g., basal flow-in, midcore flow-in) and sandy sediment injected between segmented mud intervals also suggest that ductile deformation is possible. Drilling biscuits in XCB and RCB cores (Figure **F23**) are caused by rotation of the drill bit with respect to the sediments, and in the case of XCB coring the core liner rotates as well. Where biscuits break and in what lithology may lead to insights into mechanical heterogeneity. Drilling-induced gouge is often formed between biscuits by relative rotation and injection of drilling cuttings. Other coring disturbances, such as fall-in (Figure **F24**), soupy texture (Figure **F25**), gas expansion, core extension, and voids, offer less information about the properties of the sediment. We used terminology and examples documented by Jutzeler et al. (2014) and Schmidt et al. (2012) to guide our description scheme and employ common description of drilling disturbance intensity (slight, moderate, severe, and destroyed). For example, drilling disturbance intensity for upward-arching bedding and mingled and

Figure F20. Dip direction (α_d), right-hand rule strike (α_s), and dip (β) of a plane deduced from its normal azimuth (α_n) and dip (β_n), Expedition 362. v_n denotes the unit vector normal to plane. A. $\beta_n < 0°$. B. $\beta_n \geq 0°$.

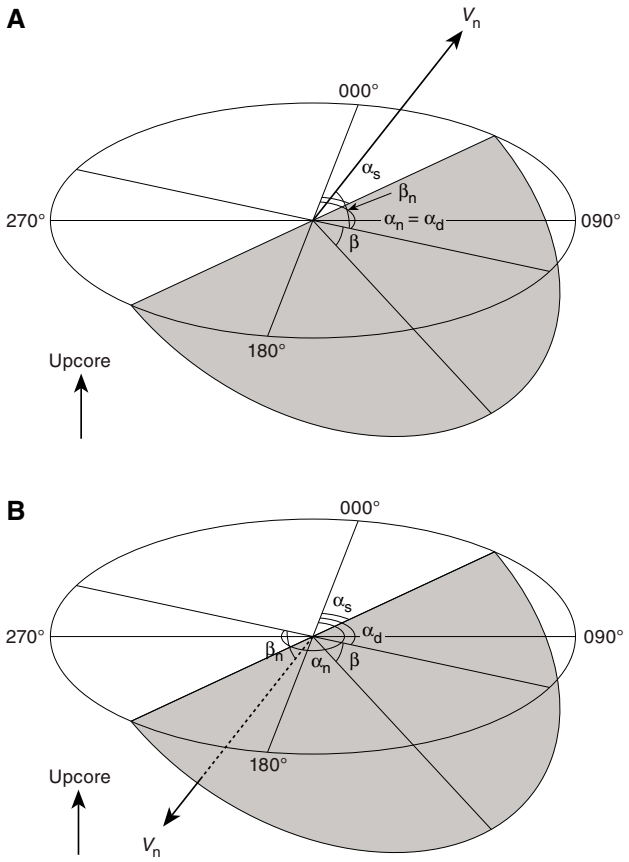

Figure F21. Upward-arching bedding observed in APC cores (Section U1480F-15F-2) and given a drilling disturbance intensity rating of slight, moderate, or severe based on the intensity of folding (i.e., slight from 62 to 73 cm, moderate from 30 to 62 cm, and severe from 73 to 102 cm).

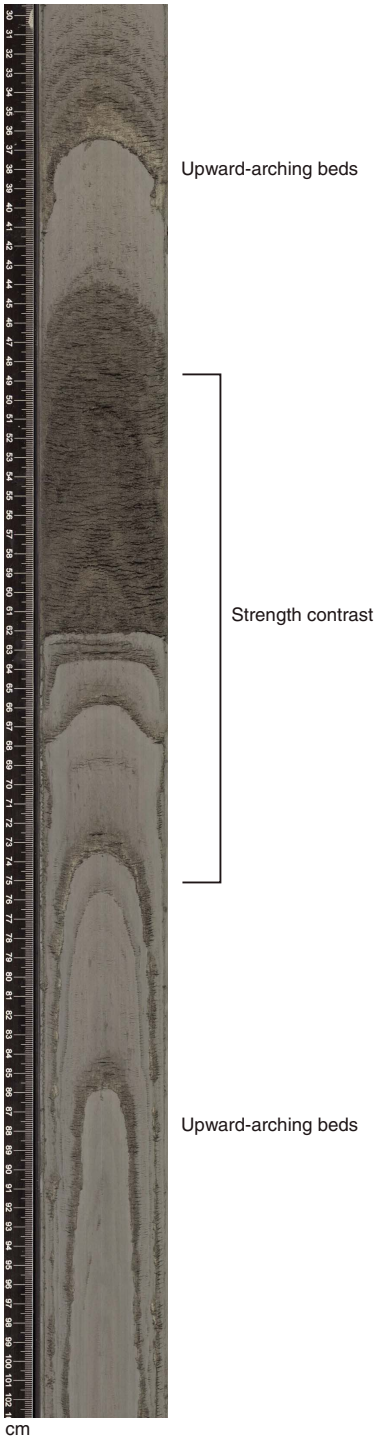

distorted bedding were rated based on the intensity of folding and destruction of primary bedding. For biscuiting of cores, intensity rating was given based on the thickness of biscuits as follows:

Slight: >5 cm thickness.
Moderate: 2–5 cm thickness.

Figure F22. Mingling and distortion of bedding observed in APC cores (Section U1480E-9H-6), perhaps an extreme version of upward-arching beds. Drilling disturbance features are given an intensity rating of slight, moderate, or severe based on the intensity of folding and destruction of primary bedding (i.e., extreme from 100 to 135 cm).

Severe: <2 cm thickness.
Destroyed: brecciated biscuits.

In addition to the drilling disturbance intensity, we added a column to interpret the drilling disturbance as either brittle, ductile, or indeterminate deformation mode, recognizing that this is a subjective, speculative interpretation, but one that we nevertheless think can serve as a guide for sample selection and site interpretation.

Our interpretation of drilling deformation is qualified by actual drilling parameters collected as the core is taken, including WOB, ROP, and torque. For example, increased WOB with a constant ROP or decreased ROP for constant WOB may reflect a stronger interval (e.g., Warren, 1981). Increased torque may reflect a sticky mud section that could develop ductile deformation mechanisms.

Strength log

The continuous strength log for each cored section, also a subjective interpretation, is one in which we speculate how each interval might deform based on observations of natural deformation features, drilling-induced deformation, and general sediment character in the core (see **Visual core descriptions**; Figure **F7**). This

Figure F23. Drilling biscuits (Section U1480G-14R-1) observed in XCB and RCB cores due to rotation of sediment behind coring surface and up into the core barrel (core barrel rotates with drill string in XCB but is stationary with respect to Earth in RCB). Drilling cuttings are injected between each biscuit, creating minor gouge. Drilling disturbance intensity rating was given based on the thickness of each biscuit as slight (>5 cm), moderate (2–5 cm), severe (<2 cm), and destroyed (brecciated biscuits).

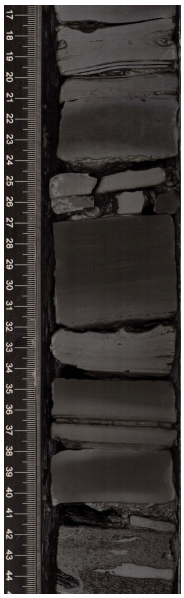

Figure F24. Fall-in at top of core (Section U1480F-12F-1). Fall-in was present at the top of many cores and was given a drilling disturbance intensity rating of destroyed.

qualitative classification is intended in the context of a field descriptive term, one used to help comprehend and assimilate detailed descriptive data in order to keep track of relative strength changes within a core and between adjacent cores. We also hope to remain more alert for changes that occur over several cores by recording observations of this property. We expect that the strength interpretation will become superseded by detailed analysis of physical property data and postcruise geomechanical tests and that the value of this description is greater during the expedition than afterward.

Figure F25. Soupy section in the sediment caused by drilling disturbance in which the primary structure is destroyed (Section U1480F-13F-3). Note the presence of water even after efforts to drain the core.

Based on these goals and expectations, there are no definitive criteria for defining the boundaries between weak, intermediate, and strong sediments or the expectation that an interval will deform by brittle or ductile methods. Rather, we used team experience and knowledge and apply that knowledge in a consistent manner.

Examples of end-member behavior help illustrate the strength description. For example, cores taken with a piston core (i.e., APC or HLAPC) and where physical property scientists are able to obtain a penetrometer reading are interpreted as weak. When drilling deformation in these cores results in folding (i.e., upward-arching beds or mingling and distortion of beds), the strength is interpreted as weak and ductile (Figure **F26**). In contrast, strong beds develop a more rock-like appearance (e.g., clay-rich sediments begin to develop fissility), are sampled more easily by a rock saw than chisel and hammer, and include lithologies like igneous rocks, concretions, and hard claystones (Figure **F27**). Biscuit formation, fracturing, brecciation, and similar types of drilling deformation lead to the inference of strong brittle deformation (Figure **F28**). Intermediate strengths lie between these two end-members (Figure **F29**), and the brittle versus ductile interpretation is based on the types of natural and drilling deformation observed in the core. Local, relative strength contrasts are interpreted when drilling deformation style and intensity varies between different lithologies (Figure **F21**).

Strain localization candidates are identified by an anomalous abundance of natural or drilling-induced deformation structures. We exclude unequivocal synsedimentary structures from this interpretation because they may reflect processes other than those that lead to deformation localization. Localization candidates are intended as placeholders for further evaluation with the expectation that many will prove to be irrelevant.

DESClogik structural geology database

The DESClogik database is a program used to store a visual (macroscopic and/or microscopic) description of core structures at a given depth. During Expedition 362, only the locations of structural features, calculated orientations in the core reference frame, and restored orientations based on the paleomagnetic data, were input into DESClogik. Orientation data management and planar fabric analysis were made with a spreadsheet as described above.

Figure F26. Weak, ductile material showing upward-arching beds, mingling and distortion of beds, and soupy deformation (Section U1480E-12H-3). Drilling disturbance is one of the primary criteria in assessing the strength of the material.

Drilling parameters used to interpret drilling deformation observations and strength inferences

Drilling and coring sediment and rock is a deformation experiment on the penetrated section. Hydraulic piston coring (APC and HLAPC) and rotary coring (XCB and RCB) are the two most distinct deformation experiments, but during this expedition we are most interested in the rotary shear experiment imposed by the XCB and RCB coring methods. An important difference between the XCB and RCB coring designs (Figures **F2**, **F3**) is that the core barrel in the XCB system latches into the BHA and thus rotates with the drill string and bit. Once the core passes the edge of the cutting surface, it is subject to torsion around the core similar to a ring-shear device in the laboratory. In contrast, the RCB lands in a support bearing in the BHA and has a vertical latch that keeps the core barrel in place; the core barrel remains stationary while the outer core barrel rotates around the inner core barrel. The cored material is only subject to torsion as it passes through the drill bit, and those forces end once the core enters the core barrel. In addition, the XCB bit extends in front of the main cutting bit and thus is less influenced by the hydraulic flow of drilling fluid used in the roller cone bit that completes the hole. The RCB coring method uses a roller cone design that both cuts the core and creates the hole at the same time.

Figure F27. Cores rated strong and brittle in strength. Brittle fractures, abundant natural faults, and some drilling-induced biscuits are present, but sections are more coherent. A. Calcareous pelagic sediment (Section U1480G-61R-3). B. Clay-rich hemipelagic sediment. Fissile fractures are abundantly observed (Section U1480G-58R-1).

In order to optimize drilling, maintain good hole conditions, and maximize core recovery, a vast number of drilling parameters are recorded by the Rig Instrumentation System (RIS; Graber et al., 2002). Although these parameters provide only a rough estimate of conditions at the bit, they provide one of the only continuous records of the drilled section. This information can prove useful in intervals with reduced core recovery (S. Midgley, pers. comm., 2016).

Our motivation is to attempt a first-order interpretation of relative strength contrasts, to normalize for constant drilling conditions when the type or intensity of drilling deformation is observed or qualify those differences if conditions change, and to provide a potential basis for extrapolating postcruise laboratory testing results across the drilled section. To address this problem, we use the concept of mechanical specific energy (MSE) introduced into the drill-

Figure F28. A. Core rated intermediate and ductile in strength. Upward-arching bedding is slight and sediments are more lithified based on use of hammer and chisel to obtain samples (Section U1480F-16F-1). B. Core rated intermediate and brittle in strength. Drilling-induced biscuiting with associated gouge was occasionally observed (Section U1480F-92X-1).

ing literature by Teale (1965), a concept that relates normal and torsional forces to the speed at which a rock is penetrated. These forces are related to the unconfined compressive strength of a rock, one of many parameters that describes the constitutive behavior of rocks.

Four drilling parameters define MSE: WOB, torque, rotary speed, and ROP (Teale, 1965). Although these parameters are used to diagnose drilling problems and optimize drilling performance based on assumed or independently determined rock properties (e.g., Dupriest and Koederitz, 2005; Pessler and Fear, 1992; Koederitz, 2005, Caicedo et al., 2005; Waughman et al., 2002; Bjornsson et al., 2004, Dupriest et al., 2005), we invert the problem by assuming that the driller is operating with a consistent level of performance by adjusting parameters to maintain maximum core recovery so that differences in MSE reflect changing rock properties. Recognizing that the assumption of consistent, optimized drilling performance is flawed, we proceed under the reasonable assumption that large differences in MSE still reflect changes in mechanical properties.

Definitions

The following are definitions of drilling parameters used in this analysis:

Figure F29. Example XCB drilling record for Core 362-U1480F-53X. Drilling parameters exported from RIS. TD torque defines the torque applied to the drill string by the top drive in kilo-ft-lb. Standpipe pressure (SPP) measures the hydraulic losses through the drilling system, including losses at the cutting bit. Time points (month/day/year hour:minute) annotated next to block position curve define the end of coring (sharp increase in block position) and start of coring (block position + interval drilled), which usually corresponds with change in pump rate and change in SPP. Note that in data presentations, axis ranges are kept constant to help comparison between cores, but a limited number of cores in Hole U1480G required an increase in maximum SPP plotted.

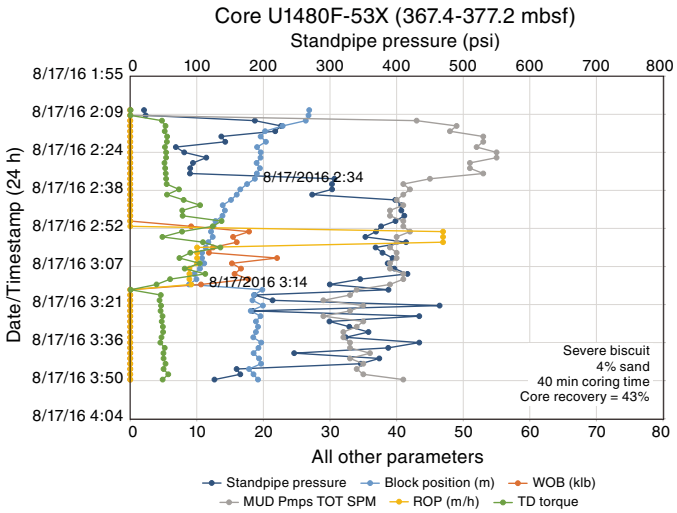

- WOB: the weight that the drill bit exerts on the rocks being cored and adjusted to optimize ROP (**https://en.wikipedia.org/wiki/Weight_on_bit**). Weight is provided by the massive drill collars that sit above the bit, but this weight is only a small fraction of the total weight of the drill string across the 4.1–5.9 km between the ship and the drill bit during Expedition 362. In the case of Expedition 362, the drilling operations plan attempted to maintain a constant WOB. However, WOB is manually controlled to optimize coring and is affected by vessel heave, so there is variability with each core. WOB is reported from the RIS in kilopounds (klb; 10^3 lb), and the most reliable measure of WOB reported by the RIS is AD Hook Load.
- ROP: the speed that the drilling bit cuts through rock (**https://en.wikipedia.org/wiki/Rate_of_penetration**). ROP is reported from the RIS in meters per hour (m/h).
- Torque (TD-Torque): a rotational force created by the top-drive motors to rotate the drill pipe and bit and allow a hole to be drilled. Torque thus reflects the resistance of a rock to be drilled. Torque is recorded by the RIS in amps, and these values are converted and reported in the RIS as kilo foot-pound (ft/lb·k).
- Rotary speed (TD-RPM): revolutions of the drill string defined as revolutions per minute (RPM).
- Mud pumps total (MPT): reflects the sum total volume of two mud pumps supplying hydraulic pressure to the drilling fluid and represents the flux of drilling fluid at the coring bit. Although the RIS records this in a number of different forms, we tracked this value in units of strokes per minute (SPM).
- Standpipe pressure (SPP): total pressure loss in a system that occurs due to fluid friction. SPP is the total system pressure, which is equal to pressure loss in the annulus, pressure loss in the drill string, pressure loss in the BHA, and pressure loss across the bit

(**https://www.petropedia.com/definition/3692/standpipe-pressure**). This parameter was used in concert with the MPT parameter to help identify the initiation of coring because SPP increases to reflect the work being done by the bit on the formation to drill a core. Units of SPP in the RIS are pounds per square inch (psi and presumably gauge pressure).

- Block position: a measure of depth defined with respect to the rig floor; a reference frame that is in constant flux because of swell heave and tides (Graber et al., 2002). Block position is considered the most reliable measure of depth recorded by the RIS and is used to define the start and end of coring (end of coring is recognized by a significant increase in block position after a long interval of decreasing block position, and start of coring is the advancement depth added to the block position at the end of coring). Block position is measured in meters (m).

The MPT and SPP parameters represent the hydraulic aspect of the drilling system used to remove cuttings from the drilling surface. These parameters provide a useful independent measure of the time that coring starts and stops because cuttings are generated during the coring process.

Comments and limitations of RIS data

Depth as recorded by the RIS on the *JOIDES Resolution*, a riserless vessel, is an uncertain quantity without the benefit of a fixed depth reference like the seafloor that is used in riser systems. Hence, parameters recorded by the RIS that rely on depth, like ROP, can be suspect (Graber et al., 2002). For this reason, we follow the recommendation of the RIS documentation and use block position defined with respect to the rig floor to monitor drill bit advancement.

The RIS also records continuous data up to 15 days at a time, at which point it is possible to export the data in ASCII format for processing and analysis. Given this time lag, it is difficult to use these data to influence operational decisions other than to observe RIS data using RigWatch.

The RIS records data at 1 s intervals; in one day 86,400 records are generated and, over a maximum 15-day timespan, 1,296,000 records. Coring occupies only a small fraction of that time, so any analysis requires the means to identify the beginning and end of each cored interval in the drilling time domain.

Methods applied

We chose to decimate the RIS data set to analyze records at 2 min. This provides a data set more suitable for initial screening analysis (Figure **F29**). Based on this analysis, we identify a limited number of discrete intervals appropriate for more detailed analysis. To decimate the data set, we used the FINDSTR command in Windows (provided by IODP Applications Developer Tim Blaisdell), which is described in STRUCTURE in **Supplementary material**. An alternative approach is offered by Tim Henstock using AWK scripts in a UNIX or LINUX environment (also in STRUCTURE in **Supplementary material**).

Data plotting

We plotted each parameter monitored between the times recorded for core on deck. In other words, the start of each plot (Figure **F29**) is based on the time the previous core is reported on deck, and the plot ends when the core under investigation is reported on deck. The following is a detailed example of the work flow.

The onset of coring is identified from the following characteristics:

1. Change in block position. In this instance, the block position changes from a constant value to a decreasing value at 2:34.
2. Increase in SPP. SPP increases at the same time as the break in slope in block position.
3. Onset of high and constant MPT. In this plot, this occurs at 2:34.
4. Increase in torque at 2:38. In the instances evaluated so far, this tends to lag the block position parameter.
5. WOB and ROP lag the onset of coring by 16 min. We often observe this lag, and in many cases neither WOB nor ROP deviate from zero when the core is taken.

The end of coring is defined by the following:

1. Minimum block position value followed by a large increase in block position at 3:14.
2. When ROP and WOB register in a plot, they drop to zero at the same time as the block position minimum.
3. Drop in torque.
4. Change in SPP and MPT. These values may increase if hole conditioning follows coring.
5. As a final check, because the end of coring is better defined than the onset of coring in many instances, the block position value is identified, the coring interval is added to the final block position to obtain its depth at the start of coring, and the time at the start of coring is rechecked. For example, in the example in Figure **F29**, the final block position is 8.84 m, the cored interval is 9.7 m, and the block position at the start of coring is 18.54 m. The block position at 2:34 is 18.73 m, which is the closest value to the target 18.54 m. A more detailed analysis with more frequent data records will improve this resolution.

Data analysis

Drilling data were combined into a value termed the specific energy factor (SEF) based on the MSE principle. MSE is defined as the sum of WOB and the quotient of torsional forces with ROP (Teale, 1965). Various constants and bit geometry terms are also included. For the sake of simplicity, we combined parameters without regard for reconciling units, neglected constants, and applied a factor of 100 to ROP to generate SEF values between 1 and 100. The form of SEF is

$$\text{SEF} \sim \text{WOB} + (\text{TD-Torque} \times \text{TD-RPM})/\text{ROP}.$$

We chose this simplified approach both to avoid the appearance of unwarranted precision that might be indicated by calculating MSE explicitly and to emphasize that we are searching for relative differences.

Four additional parameters were also compiled about the cored interval:

1. The predominant type and intensity of drilling deformation.
2. The fraction of sand recorded in the cored interval.
3. The time it took to collect the core.
4. The core recovery percentage as recorded in the Core Summary report in the LIMS database.

Although we recognize that every core contains a variety of drilling deformation types and intensities, we elected to characterize each core with the dominant types for initial data screening purposes. Part of the problem is that when there is incomplete recovery, it is difficult or impossible to assign any particular interval in the core with a specific coring interval. For example, in a core

with 20% recovery, does that segment belong to the beginning, end, or middle of the coring cycle? Without a clear method to address this issue, we chose to apply a more generalized core disturbance summary.

Sand fraction is based on the lithologic description. For most of the interval cored the remaining fraction is clay or silt, but the lithologic log is the ultimate record of all lithologies cored.

The time to collect a core is based on the difference between onset and end of coring. Because our screening analysis is based on a 2 min decimated data set, the precision of this determination is ±2 min.

Biostratigraphy

Biozonations and biohorizons

Preliminary age assignments were based on biostratigraphic analyses of calcareous nannofossils, diatoms, planktonic foraminifers, and radiolarians. Biostratigraphy was tied to the geomagnetic polarity timescale (GPTS) used for Expedition 362, which is a composite timescale based on Hilgen et al. (2012), Pälike et al. (2006), Vandenberghe et al. (2012), and Husson et al. (2011). See **Paleomagnetism** for details of the timescale used (Table **T11**). Summaries of biozones from all four microfossil groups together with the GPTS used for Expedition 362 are shown in Figure **F30**, with each part showing a ~23 My time interval.

Biostratigraphic data were collected from core catcher samples. Additional samples were analyzed, when suitable and time permitted, from within cores in order to decrease the depth uncertainty of individual biohorizons and to improve biostratigraphic resolution. All sample depths are cited in the text as midpoint depths within the sample interval of interest, where appropriate. Microfossil preservation, abundance, and biozone assignment data were entered through DESClogik and are available in the LIMS database (**http://web.iodp.tamu.edu/DESCReport**). In site chapters, we present the biostratigraphic data in tables showing depths of age-diagnostic biohorizons, stratigraphic distribution charts of these biohorizons, integrated biozonation figures, and age-depth plots. It should be noted that the distribution charts are based on shipboard study only and are, therefore, strongly biased toward age-diagnostic species.

Calcareous nannofossils

Three biozone schemes were employed: Backman et al. (2012) for the Miocene through Pleistocene interval, Agnini et al. (2014) for the Paleogene interval, and Burnett (1998) for the Maastrichtian interval. These biozonations represent a general framework for the biostratigraphic classification of middle- to low-latitude nannofossil assemblages throughout the Cenozoic and into the Maastrichtian, divided into three intervals: 0–23, 23–46, and 46–70 Ma. Biozones and chronostratigraphy for each of these intervals are presented in Figure **F31**. Age estimates of biohorizons defining biozone boundaries as well as many additional biohorizons are presented in Table **T7**. Nannofossil taxonomy follows Bown (1998, 2005) and Perch-Nielsen (1985a, 1985b), in which full taxonomic lists can be found.

Calcareous nannofossils were examined in smear slides using standard preparation and light microscope techniques under crossed polarizers and transmitted light. Samples were initially investigated using 50 fields of view (FOVs) at 630× magnification. Assemblages were investigated at 1000× magnification when needed for taxonomic resolution. Total calcareous nannofossil abundance within the sediment was recorded as

Figure F30. Expedition 362 timescale with planktonic foraminifer (PF), calcareous nannofossil (CN), diatom, and radiolarian biozones. Polarity: black = normal, white = reverse. A. 0–23 Ma. (Continued on next page.)

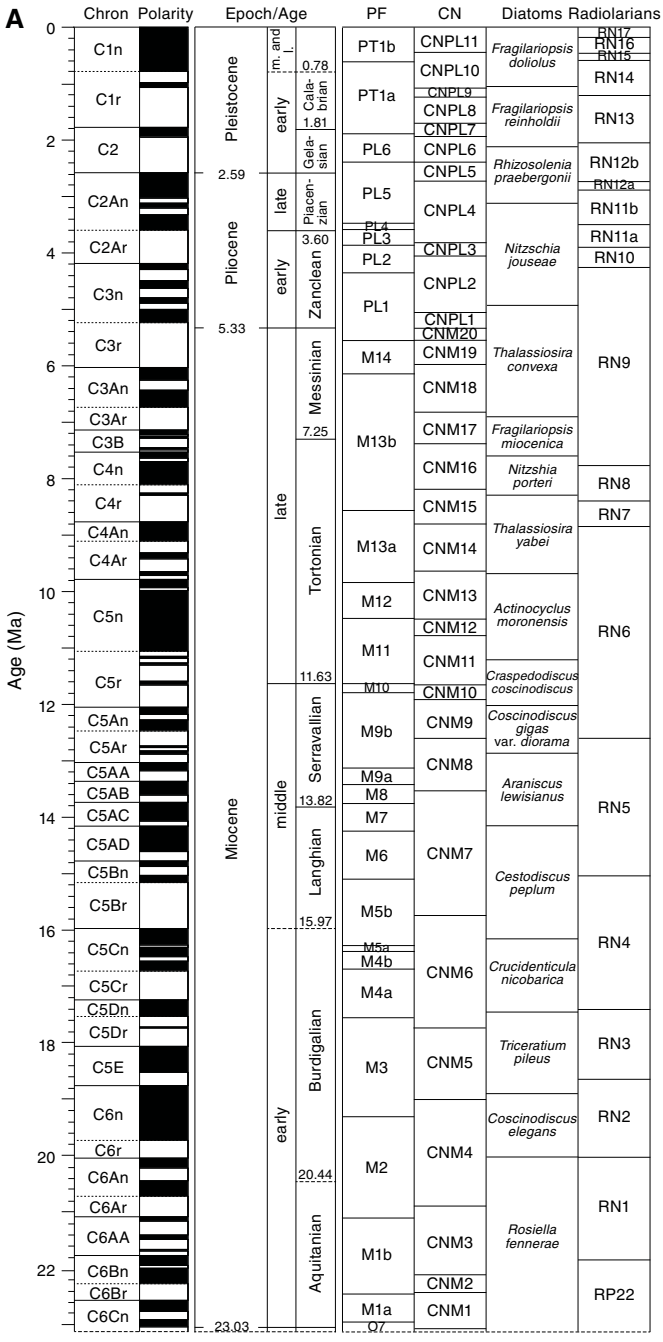

A = abundant (>50% of sediment particles).
C = common (>10%–50% of sediment particles).
F = few (1%–10% of sediment particles).
R = rare (<1% of sediment particles).
B = barren (no specimens).

Abundance of individual calcareous nannofossil taxa is recorded as

A = abundant (>10 specimens per FOV).
C = common (>1–10 specimens per FOV).
F = few (1 specimen per 1–10 FOVs).
R = rare (<1 specimen per 10 FOVs).

Figure F30 (continued). B. 23–46 Ma. C. 46–70 Ma.

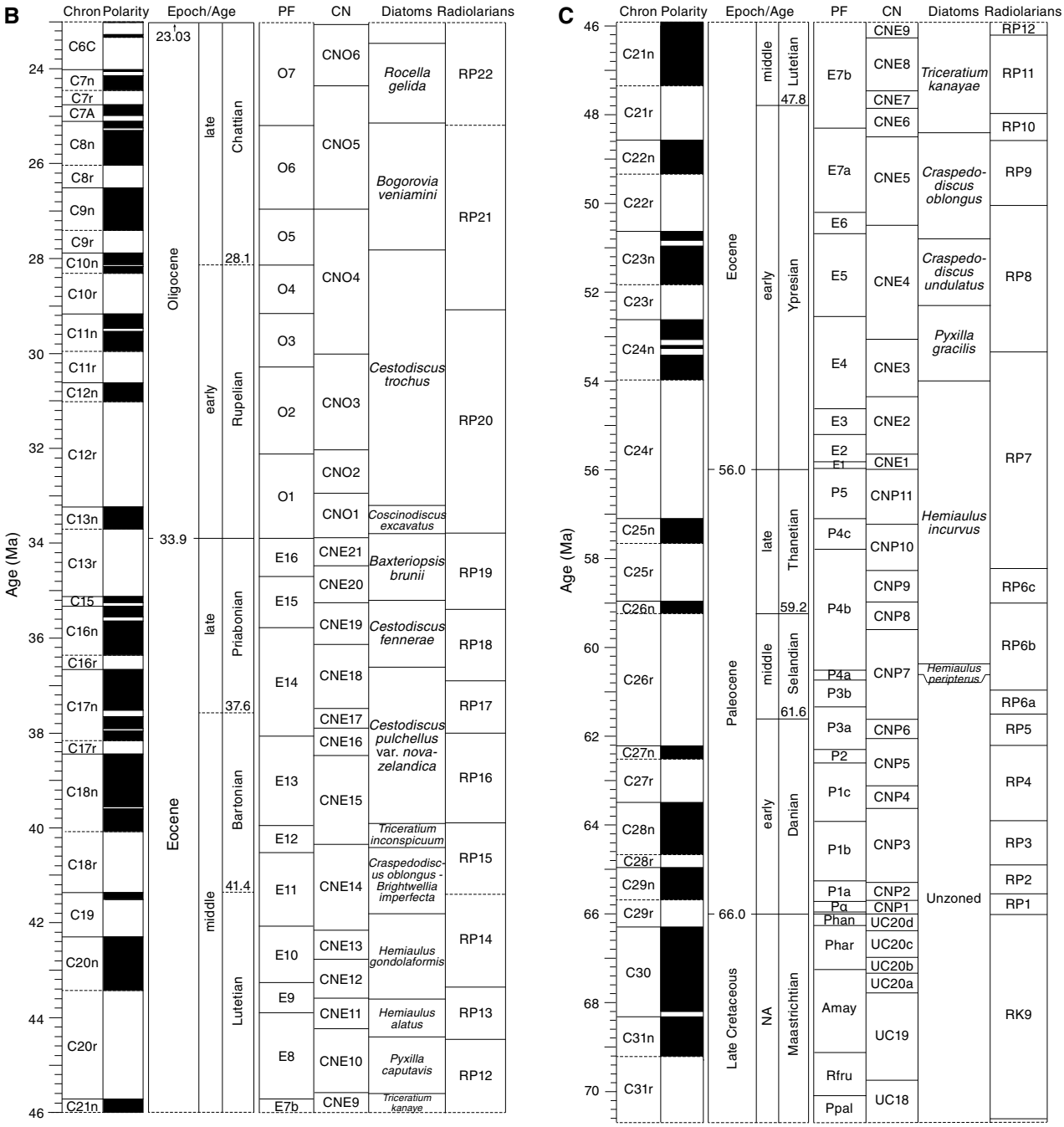

Preservation of the calcareous nannofossils is recorded as

G = good (little or no evidence of dissolution and/or recrystallization, primary morphological characteristics only slightly altered, and specimens were identifiable to the species level).

M = moderate (specimens exhibit some etching and/or recrystallization, primary morphological characteristics somewhat altered; however, most specimens were identifiable to the species level).

P = poor (specimens were severely etched or overgrown, primary morphological characteristics largely destroyed, fragmentation has occurred, and specimens often could not be identified at the species and/or generic level).

The combination of barren intervals, low abundances, and poor preservation of calcareous nannofossils made it impossible to follow the complete distribution of expected ranges of individual species throughout the investigated sediments. Rather, the distribution of presence and, in a few cases, absence, of species was recorded with a focus on age-calibrated marker species. Presence of a species having an age-calibrated extinction in a sample implies a youngest possible age for that sample depth. Presence of a species having an age-calibrated first evolutionary appearance in a sample implies an oldest possible age for that sample depth.

Figure F31. Calcareous nannofossil biozones and biohorizons defining biozone boundaries, Expedition 362. T = top, Tc = top common, Ta = top absence, B = base, Bc = base common, Ba = base absence. A. 0–23 Ma. B. 23–46 Ma. (Continued on next page.)

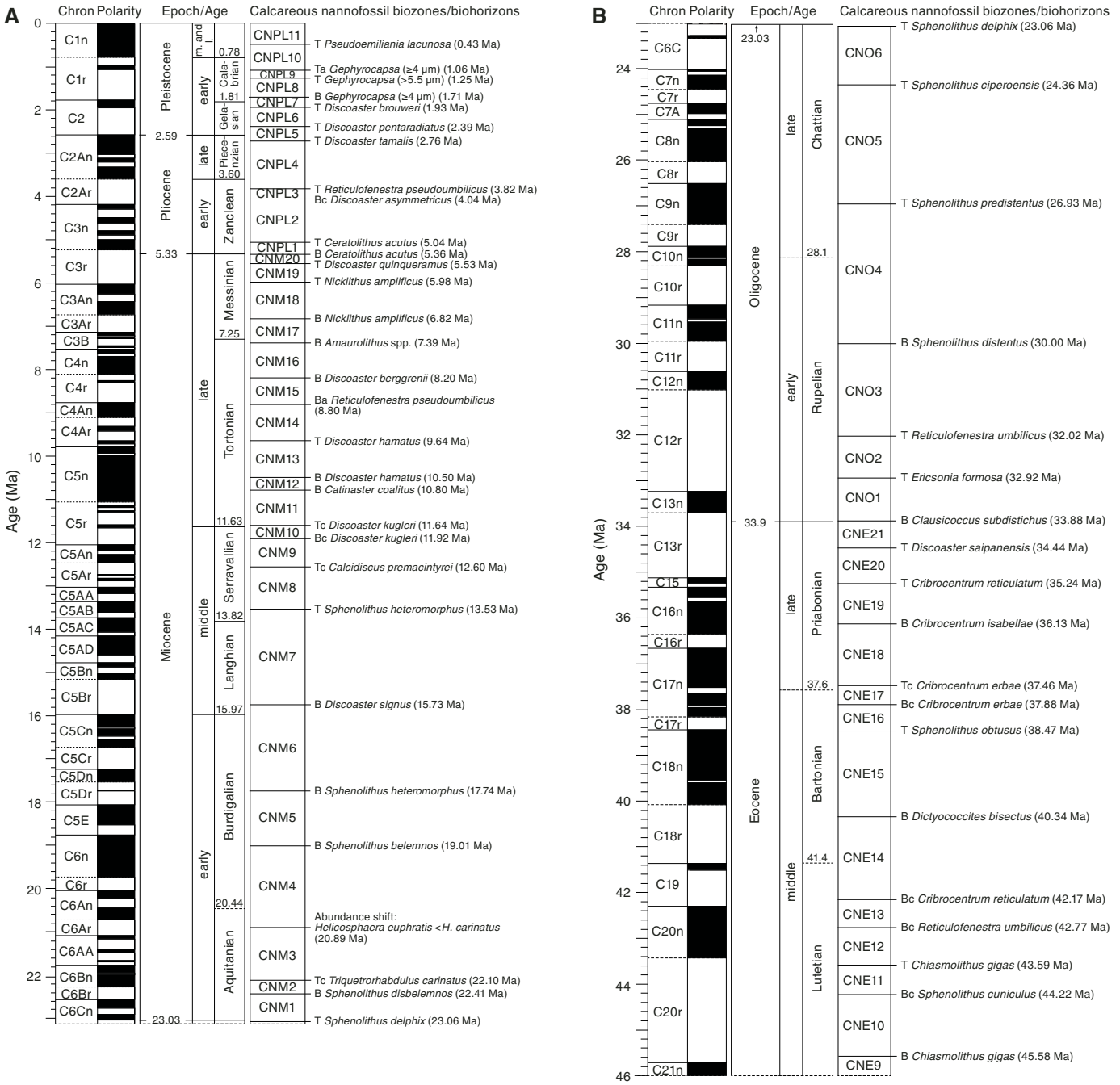

Planktonic foraminifers

The zonal scheme of Anthonissen and Ogg (2012) was used for the Late Cretaceous. The zonal scheme of Berggren and Pearson (2005), as modified by Wade et al. (2011), was used for the Paleogene (zonal codes P, E, and O), and that of Berggren et al. (1995), as modified by Wade et al. (2011), was used for the Quaternary and Neogene (zonal codes M, PL, and PT). The planktonic foraminifer zonal scheme used during Expedition 362 is illustrated in Figure **F32**. Calibrated ages are from Anthonissen and Ogg (2012) and adjusted to the Expedition 362 timescale (Table **T8**).

Planktonic foraminifer taxonomic concepts in the Late Cretaceous mainly follow Robaszynski et al. (1984) and Caron (1985). Taxonomic concepts in the Cenozoic mainly follow Blow (1979), Kennett and Srinivasan (1983), Toumarkine and Luterbacher (1985), Bolli and Saunders (1985), and Pearson et al. (2006).

Core catcher samples (plus one sample per section, as needed) were soaked in tap water or in a weak hydrogen peroxide solution when necessary, warmed on a hot plate, and washed over a 63 µm mesh sieve. Lithified material was crushed into ~2 cm^3 pieces, heated in a hydrogen peroxide solution, and then sieved as above. All samples were dried in sieves or on filter papers in a <60°C oven.

Figure F31 (continued). C. 46–70 Ma.

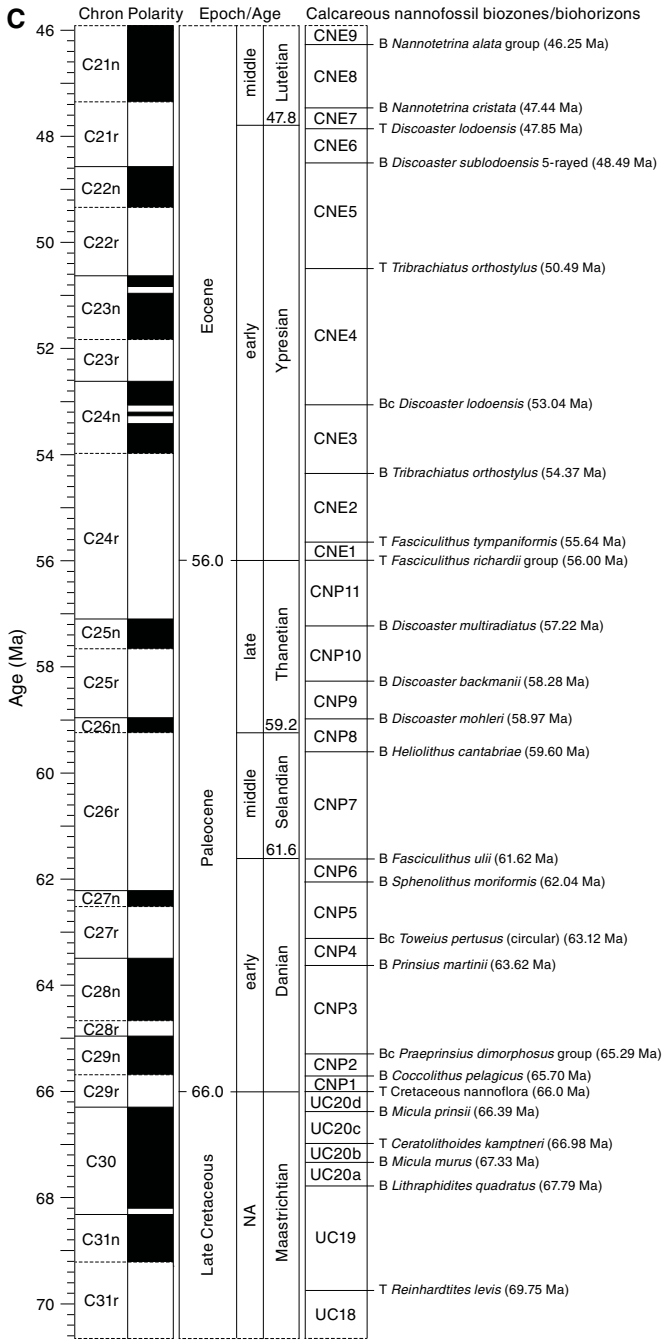

To minimize contamination of foraminifers, the sieves were placed into a sonicator for several minutes, cleaned with pressurized air, and thoroughly checked between samples. The dried samples were sieved over a 150 µm sieve, retaining the <150 µm size fraction for additional observation when necessary. The >150 µm size fraction specimens were examined under a Zeiss Discovery V8 microscope for species identification.

The total abundance of planktonic foraminifers was estimated from visual examination of the dried >63 µm residue and was defined as

A = abundant (>25% in total residue).
C = common (>10%–25% specimens in total residue).

Table T7. Age estimates of calcareous nannofossil biohorizons, Expedition 362. T = top, Tc = top common, Ta = top absence, B = base, Bc = base common, Ba = base absence. (Continued on next page.) **Download table in .csv format.**

Event	Age (Ma)	Base of biozone	References for biozones and age estimates
B *Emiliania huxleyi*	0.29		T CNPL11–B CNM1; Backman et al., 2012
T *Pseudoemiliania lacunosa*	0.43	CNPL11	
Tc *Reticulofenestra asanoi*	0.91		
Ta *Gephyrocapsa* (≥4 µm)	1.06	CNPL10	
Bc *Reticulofenestra asanoi*	1.14		
T *Helicosphaera sellii* (Atlantic)	1.24		
T *Gephyrocapsa* (>5.5 µm)	1.25	CNPL9	
B *Gephyrocapsa* (>5.5 µm)	1.59		
T *Calcidiscus macintyrei*	1.60		
B *Gephyrocapsa* (≥4 µm)	1.71	CNPL8	
T *Discoaster brouweri*	1.93	CNPL7	
Bc *Discoaster triradiatus*	2.16		
T *Discoaster pentaradiatus*	2.39	CNPL6	
T *Discoaster surculus*	2.53		
Pliocene/Pleistocene boundary	2.59		Hilgen et al., 2012
T *Discoaster tamalis*	2.76	CNPL5	
T *Sphenolithus* spp.	3.61		
T *Reticulofenestra pseudoumbilicus*	3.82	CNPL4	
Bc *Discoaster asymmetricus*	4.04	CNPL3	
T *Ceratolithus acutus*	5.04	CNPL2	
B *Ceratolithus rugosus*	5.08		
T *Ceratolithus atlanticus*	5.22		
T *Triquetrorhabdulus rugosus*	5.23		
T *Ceratolithus larrymayeri*	5.26		
Miocene/Pliocene boundary	5.33		Hilgen et al., 2012
B *Ceratolithus larrymayeri*	5.33		
B *Ceratolithus acutus*	5.36	CNPL1	
T *Discoaster quinqueramus*	5.53	CNM20	
T *Nicklithus amplificus*	5.98	CNM19	
T *Reticulofenestra rotaria*	6.79		Lourens et al., 2004
B *Nicklithus amplificus*	6.82	CNM18	
T *Reticulofenestra rotaria*	6.94		Raffi et al., 2003
Ta *Reticulofenestra pseudoumbilicus*	7.09		
B *Amaurolithus* spp.	7.39	CNM17	
B *Reticulofenestra rotaria*	7.40		Raffi et al., 2003
B *Discoaster berggrenii*	8.20	CNM16	
Ba *Reticulofenestra pseudoumbilicus*	8.80	CNM15	8.80–14.85 Ma; converted from Lourens et al., 2004 to Hilgen et al., 2012
T *Catinaster calyculus*	9.64		
T *Discoaster hamatus*	9.64	CNM14	
T *Catinaster calyculus*	9.64		
T *Catinaster coalitus*	9.70		
B *Discoaster bellus*	10.40		Lourens et al., 2004
B *Discoaster neohamatus*	10.48		
B *Discoaster hamatus*	10.50	CNM13	
T *Coccolithus miopelagicus* (Pacific)	10.62		Atlantic: 10.94 Ma
B *Catinaster calyculus*	10.72		
B *Discoaster brouweri*	10.74		Lourens et al., 2004
B *Catinaster coalitus*	10.80	CNM12	
Tc *Discoaster kugleri*	11.64	CNM11	
Bc *Discoaster kugleri*	11.92	CNM10	
T *Coronocyclus nitescens*	12.18		
T *Calcidiscus premacintyrei*	12.60	CNM9	
T *Sphenolithus heteromorphus*	13.53	CNM8	
T *Helicosphaera ampliaperta*	14.85		
Tc *Discoaster deflandrei*	15.69		
B *Discoaster signus*	15.73	CNM7	
B *Sphenolithus heteromorphus*	17.74	CNM6	
T *Sphenolithus belemnos*	17.94		
B *Sphenolithus belemnos*	19.01	CNM5	
T *Triquetrorhabdulus carinatus*	19.18		
B *Helicosphaera ampliaperta*	20.43		
Helicosphaera euphratis < *H. carteri* (shift)	20.89	CNM4	
Tc *Triquetrorhabdulus carinatus*	22.10	CNM3	
B *Sphenolithus disbelemnos*	22.41	CNM2	

Table T7 (continued).

Event	Age (Ma)	Base of biozone	References for biozones and age estimates
B *Discoaster druggii* (Pacific)	22.59		
Oligocene/Miocene boundary	23.03		Hilgen et al., 2012
T *Sphenolithus delphix*	23.06	CNM1	T CNO6–B CNP1; Agnini et al., 2014
B *Sphenolithus delphix*	23.38		
T *Sphenolithus ciperoensis*	24.36	CNO6	
Triquetrorhabdulus longus < *T. carinatus*	25.04		
T *Sphenolithus distentus*	26.81		
T *Sphenolithus predistentus*	26.93	CNO5	
B *Sphenolithus ciperoensis*	27.14		
B *Sphenolithus distentus*	30.00	CNO4	
T *Reticulofenestra umbilicus*	32.02	CNO3	
T *Coccolithus formosus*	32.92	CNO2	
B *Clausicoccus subdistichus*	33.88	CNO1	
Eocene/Oligocene boundary			Coccioni et al., 1988
T *Discoaster saipanensis*	34.44	CNE21	
T *Discoaster barbadiensis*	34.77		
T *Cribrocentrum reticulatum*	35.24	CNE20	
B *Cribrocentrum isabellae*	36.13	CNE19	
Bc *Isthmolithus recurvus*	36.84		
Tc *Cribrocentrum erbae*	37.46	CNE18	
T *Chiasmolithus grandis*	37.77		
B *Chiasmolithus oamaruensis*	37.84		
Bc *Cribrocentrum erbae*	37.88	CNE17	
T *Sphenolithus obtusus*	38.47	CNE16	
B *Dictyococcites bisectus*	40.34	CNE15	
T *Sphenolithus furcatolithoides*	40.51		
Bc *Cribrocentrum reticulatum*	42.17	CNE14	
Bc *Reticulofenestra umbilicus*	42.77	CNE13	
T *Chiasmolithus gigas*	43.59	CNE12	
Bc *Sphenolithus cuniculus*	44.22	CNE11	
B *Sphenolithus furcatolithoides*	45.43		
B *Chiasmolithus gigas*	45.58	CNE10	
B *Nannotetrina alata* group	46.25	CNE9	
B *Nannotetrina cristata*	47.44	CNE8	
T *Discoaster lodoensis*	47.85	CNE7	
B *Discoaster sublodoensis* (5 rayed)	48.49	CNE6	
Toweius < *Dictyococcites* + *Reticulofenestra*	50.49		
T *Tribrachiatus orthostylus*	50.49	CNE5	
Bc *Discoaster lodoensis*	53.04	CNE4	
B *Girgisia gammation*	53.72		
T *Tribrachiatus contortus*	54.15		
B *Sphenolithus radians*	54.20		
Tc *Discoaster multiradiatus*	54.26		
B *Tribrachiatus orthostylus*	54.37	CNE3	
B *Tribrachiatus contortus*	54.78		
B *Discoaster diastypus*	54.94		
T *Fasciculithus tympaniformis*	55.64	CNE2	
B *Rhomboaster* spp.	55.98		
T *Fasciculithus richardii* group	56.00	CNE1	
Paleocene/Eocene boundary	56.0		Vandenberghe et al., 2012
T *Ericsonia robusta*	57.10		
B *Discoaster multiradiatus*	57.22	CNP11	
T *Sphenolithus anarrhopus*	57.26		
B *Discoaster delicatus*	57.45		
B *Discoaster nobilis*	57.50		
B *Discoaster backmanii*	58.28	CNP10	
T *Heliolithus kleinpellii*	58.81		
B *Discoaster mohleri*	58.97	CNP9	
B *Heliolithus kleinpellii*	59.36		
B *Heliolithus cantabriae*	59.60	CNP8	
B *Fasciculithus tympaniformis*	61.24		
B *Fasciculithus ulii*	61.62	CNP7	
B *Sphenolithus moriformis*	62.04	CNP6	
Bc *Toweius pertusus* (circular)	63.12	CNP5	
B *Prinsius martinii*	63.62	CNP4	
Bc *Praeprinsius dimorphosus* gr.	65.29	CNP3	
B *Praeprinsius dimorphosus* gr.	65.60		
B *Cruciplacolithus intermedius*	65.65		
B *Coccolithus pelagicus*	65.70	CNP2	
T Cretaceous nannoflora	66.0	CNP1	
Late Cretaceous/Paleocene boundary	66.0		Vandenberghe et al., 2012; Husson et al., 2011
Tc *Micula murus*	66.07		Maastrichtian; Thibault et al., 2012
Tc *Cribrocorona gallica*	66.24		
B *Micula prinsii*	66.39	UC20d	
Bc *Cribrocorona gallica*	66.39		
Tc *Lithraphidites quatratus* and *L. praequadratus*	66.39		
T *Biscutum constans*	66.49		
Bc *Micula murus*	66.56		
B *Ceratolithoides indiensis*	66.87		
B *Discorhabdus ignotus*	66.87		
T *Ceratolithoides kamptneri*	66.98	UC20c	
Bc *Lithraphidites quatratus* and *L. praequadratus*	67.07		
B *Micula murus*	67.33	UC20b	
B *Lithraphidites quadratus*	67.79	UC20a	
T *Ahmuelerella octoradiata*	67.79		
T *Petrarhabdus vietus*	67.79		
B *Pseudomicula quadrata*	68.02		
B *Micula praemurus*	68.07		
B *Lithraphidites praequadratus*	68.18		
B *Cribrocorona gallica*	68.18		
T *Stoverius coangustatus*	68.40		
T *Amphizygus brooksii*	68.95		
T *Broinsonia parca* spp. *constricta*	69.48		
T *Reinhardtites levis*	69.75	UC19	

F = few (5%–10% specimens in total residue).
R = rare (<5% specimens in total residue).
VR = very rare (<0.1% specimens in total residue).
B = barren (no specimens in total residue).

Individual planktonic foraminifers were recorded in qualitative terms, based on an assessment of forms, observed in a random sample of ~150 specimens from the >150 µm size fraction. In samples where fewer than 150 specimens were present, all specimens were counted. Relative abundances were reported using the following categories:

A = abundant (>25 specimens).
C = common (11–25 specimens).
F = few (5–10 specimens).
R = rare (<5 specimens).
B = barren (none present).

The preservation status of planktonic and benthic foraminifers was estimated as

VG = very good (no evidence of overgrowth, dissolution, or abrasion).
G = good (little evidence of overgrowth, dissolution, or abrasion).
M = moderate (calcite overgrowth, dissolution, or abrasion are common but minor).
P = poor (substantial overgrowth, dissolution, or abrasion).

Figure F32. Planktonic foraminiferal biozones and biohorizons defining biozone boundaries, Expedition 362. T = top, B = base. A. 0–23 Ma. B. 23–46 Ma. (Continued on next page.)

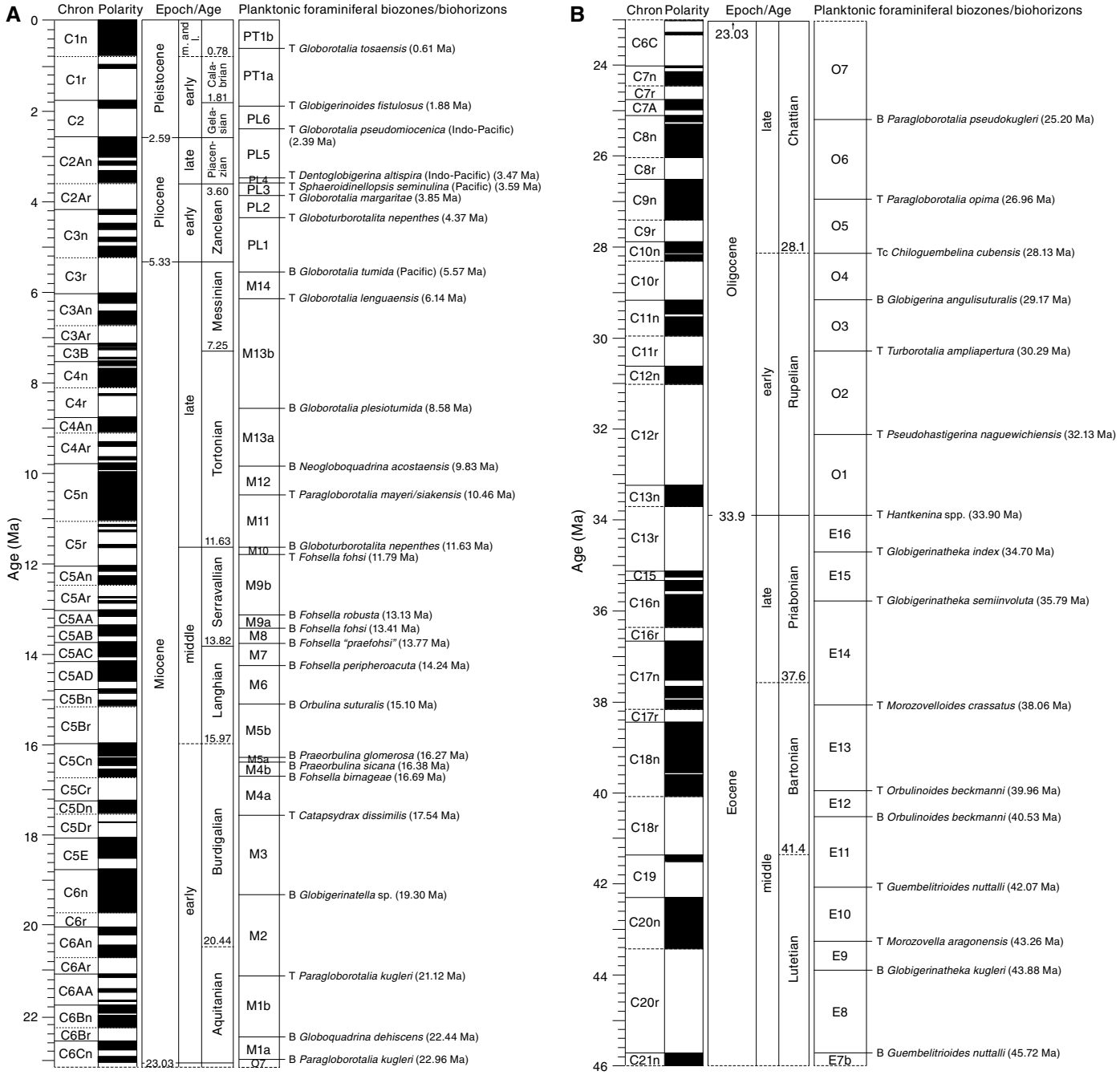

Diatoms

Because of the overall low abundance of diatoms, it was necessary to concentrate diatoms by boiling sediment in HCl and H_2O_2 to remove carbonate and organic material before sieving at 150 µm (with the fine fraction retained) and 10 µm (with the coarse fraction retained). Strewn slides were then prepared with the residue, using 22 mm × 40 mm coverslips and a few drops of Norland optical adhesive. As a result of processing, only relative abundances of taxa were recorded. At least four traverses of each strewn slide were examined on a Zeiss Axiophot light microscope at 500× magnification, with species identification at 1000× magnification if necessary.

Diatom biohorizons for Expedition 362 were compiled from Baldauf (1985), Fourtanier (1991a, 1991b), Barron (1992, 2006), and Barron et al. (2004, 2014, 2015). Diatom biozones follow Burckle (1972) for the late Miocene–Quaternary, Barron (2006) for the early Miocene–late Oligocene, Barron et al. (2014) for the early Oligocene–late Eocene, and Fourtanier (1991b) for the early Eocene–Paleocene. All biohorizons and biozone boundaries were modified where necessary according to the Expedition 362 timescale. Modified diatom biohorizons and biozones are detailed in Table **T9** and shown in Figure **F33**.

Figure F32 (continued). C. 46–70 Ma.

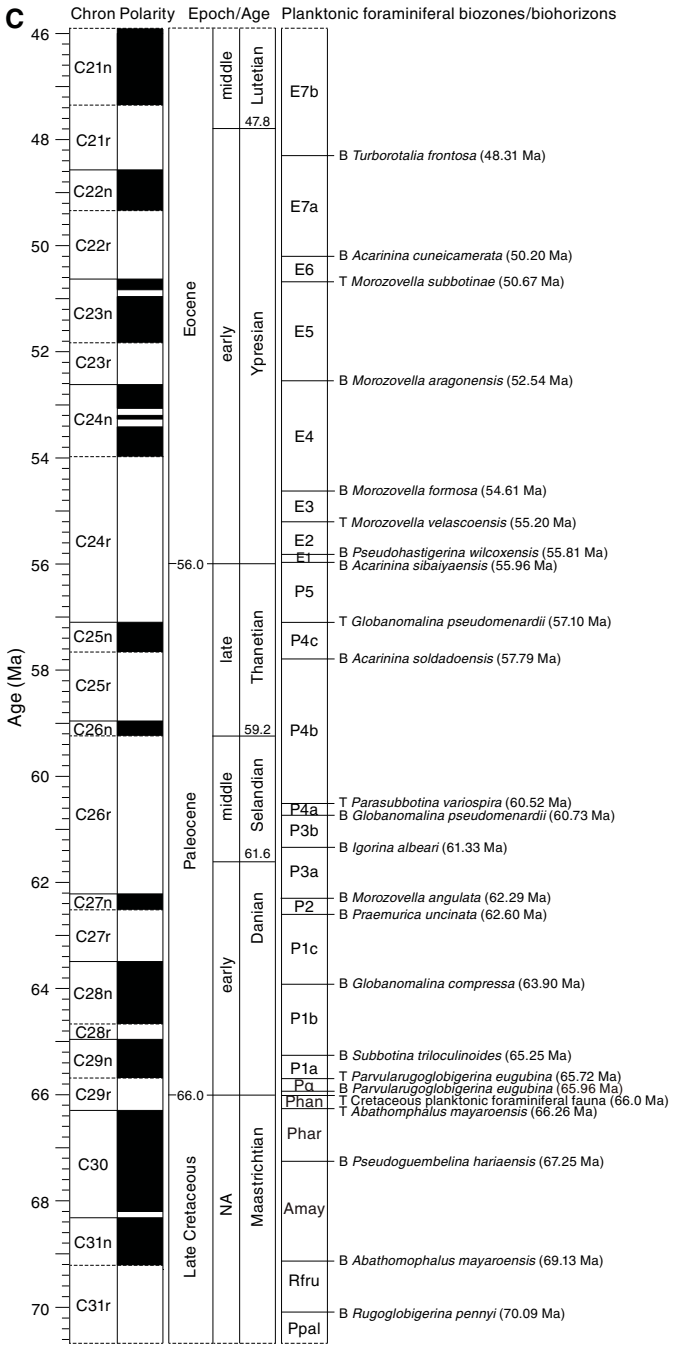

Relative abundances of individual diatom taxa were estimated from counts per FOV:

A = abundant (>5 valves/FOV).
C = common (3–5 valves/FOV).
F = few (1–2 valves/FOV).
R = rare (≥2 valves/traverse of coverslip).
P = present (at least 1 valve observed, including fragments).
B = barren (no valves observed).

Diatom preservation was described qualitatively following Barron and Gladenkov (1995):

Table T8. Age estimates of planktonic foraminiferal biohorizons, Expedition 362. S = sinistral, D = dextral. IO = Indian Ocean. (Continued on next two pages.) **Download table in .csv format.**

Event	Age (Ma)	Base of biozone	References for biozones and age estimates
T *Globorotalia flexuosa*	0.07		Anthonissen and Ogg, 2012 (on Exp. 362 timescale)
T *Globigerinoides ruber* (pink) (Indo-Pacific)	0.12		
B *Globorotalia flexuosa*	0.40		
T *Globorotalia tosaensis*	0.61	PT1b	
B *Globorotalia hessi*	0.75		
X *Pulleniatina* coiling random to D	0.80		
B *Globorotalia excelsa* (Mediterranean)	1.00		
T *Globigerinoides obliquus*	1.30		
T *Neogloboquadrina acostaensis*	1.58		
T *Globoturborotalita apertura*	1.64		
T *Globigerinoides fistulosus*	1.88	PT1a	
B *Globorotalia truncatulinoides*	1.93		
T *Globigerinoides extremus*	1.98		
B *Pulleniatina finalis*	2.04		
T *Globorotalia pertenuis*	2.30		
T *Globoturborotalita woodi*	2.30		
T *Globorotalia pseudomiocenica* (Indo-Pacific)	2.39	PL6	
Pliocene/Pleistocene boundary	2.59		Hilgen et al., 2012
T *Globoturborotalita decoraperta*	2.75		
T *Globorotalia multicamerata*	2.98		
B *Globigerinoides fistulosus*	3.33		
B *Globorotalia tosaensis*	3.35		
T *Dentoglobigerina altispira* (Indo-Pacific)	3.47	PL5	
B *Globorotalia pertenuis*	3.52		
T *Sphaeroidinellopsis seminulina* (Pacific)	3.59	PL4	
T *Pulleniatina primalis* (Pacific)	3.66		
T *Globorotalia plesiotumida*	3.77		
T *Globorotalia margaritae*	3.85	PL3	
X *Pulleniatina* coiling S→D	4.08		
T *Pulleniatina spectabilis* (Pacific)	4.21		
B *Globorotalia crassaformis* s.l.	4.31		
T *Globoturborotalita nepenthes*	4.37	PL2	
B *Globorotalia exilis* (Atlantic)	4.45		
T *Sphaeroidinellopsis kochi*	4.53		
T *Globorotalia cibaoensis*	4.60		
T *Globigerinoides seiglei*	4.72		
Miocene/Pliocene boundary	5.33		Hilgen et al., 2012
B *Sphaeroidinella dehiscens* sensu lato	5.53		
B *Globorotalia tumida* (Pacific)	5.57	PL1	
B *Turborotalita humilis*	5.81		
T *Globoquadrina dehiscens*	5.92		
B *Globorotalia margaritae*	6.08		
T *Globorotalia lenguaensis* (Pacific)	6.14	M14	
B *Globigerinoides conglobatus*	6.20		
X *Neogloboquadrina acostaensis* coiling S→D	6.37		
B *Pulleniatina primalis*	6.60		
X *Neogloboquadrina acostaensis* coiling D→S	6.77		
B *Candeina nitida*	8.43		
B *Neogloboquadrina humerosa*	8.56		
B *Globorotalia plesiotumida*	8.58	M13b	
B *Globigerinoides extremus*	8.93		
B *Neogloboquadrina pachyderma* (IO)	9.37		
B *Globorotalia cibaoensis*	9.44		
B *Globorotalia juanai*	9.69		
B *Neogloboquadrina acostaensis* (Sub)Tropical	9.83	M13a	
T *Globorotalia challengeri*	9.99		

Table T8 (continued). (Continued on next page.)

Event	Age (Ma)	Base of biozone	References for biozones and age estimates
T *Neogloboquadrina nympha* (IO)	10.20		
T *Paragloborotalia mayeri/siakensis* (Sub)Tropical	10.46	M12	
B *Globorotalia limbata*	10.64		
T *Cassigerinella chipolensis*	10.89		
B *Globoturborotalita apertura*	11.18		
B *Globorotalia challengeri*	11.22		
B *Globigerinoides obliquus* (regular)	11.25		
B *Globoturborotalita decoraperta*	11.49		
T *Globigerinoides subquadratus*	11.54		
B *Globoturborotalita nepenthes*	11.63	M11	
T *Fohsella fohsi* (*Fohsella plexus*)	11.79	M10	
T *Globorotalia panda* (IO)	11.93		
T *Clavatorella bermudezi*	12.00		
T *Tenuitella selleyi/pseudoedita/minutissima/clemebciae* (IO)	12.37		
B *Globorotalia lenguanensis*	12.84		
B *Sphaeroidinellopsis subdehiscens*	13.02		
B *Fohsella robusta*	13.13	M9b	
T *Cassigerinella martinezpicoi*	13.27		
B *Fohsella fohsi*	13.41	M9a	
B *Neogloboquadrina nympha*	13.49		
B *Fohsella "praefohsi"*	13.77	M8	
T *Fohsella peripheroronda*	13.80		
T *Clavatorella bermudezi* (regular)	13.82		
T *Globorotalia archeomenardii*	13.87		
B *Fohsella peripheroacuta*	14.24	M7	
B *Globorotalia praemenardii*	14.38		
T *Praeorbulina sicana*	14.53		
T *Globigeriantella insueta*	14.66		
T *Praeorbulina glomerosa* s.s.	14.78		
T *Praeorbulina circularis*	14.89		
B *Orbulina suturalis*	15.10	M6	
B *Clavatorella bermudezi*	15.73		
B *Praeorbulina circularis*	15.96		
B *Globigerinoides diminutus*	16.06		
B *Globorotalia archeomenardii*	16.26		
B *Praeorbulina glomerosa* s.s.	16.27	M5b	
B *Praeorbulina curva*	16.28		
B *Praeorbulina sicana*	16.38	M5a	
T *Globorotalia incognita*	16.39		
B *Fohsella birnageae*	16.69	M4b	
B *Globorotalia miozea*	16.70		
B *Globorotalia zealandica*	17.26		
T *Globorotalia semivera*	17.26		
T *Catapsydrax dissimilis*	17.54	M4a	
B *Globigeriantella insueta* s.s.	17.59		
B *Globorotalia praescitula*	18.26		
T *Globoquadrina binaiensis*	19.09		
B *Globogerinatella* sp.	19.30	M3	
B *Globoquadrina binaiensis*	19.30		
B *Globigerinoides altiapertura*	20.03		
T *Tenuitella munda*	20.78		
B *Globorotalia incognita*	20.93		
T *Globoturborotalita angulisuturalis*	20.94		
T *Paragloborotalia kugleri*	21.12	M2	
T *Paragloborotalia pseudokugleri*	21.31		
B *Globoquadrina dehiscens* f. *spinosa*	21.44		
T *Dentoglobigerina globularis*	21.98		
B *Globoquadrina dehiscens*	22.44	M1b	
T *Globigerina ciperoensis*	22.90		
B *Globigerinoides trilobus* s.l.	22.96		
B *Paragloborotalia kugleri*	22.96	M1a	
Oligocene/ Miocene boundary	23.03		Hilgen et al., 2012
T *Globigerina euapertura*	23.03		
T *Tenuitella gemma*	23.55		
Bc *Globigerinoides primordius*	23.55		
B *Paragloborotalia pseudokugleri*	25.20	O7	
B *Globigerinoides primordius*	26.18		
T *Paragloborotalia opima* s.s.	26.96	O6	
Tc *Chiloguembelina cubensis*	28.13	O5	
B *Globigerina angulisuturalis*	29.17	O4	
B *Tenuitellinata juvenilis*	29.49		
T *Subbotina angiporoides*	29.83		
T *Turborotalia ampliapertura*	30.29	O3	
B *Paragloborotalia opima*	30.74		
T *Pseudohastigerina naguewichiensis*	32.13	O2	
B *Cassigerinella chipolensis*	33.89		
Eocene/ Oligocene boundary	33.90	O1	Coccioni et al., 1988
T *Hantkenina* spp. (*Hantkenina alabamensis*)	33.90		
Tc *Pseudohastigerina micra*	33.90		
T *Turborotalia cerroazulensis*	34.06		
T *Cribrohantkenina inflata*	34.27		
T *Globigerinatheka index*	34.70	E16	
T *Turborotalia pomeroli*	35.32		
B *Turborotalia cunialensis*	35.33		
B *Cribrohantkenina inflata*	35.53		
T *Globigerinatheka semiinvoluta*	35.79	E15	
T *Acarinina* spp.	37.52		
T *Subbotina linaperta*	37.76		
T *Acarinina collactea*	37.76		
T *Morozovelloides crassatus*	38.06	E14	
B *Globigerinatheka semiinvoluta*	38.45		
T *Acarinina mcgowrani*	38.45		
T *Planorotalites* spp.	38.45		
T *Acarinina primitiva*	39.00		
T *Turborotalia frontosa*	39.32		
T *Orbulinoides beckmanni*	39.96	E13	
B *Orbulinoides beckmanni*	40.53	E12	
T *Acarinina bullbrooki*	40.53		
T *Guembelitrioides nuttalli*	42.07	E11	
B *Turborotalia pomeroli*	42.21		
B *Globigerinatheka index*	42.64		
B *Morozovelloides lehneri*	43.15		
T *Morozovella aragonensis*	43.26	E10	
B *Globigerinatheka kugleri*	43.88	E9	
B *Hantkenina singanoae*	44.49		
B *Turborotalia possagnoensis*	45.49		
B *Guembelitrioides nuttalli*	45.72	E8	
B *Turborotalia frontosa*	48.31	E7b	
B *Acarinina cuneicamerata*	50.20	E7a	
B *Planorotalites palmerae*	50.20		
T *Morozovella subbotinae*	50.67	E6	
B *Acarinina pentacamerata*	50.67		
B *Morozovella aragonensis*	52.54	E5	
T *Morozovella marginodentata*	52.85		
T *Morozovella lensiformis*	53.14		
T *Morozovella aequa*	54.20		
B *Morozovella formosa*	54.61	E4	
B *Morozovella lensiformis*	54.61		
T *Subbotina velascoensis*	55.07		
T *Morozovella velascoensis*	55.20	E3	
T *Morozovella acuta*	55.39		
B *Morozovella gracilis*	55.39		
B *Igorina broedermanni*	55.39		
B *Morozovella marginodentata*	55.54		
B *Pseudohastigerina wilcoxensis*	55.81	E2	
B *Globanomalina australiformis*	55.96		
B *Acarinina sibaiyaensis*	55.96	E1	
Paleocene/Eocene boundary	56.00		Vandenberghe et al., 2012
T *Globanomalina pseudomenardii*	57.10	P5	
B *Morozovella subbotinae*	57.10		
T *Acarinina mckannai*	57.66		
T *Acarinina acarinata*	57.66		
B *Acarinina soldadoensis*	57.79	P4c	
B *Acarinina coalingensis*	57.79		

Table T8 (continued).

Event	Age (Ma)	Base of biozone	References for biozones and age estimates
B *Morozovella aequa*	57.79		
T *Acarinina subsphaerica*	58.44		
B *Acarinina mckannai*	60.43		
T *Parasubbotina variospira*	60.52	P4b	
B *Acarinina acarinata*	60.52		
B *Acarinina subsphaerica*	60.52		
B *Globanomalina pseudomenardii*	60.73	P4a	
B *Igorina albeari*	61.33	P3b	
B *Morozovella velascoensis*	61.33		
B *Acarinina strabocella*	61.77		
B *Morozovella conicotruncata*	62.22		
B *Morozovella angulata*	62.29	P3a	
B *Igorina pusilla*	62.29		
B *Morozovella praeangulata*	62.46		
B *Praemurica uncinata*	62.60	P2	
B *Globanomalina compressa*	63.90	P1c	
B *Praemurica inconstans*	63.90		
B *Parasubbotina varianta*	64.02		
B *Subbotina triloculinoides*	65.25	P1b	
T *Parvularugoglobigerina eugubina*	65.72	P1a	
B *Parasubbotina pseudobulloides*	65.75		
B *Parvularugoglobigerina extensa*	65.91		
B *Parvularugoglobigerina eugubina*	65.96	Pα	
Late Cretaceous/Paleocene boundary	66.00		Vandenberghe et al., 2012; Husson et al., 2011
T Cretaceous planktonic foraminiferal fauna	66.00	P0	Within C29r, ~50% from top
T *Abathomphalus mayaroensis*	66.26	Phan	Maastrichtian PF biozones
T *Gansserina gansseri*	66.40		
T *Contusotruncana patelliformis*	66.64		
B *Pseudoguembelina hariaensis*	67.25	Phar	
T *Abathomphalus intermedia*	67.28		
T *Globotruncana linneiana*	68.32		
T *Globotruncana bulloides*	68.77		
T *Rugoglobigerina pennyi*	68.81		
T *Contusotruncana fornicata*	69.08		
B *Abathomphalus mayaroensis*	69.13	Amay	
B *Pseudotextularia elegans*	69.50		
B *Planoglobulina acervulinoides*	70.00		
B *Rugoglobigerina pennyi*	70.09	Rfru	

VG = very good (no breakage or dissolution).

G = good (majority of specimens complete, with minor dissolution and/or breakage and no significant enlargement of the areolae or dissolution of frustule rims detected).

M = moderate (minor but common areolae enlargement and dissolution of frustule rims, with a considerable amount of broken specimens).

P = poor (strong dissolution or breakage, some specimens unidentifiable, strong dissolution of frustule rims and areolae enlargement).

VP = very poor (very strong dissolution or breakage, most specimens unidentifiable).

Radiolarians

Cenozoic low-latitude radiolarian taxonomy and zonation followed that of Kamikuri and Wade (2012), Nigrini and Moore (1979), Nigrini and Sanfilippo (2001), Sanfilippo and Nigrini (1998), Sanfilippo et al. (1985), and Takahashi (1991). Full taxonomic lists and zonal assignments can be found in these references. For an explanation of evolutionary transitions, see Sanfilippo and Nigrini (1998). The zonal schemes of Sanfilippo and Nigrini (1998; codes RN and RP), Nigrini et al. (2006; codes RN and RP), and Kamikuri and Wade

Table T9. Age estimates of diatom and silicoflagellate biohorizons, Expedition 362. T = top, Tc = top common, Ta = top absence, B = base, Bc = base common, Ba = base absence, Ai = abundance increase. (Continued on next two pages.) **Download table in .csv format.**

Event	Age (Ma)	Base of biozone	References for biozones and age estimates
T *Fragilariopsis fossilis*	0.55		Fourtanier, 1991a
T *Mesocena elliptica*	0.79		Schrader, 1974
T *Mesocena quadrangula*	0.85		Fourtanier, 1991a
Tc *Fragilariopsis fossilis*	0.94		Fourtanier, 1991a
T *Rhizosolenia matuyamai*	1.02	*Fragilariopsis doliolus*	Barron, 1992
T *Fragilariopsis reinholdii*	1.04		Fourtanier, 1991a
B *Rhizosolenia matuyamai*	1.20		Barron, 1992
Tc *Fragilariopsis reinholdii*	1.24		Fourtanier, 1991a
T *Rhizosolenia praebergonii* var. *robusta*	1.66		Fourtanier, 1991a
T *Rhizosolenia praebergonii*	1.66		Barron, 1992
Ai *Shionodiscus oestrupii*	1.92	*Fragilariopsis reinholdii*	Baldauf, 1985
B *Fragilariopsis doliolus*	2.12		Fourtanier, 1991a
T *Thalassiosira convexa*	2.18		Barron, 1992
Pliocene/Pleistocene boundary	2.59		Hilgen et al., 2012
T *Nitzschia jouseae*	2.71	*Rhizosolenia praebergonii*	Barron, 1992
B *Rhizosolenia praebergonii*	3.13		Barron, 1992
T *Actinocyclus ellipticus* f. *lanceolata*	3.35		Barron, 1992
Ai *Thalassiosira convexa* var. *aspinosa*	3.68		Baldauf, 1985
B *Thalassiosira convexa* var. *convexa*	3.84		Barron, 1992
B *Asteromphalus elegans*	4.21		Barron, 1992
T *Fragilariopsis cylindrica*	4.69		Barron, 1992
B *Nitzschia jouseae*	4.93	*Nitzschia jouseae*	Barron, 1992
Miocene/Pliocene boundary	5.33		Hilgen et al., 2012
T *Thalassiosira miocenica*	5.69		Barron, 1992
B *Shionodiscus oestrupii*	5.69		Barron, 1992
T *Asterolampra acutiloba*	6.03		Barron, 1992
T *Fragilariopsis miocenica*	6.28		Barron, 1992
T *Thalassiosira praeconvexa*	6.61		Barron, 1992
B *Thalassiosira miocenica*	6.91	*Thalassiosira convexa*	Barron, 1992
B *Thalassiosira convexa* var. *aspinosa*	6.91		Barron, 1992
B *Thalassiosira praeconvexa*	7.08		Barron, 1992
T *Nitzschia porteri*	7.53	*Fragilariopsis miocenica*	Barron, 1992
B *Fragilariopsis miocenica*	7.60		Barron, 1992
T *Rossiella paleacea*	7.66		Barron, 1992
T *Thalassiosira burckliana*	7.84		Barron, 1992
B *Fragilariopsis reinholdii*	8.15		Barron, 1992
T *Actinocyclus ellipticus* var. *javanica*	8.25		Barron, 1992
B *Alveus marina*	8.29	*Nitzschia porteri*	Barron, 1992
B *Fragilariopsis cyclindrica*	8.43		Barron, 1992
T *Thalassiosira yabei*	8.43		Barron, 1992
B *Azpeitia nodulifera* var. *cyclopus*	8.58		Barron, 1992
T *Thalassiosira yabei* var. *elliptica*	8.77		Barron, 1992
B *Thalassiosira yabei* var. *elliptica*	8.99		Barron, 1992
B *Fragilariopsis fossilis*	8.99		Barron, 1992
B *Thalassiosira burckliana*	9.09		Barron, 1992
T *Azpeitia vetustissimus* var. *javanica*	9.48	*Thalassiosira yabei*	Barron, 1992
B *Azpeitia vetustissimus* var. *javanica*	9.68		Barron, 1992
T *Actinocyclus moronensis*	9.78		Barron, 1992
B *Actinocyclus ellipticus* f. *lanceolata*	10.62		Barron, 1992
T *Coscinodiscus tuberculatus*	10.79		Barron, 1992
T *Cavitatus jouseanus*	11.04	*Actinocyclus moronensis*	Barron, 1992
T *Craspedodiscus coscinodiscus*	11.21		Barron, 1992
B *Rossiella paleacea* var. *elongata*	11.21		Barron, 1992
T *Crucidenticula punctata*	11.21		Barron, 1992
B *Thalassionema robusta*	11.21		Barron, 1992
T *Coscinodiscus gigas* var. *diorama*	11.30		Barron, 1992
T *Actinocyclus ellipticus* var. *spiralis*	11.39		Barron, 1992
B *Hemidiscus cuniformis*	11.67		Barron, 1992
B *Rossiella praepaleacea*	11.96		Barron, 1992
B *Coscinodiscus temperei* var. *delicata*	12.01	*Craspedodiscus coscinodiscus*	Barron, 1992
T *Actinocyclus ingens*	12.01		Barron, 1992

Table T9 (continued). (Continued on next page.)

Event	Age (Ma)	Base of biozone	References for biozones and age estimates
T *Cestodiscus pulchellus*	12.08		Barron, 1992
B *Nitzschia porterii*	12.15		Barron, 1992
T *Crucidenticula nicobarica*	12.54		Barron, 1992
T *Annellus californicus*	12.69	*Coscinodiscus gigas* var. *diorama*	Barron, 1992
T *Azpeitia salisburyana*	12.78		Barron, 1992
B *Coscinodiscus gigas* var. *diorama*	12.86		Barron, 1992
T *Araniscus lewisianus*	13.01		Barron, 1992
B *Denticulopsis punctata*	13.17		Barron, 1992
T *Thalassiosira tappanae*	13.41		Barron, 1992
B *Azpeitia nodulifera*	13.46		Barron, 1992
B *Thalassiosira grunowii*	13.79		Barron, 1992
B *Triceratium cinnamoneum*	13.87		Barron, 1992
T *Cestodiscus pulchellus* var. *maculatus*	13.92	*Araniscus lewisianus*	Barron, 1992
B *Actinocyclus ellipticus* var. *spiralis*	14.16		Barron, 1992
T *Cestodiscus peplum*	14.16		Barron, 1992
B *Thalassiosira tappanae*	14.55		Barron, 1992
T *Coscinodiscus blysmos*	14.55		Barron, 1992
B *Actinocyclus ingens*	15.36	*Cestodiscus peplum*	Barron, 1992
B *Cestodiscus peplum*	16.15		Barron, 1992
B *Crucidenticula kanaye*	16.64		Barron, 1992
T *Thalassiosira bukryi*	16.74		Barron, 1992
T *Coscinodiscus rhombicus*	17.19		Barron, 2006
B *Coscinodiscus blysmos*	17.34		Barron, 2006
T *Crucidenticula ikibei*	17.34	*Crucidenticula nicobarica*	Barron, 2006
B *Crucidenticula nicobarica*	17.44		Barron, 1992
B *Azpeitia salisburyana*	17.47		Barron, 2006
T *Coscinodiscus lewisianus* var. *robustus*	17.47		Barron, 2006
T *Azpeitia bukryi*	17.47		Barron, 2006
T *Thalassiosira spinosa*	17.62		Barron, 1992
B *Craspedodiscus coscinodiscus*	17.69		Barron, 2006
B *Annellus californicus*	17.69		Barron, 2006
T *Triceratium pileus*	17.82		Barron, 2006
B *Crucidenticula ikibei*	17.97		Barron, 2006
B *Crucidenticula sawamurae*	18.19		Barron, 2006
T *Bogorovia puncticulata*	18.19		Barron, 2006
B *Cestodiscus kugleri*	18.43		Barron, 2006
T *Thalassiosira praefraga*	18.66		Barron, 2006
B *Cestodiscus pulchellus* var. *maculatus*	18.79		Barron, 2006
T *Actinocyclus radionovae*	18.79		Barron, 2006
T *Actinocyclus jouseae*	18.79		Barron, 2006
B *Cestodiscus pulchellus* var. *maculatus*	18.79		Barron, 2006
T *Actinocyclus barronii*	18.79		Barron, 2006
B *Triceratium pileus*	18.92	*Triceratium pileus*	Barron, 2006
T *Craspedodiscus elegans*	19.06		Barron, 2006
B *Cestodiscus ovalis*	19.20		Barron, 2006
B *Nitzschia maleinterpretaria*	19.34		Barron, 2006
B *Coscinodiscus lewisianus* var. *robustus*	19.48		Barron, 2006
T *Azpeitia gombosii*	19.48		Barron, 2006
B *Actinocyclus barronii*	19.48		Barron, 2006
B *Actinocyclus jouseae*	19.62		Barron, 2006
T *Actinocyclus praellipticus*	19.62		Barron, 2006
T *Actinocyclus hajosiae*	19.75		Barron, 2006
T *Azpeitia oligocenica*	19.83		Barron, 1992
T *Rossiella fennerae*	19.89		Barron, 2006
T *Melosira architecturalis*	19.91	*Coscinodiscus elegans*	Barron, 1992
T *Bogorovia veniamini*	20.02		Barron, 2006
T *Bogorovia barronii*	20.02		Barron, 2006
B *Thalassiosira fraga*	20.42		Barron, 2006
T *Diestephanisira architecturalis*	20.42		Barron, 2006
T *Azpeitia oligocenica*	20.54		Barron, 2006
T *Actinocyclus mutabilis*	20.65		Barron, 2006
T *Cestodiscus trochus*	20.81		Barron, 2006
B *Actinocyclus praellipticus*	20.81		Barron, 2006
B *Bogorovia puncticulata*	20.81		Barron, 2006
B *Rossiella paleacea*	21.08		Barron, 2006
B *Actinocyclus radionovae*	21.29		Barron, 2006
B *Actinocyclus hajosiae*	21.35		Barron, 2006
B *Actinocyclus mutabilis*	21.41		Barron, 2006
B *Cestodiscus pulchellus* s.s.	21.41		Barron, 2006
T *Rossiella symmetrica*	21.47		Barron, 2006
T *Actinocyclus nigriniae*	21.53		Barron, 2006
T *Rossiella fourtanierae*	21.71		Barron, 2006
B *Cestodiscus umbonatus*	21.71		Barron, 2006
B *Cestodiscus quadratus*	21.71		Barron, 2006
T *Thalassiosira primalabiata*	21.77		Barron, 2006
B *Actinocyclus nigriniae*	21.85		Barron, 2006
B *Azpeitia praenodulifera*	21.85		Barron, 2006
T *Bogorovia gombosii*	21.93		Barron, 2006
B *Bogorovia barronii*	22.12		Barron, 2006
B *Thalassiosira spumellaroides*	22.80		Barron, 2006
B *Thalassiosira leptopus*	23.02		Barron, 2006
B *Rossiella fourtanierae*	23.02		Barron, 2006
Oligocene/Miocene boundary	23.03		Hilgen et al., 2012
T *Rocella schraderi*	23.32		Barron, 2006
T *Coscinodiscus lewisianus* var. *rhomboides*	23.32		Barron, 2006
T *Rocella gelida*	23.40		Barron, 2006
B *Thalassiosira praefraga*	23.40		Barron, 2006
T *Rocella gelida*	23.45	*Rossiella fennerae*	Barron et al., 2004
T *Coscinodiscus lewisianus* var. *rhomboides*	23.45		Barron et al., 2004
Tc *Rossiella fennerae*	23.97		Barron et al., 2004
T *Rocella vigilans*	24.05		Barron et al., 2004
T *Rocella princeps*	24.82		Barron et al., 2004
B *Craspedodiscus barronii*	24.92		Barron et al., 2004
B *Rocella schraderi*	25.00		Barron et al., 2004
B *Coscinodiscus lewisianus* var. *rhomboides*	25.14		Barron et al., 2004
B *Rocella gelida*	25.14	*Rocella gelida*	Barron et al., 2004
B *Rocella princeps*	25.38		Barron et al., 2004
T *Kozloviela minor*	27.21		Barron et al., 2004
B *Coscinodiscus lewisianus* var. *levis*	27.81	*Bogorovia veniamini*	Barron et al., 2004
B *Bogorovia veniamini*	27.81		Barron et al., 2004
T *Baxteriopsis brunii*	27.81		Barron et al., 2004
Tc *Cestodiscus trochus*	28.07		Barron et al., 2004
B *Coscinodiscus rhombicus*	28.17		Barron et al., 2004
B *Cavitatus rectus*	28.17		Barron et al., 2004
B *Kozloviella minor*	28.31		Barron et al., 2004
B *Cavitatus jouseana*	28.31		Barron et al., 2004
B *Rossiella symmetrica*	28.75		Barron et al., 2004
B *Rocella vigilans*	29.66	*Rocella vigilans*	Barron et al., 2004
Tc *Cestodiscus robustus*	30.77		Barron et al., 2004
T *Skeletonemopsis barbadensis*	30.95		Barron et al., 2004
T *Cestodiscus convexus*	30.95		Barron et al., 2004
B *Cavitatus miocenicus*	31.12		Barron et al., 2004
B *Thalassionema* cf. *nitzschiodes*	31.48		Barron et al., 2004
T *Coscinodiscus excavatus* var. *semilunis*	31.72		Barron et al., 2004
B *Coscinodiscus excavatus* var. *semilunis*	32.48		Barron et al., 2004
T *Cestodiscus reticulatus*	32.48		Barron et al., 2004
B *Thalassiothrix* cf. *primitiva*	33.18		Barron et al., 2004
B *Cestodiscus reticulatus*	33.18	*Cestodiscus trochus*	Barron et al., 2004
T *Coscinodiscus excavatus*	33.20		Barron et al., 2004
T *Cestodiscus antarcticus*	33.30		Barron et al., 2015
T *Cestodiscus* sp. 2	33.4		Barron et al., 2015
B *Cestodiscus robustus*	33.7		Barron et al., 2015
B *Hemiaulus barbadensis*	33.7	*Coscinodiscus excavatus*	Barron et al., 2015
B *Coscinodiscus excavatus*	33.8		Barron et al., 2015
T *Kozloviella subrotunda*	33.8		Barron et al., 2015
Eocene/Oligocene boundary	33.9		Coccioni et al., 1988

Table T9 (continued).

Event	Age (Ma)	Base of biozone	References for biozones and age estimates
B *Cestodiscus* sp. 2	33.9		Barron et al., 2015
T *Coscinodiscus decrescens*	33.9		Barron et al., 2015
B *Azpeitia oligocenica* var. *nodosa*	34.0		Barron et al., 2015
B *Trinacria subcapitata*	34.0		Barron et al., 2015
T *Hemiaulus gracilis*	34.1		Barron et al., 2015
B *Cestodiscus trochus*	34.2		Barron et al., 2015
B *Azpeitia oligocenica*	34.4		Barron et al., 2015
B *Cestodiscus demergitus*	34.4		Barron et al., 2015
B *Cestodiscus convexus*	34.5		Barron et al., 2015
B *Hemiaulus gracilis*	34.5		Barron et al., 2015
T *Brightwellia imperfecta*	34.7		Barron et al., 2015
B *Cestodiscus antarcticus*	35.0		Barron et al., 2015
T *Cestodiscus fennerae*	35.1		Barron et al., 2015
T *Cestodiscus pulchellus* var. *novazealandica*	35.1		Barron et al., 2015
B *Cestodiscus stokesianus*	35.1		Barron et al., 2015
B *Chaetoceros asymmetricus*	35.1	*Baxteriopsis brunii*	Barron et al., 2015
B *Baxteriopsis brunii*	35.2		Barron et al., 2015
T *Cestodiscus spinifer*	35.3		Barron et al., 2015
T *Azpeitia tuberculata*	35.3		Barron et al., 2015
T *Hemiaulus grassus*	35.9	*Cestodiscus fennerae*	Barron et al., 2015
B *Cestodiscus fennerae*	36.6		Barron et al., 2015
B *Hemiaulus altar*	36.8		Barron et al., 2015
T *Hemiaulus gondolaformis*	36.9		Barron et al., 2015
B *Skeletonemopsis barbadensis*	37.0		Barron et al., 2015
B *Coscinodiscus hajosiae*	37.4		Barron et al., 2015
B *Ethmodiscus rex*	37.6		Barron et al., 2015
T *Hemiaulus alatus*	37.7		Barron et al., 2015
B *Cestodiscus spinifer*	38.1		Barron et al., 2015
B *Cestodiscus pulchellus* var. *novazealandica*	38.9	*Cestodiscus pulchellus* var. *novazelandica*	Barron et al., 2015
T *Triceratium inconspicuum*	38.9		Barron et al., 2015
T *Triceratium kanayae*	38.9		Barron et al., 2015
B *Azpeitia crenuloides*	39.3		Barron et al., 2015
T *Brightwellia hyperborea*	39.3		Barron et al., 2015
T *Abas wittii*	39.4		Barron et al., 2015
T *Craspedodiscus umbonatus*	39.6		Barron et al., 2015
B *Kozloviella subrotunda*	39.7		Barron et al., 2015
B *Actinoptychus splendens*	39.8		Barron et al., 2015
T *Triceratium barbadense*	40.3		Barron et al., 2015
B *Asterolampra marylandica*	40.4	*Triceratium inconspicuum*	Barron et al., 2015
T *Craspedodiscus oblongus*	40.4		Barron et al., 2015
T *Pyxilla gracilis*	40.4		Barron et al., 2015
B *Riedelia claviger*	41.5	*C. oblongus–B. imperfecta*	Barron et al., 2015
B *Brightwellia imperfecta*	41.8		Barron et al., 2015
T *Pyxilla caputavis*	41.8		Barron et al., 2015
B *Hemiaulus exiguus*	42.0	*Hemiaulus gondolaformis*	Barron et al., 2015
B *Hemiaulus gondolaformis*	43.6		Barron et al., 2015
B *Asterolampra affinis*	43.7		Barron et al., 2015
B *Asterolampra grevillei*	43.7		Barron et al., 2015
B *Craspedodiscus umbonatus*	44.0		Barron et al., 2015
B *Hemiaulus alatus*	44.4	*Hemiaulus alatus*	Barron et al., 2015
B *Hemiaulus lyriformis*	44.7		Barron et al., 2015
T *Trinacria simulacrum*	44.9		Barron et al., 2015
B *Hemiaulus grassus*	45.4		Barron et al., 2015
B *Pyxilla caputavis*	45.6	*Pyxilla caputavis*	Barron et al., 2015
T *Triceratium polycystinorum*	45.8		Barron et al., 2015
T *Trochosira trochlea*	45.9		Barron et al., 2015
T *Coscinodiscus eomonoculus*	46.0		Barron et al., 2015
B *Azpeitia tuberculata*	46.2		Barron et al., 2015
B *Hemiaulus dubius*	46.2		Barron et al., 2015
B *Hemiaulus polycistinorum* var. *mesolepta*	46.2		Barron et al., 2015
B *Asterolampra insignis*	46.3		Barron et al., 2015
B *Triceratium barbadense*	46.3		Barron et al., 2015
B *Rocella praenitida*	46.5		Barron et al., 2015
B *Pyxilla reticulata*	46.6		Barron et al., 2015
T *Hemiaulus inaequilaterus*	48.1		Barron et al., 2015
B *Triceratium inconspicuum*	48.4	*Triceratium kanaye*	Barron et al., 2015
B *Triceratium kanayae*	48.4		Barron et al., 2015
B *Coscinodiscus eomonoculus*	50.4		Barron et al., 2015
T *Craspedodiscus undulatus*	50.4	*Craspedodiscus oblongus*	Barron et al., 2015
B *Craspedodiscus oblongus*	50.8		Barron et al., 2015
T *Hemiaulus incurvus*	52.0	*Craspedodiscus undulatus*	Barron et al., 2015
B *Craspedodiscus undulatus*	52.3		Barron et al., 2015
B *Brightwellia hyperborea*	53.0		Barron et al., 2015
B *Coscinodiscus bulliens*	53.0		Barron et al., 2015
T *Hemiaulus peripterus* var. *longispina*	53.4		Barron et al., 2015
B *Abas wittii*	53.5		Barron et al., 2015
B *Triceratium polycystinorum*	53.5		Barron et al., 2015
B *Pyxilla gracilis*	54.0	*Pyxilla gracilis*	Barron et al., 2015
T *Trinacria exsculpta*	54.0		Barron et al., 2015
T *Trinacria regina*	55.0		Barron et al., 2015
T *Trochosira radiata*	55.0		Barron et al., 2015
B *Hemiaulus peripterus* var. *longispina*	55.3		Barron et al., 2015
B *Coscinodiscus descerens*	55.3		Barron et al., 2015
B *Rhizosolenia setigera*	55.4		Barron et al., 2015
T *Triceratium mirabile*	55.8		Barron et al., 2015
T *Triceratium heibergii*	55.9		Barron et al., 2015
Paleocene/Eocene boundary			Vandenberghe et al., 2012
B *Hemiaulus inaequilaterus*	56.1		Barron et al., 2015
B *Trinacria exsculpta*	56.4		Barron et al., 2015
T *Trochosira gracillima*	56.6		Barron et al., 2015
T *Coscinodiscus cruxii*	56.7		Barron et al., 2015
T *Trinacria simulacroides*	56.7		Barron et al., 2015
T *Trinacria aries*	56.8		Barron et al., 2015
T *Hemiaulus kristoffersenii*	56.9		Barron et al., 2015
T *Hemiaulus nocchiae*	56.9		Barron et al., 2015
T *Pterotheca clavata*	56.9		Barron et al., 2015
T *Trinacria conifera*	56.9		Barron et al., 2015
T *Trinacria deciusi*	56.9		Barron et al., 2015
B *Hemiaulus subactus*	57.1		Barron et al., 2015
T *Trochosira marginata*	57.3		Barron et al., 2015
T *Hyalodiscus ambiguus*	57.5		Barron et al., 2015
T *Triceratium gombosii*	57.5		Barron et al., 2015
T *Triceratium gombossi* var. A	59.27		Fourtanier, 1991b
B *Triceratium gombossi*	59.57	*Hemiaulus incurvus*	Fourtanier, 1991b
B *Hemiaulus incurvus*	60.38		Fourtanier, 1991b
T *Hemiaulus peripterus* var. *peripterus*	60.61	*Hemiaulus peripterus*	Fourtanier, 1991b
Late Cretaceous/Paleocene boundary	66.0		Vandenberghe et al., 2012; Husson et al., 2011

(2012; code RP) were used for Cenozoic radiolarian biostratigraphy. The Maastrichtian radiolarian biostratigraphy is represented in the global Late Cretaceous biozonation following Hollis (2002; code RK), De Weaver et al. (2001), and O'Dogherty et al. (2009) systematics. All biohorizons and biozones were modified where necessary according to the Expedition 362 timescale. Modified diatom biohorizons and biozones are detailed in Table **T10** and shown in Figure **F34**. Accuracy of the correlation depends on many factors including core recovery, preservation, reworking, consistent recognition of taxa, geographical variability of taxa, and absence from or presence in some regions.

Figure F33. Diatom biozones and biohorizons defining biozone boundaries, Expedition 362. T = top, B = base. A. 0–23 Ma. B. 23–46 Ma. (Continued on next page.)

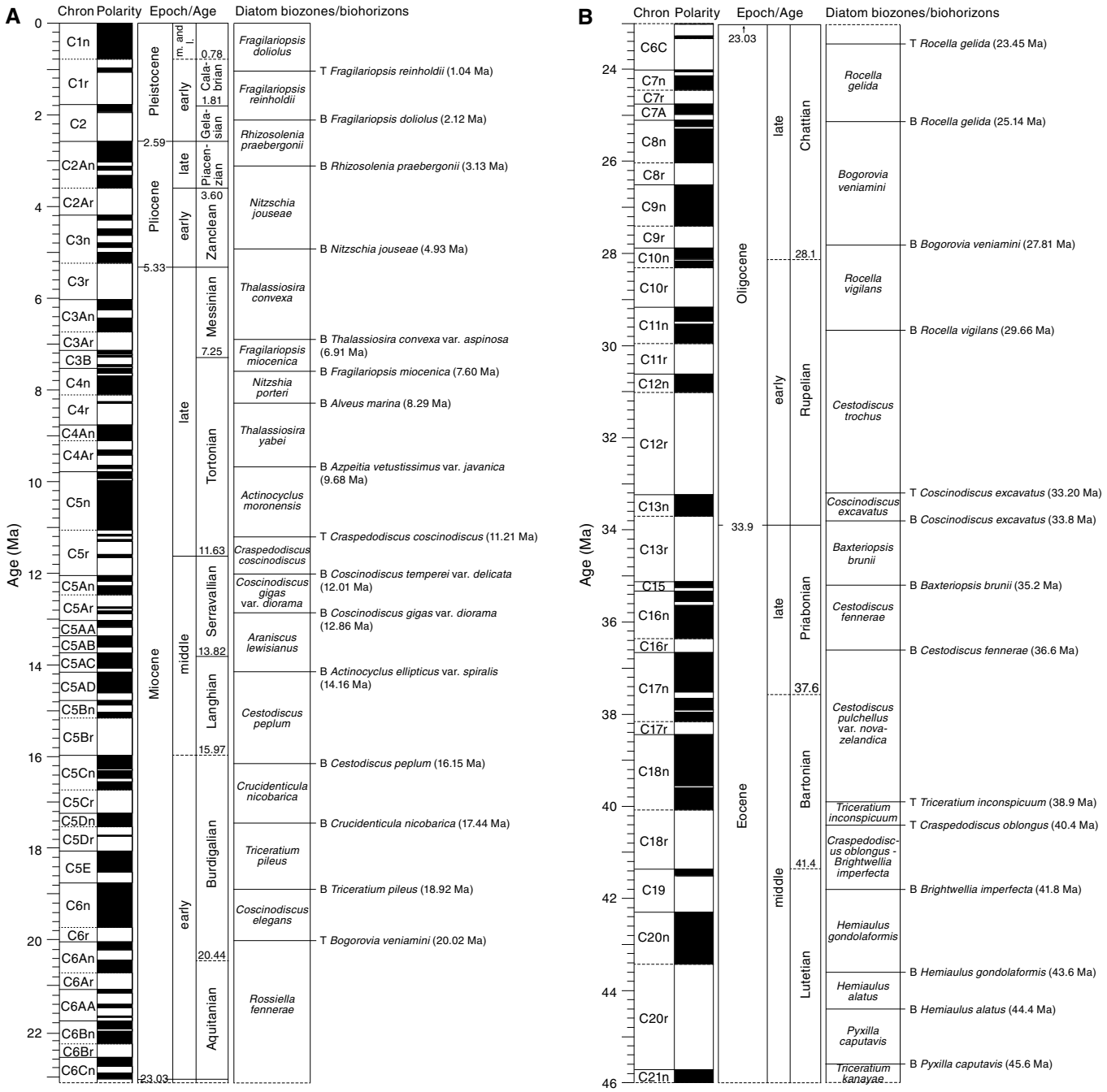

The age estimate of the base of *Diartus hughesi* was originally derived from Deep Sea Drilling Project Site 214 in the Indian Ocean (Johnson and Nigrini, 1985). This biohorizon occurs at 153.96 ± 0.75 mbsf in Core 22-214-17R (Gartner, 1974). The nannofossil *Catinaster calyculus* has its total range confined to Core 17R (Gartner, 1974), between 161.02 ± 0.98 mbsf (10.71 Ma) and 153.30 ± 0.75 mbsf (9.64 Ma). Linear interpolation between top and base *C. calyculus* results in an age of base *D. hughesi* of 9.73 Ma on the Expedition 362 timescale.

Samples were disaggregated by treatment with 10% H_2O_2 for 2 h, or until effervescence subsided. The samples were then washed through a 63 µm sieve. A second treatment with a 10% solution of HCl was used if any carbonate was present. While wet, residue samples were mounted by pipetting onto a microscope slide and the remainder residue was dried for scanning electron microscope (SEM) analysis. A few drops of mounting medium, Norland optical adhesive 61 (NOA 61) were applied to the dry slide, followed by a 22 mm × 40 mm glass coverslip. After curing under ultraviolet light, slides were examined using Zeiss Axiophot light microscopes under phase contrast, brightfield, and cross-polarized light at 50× and 100× magnification.

For the treatment of clayey sediment that contained pyritized radiolarians, samples were boiled for 4–5 min with tetrasodium phosphate before being further processed with 10% HCl for 2 h, or

Figure F33 (continued). C. 46–70 Ma.

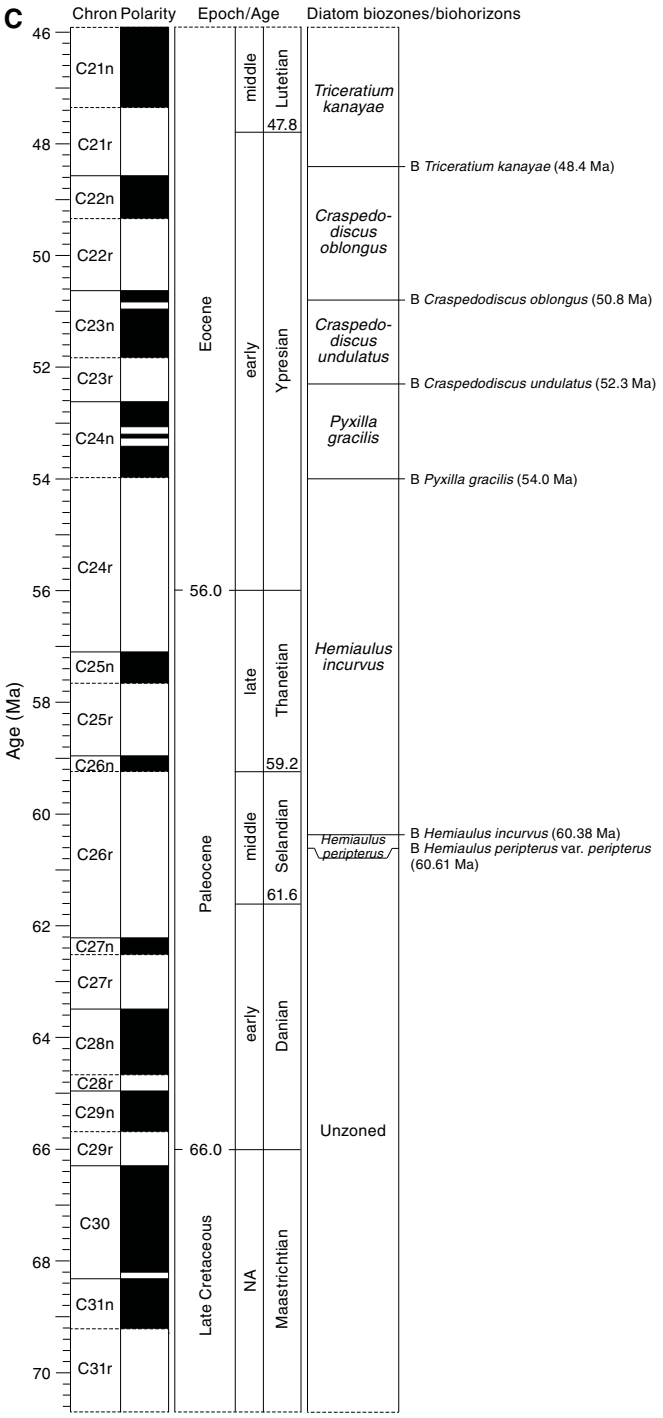

until effervescence subsided. Freed skeletons were frequently removed to avoid oxidation, and mechanical agitation (ultrasonic device and strong flows while sieving) was avoided. Cleaning with H_2O_2 was avoided when dealing with pyritized radiolarians. Sample residues were observed under a Zeiss Discovery V8 microscope, and representative radiolarians were picked from a tray and mounted on aluminum stubs. Stubs were sputter-coated with gold for 3–4 min to enhance conductivity. Specimens were then examined and photographed with a Hitachi-TM3030 desktop SEM at 10

Table T10. Age estimates of radiolarian biohorizons, Expedition 362. * = lower Paleocene zones that have been defined using material from New Zealand (Hollis, 2002). T = top, Tc = top common, Ta = top absence, B = base, Bc = base common, Ba = base absence. (Continued on next two pages.) **Download table in .csv format.**

Event	Age (Ma)	Base of biozone	References for biozones and age estimates
B *Buccinosphaera invaginata*	0.18	RN17	Pleistocene (T RN13) through Miocene (B RN1): Nigrini et al., 2006; Sanfilippo and Nigrini, 1998
T *Stylatractus universus*	0.44	RN16	
B *Collosphaera tuberosa*	0.59	RN15	
T *Lamprocyrtis neoheteroporos*	1.08		
T *Anthocyrtidium angulare*	1.21	RN14	
B *Lamprocyrtis nigriniae*	1.31		
T *Pterocanium prismatium*	2.04	RN13	
Pliocene/Pleistocene boundary	2.59		Hilgen et al., 2012
T *Anthocyrtidium jenghisi*	2.74	RN12b	
T *Stichocorys peregrina*	2.87	RN12a	
B *Theocorythium trachelium trachelium*	2.90		
T *Phormostichoartus fistula*	3.49	RN11b	
T *Phormostichoartus doliolum*	3.89	RN11a	
T *Didymocyrtis penultima*	4.24	RN10	
Miocene/Pliocene boundary	5.33		Hilgen et al., 2012
T *Stichocorys delmontensis*	7.78		
B *Stichocorys peregrina*	7.78	RN9	
T *Diartus hughesi*	8.39	RN8	
T *Didymocyrtis antepenultima*	8.51		
T *Diartus petterssoni*	8.84	RN7	
B *Phormostichoartus doliolum*	8.87		Lazarus et al., 1995
T *Stichocorys wolffii*	8.87		Lazarus et al., 1995
B *Diartus hughesi*	9.73		This study
T *Cyrtocapsella japonica*	9.86		Lazarus et al., 1995
B *Didymocyrtis antepenultima*	10.01		
T *Carpocanopsis cristata*	10.68		Lazarus et al., 1995
T *Dorcadospyris alata*	12.50		
B *Diartus petterssoni*	12.60	RN6	
T *Calocycletta costata*	15.00		
T *Didymocyrtis violina*	15.00		
T *Dorcadospyris forcipata*	15.03		
Dorcadospyris alata < *D. dentata*	15.03	RN5	
T *Lychnocanoma elongata*	15.03		
T *Didymocyrtis prismatica*	16.73		
B *Acrocubus octopylus*	17.11		
B *Carpocanopsis cristata*	17.16		
B *Calocycletta costata*	17.40	RN4	
B *Liriospyris stauropora*	17.72		
B *Dorcadospyris dentata*	18.22		
T *Dorcadospyris ateuchus*	18.64		
B *Siphostichartus corona*	18.64		
B *Stichocorys wolffi*	18.64	RN3	
T *Dorcadospyris simplex* s.s.	18.76		
B *Carpocanopsis bramlettei*	19.34		
B *Didymocyrtis tubaria*	19.34		
B *Didymocyrtis violina*	19.34		
B *Stichocorys delmontensis*	19.34		
T *Theocyrtis annosa*	20.05	RN2	
T *Calocycletta serrata*	20.40		
B *Dorcadospyris simplex* s.s.	20.41		
T *Calocycletta robusta*	20.76		
B *Carpocanopsis favosa*	21.11		
B *Cyrtocapsella cornuta*	21.46		
B *Botryostrobus miralestensis*	21.82		
B *Calocycletta serrata*	21.82		
B *Calocycletta virginis*	21.82		
B *Cyrtocapsella tetrapera*	21.82	RN1	
T *Artophormis gracilis*	22.41		
B *Eucyrtidium diaphanes*	23.00		
Oligocene/Miocene boundary	23.03		Hilgen et al., 2012

Table T10 (continued). (Continued on next page.)

Event	Age (Ma)	Base of biozone	References for biozones and age estimates
B *Carpocanopsis cingulata*	25.20		Oligocene (T RP22) through Paleocene (B RP1): Kamikuri and Wade, 2012; Nigrini et al., 2006; Sanfilippo and Nigrini, 1998
B *Lychnocanoma elongata*	25.20	RP22	
B *Calocycletta robusta*	26.10		
B *Dorcadospyris papilio*	25.55		
T *Lithocyclia angusta*	27.70		
B *Theocyrtis annosa*	29.00		
Tristylospyris triceros < *Dorcadospyris ateuchus*	29.10	RP21	
T *Lithocyclia crux*	30.13		
T *Dorcadospyris pseudopapilio*	30.84		
B *Didymocyrtis prismatica*	30.85		
B *Lychnodictyum audax*	30.96		
T *Centrobotrys gravida*	30.91		
B *Centrobotrys petrushevskayae*	30.91		
B *Dorcadospyris pseudopapilio*	31.00		
B *Lithocyclia crux*	31.01		
B *Centrobotrys gravida*	32.40		
Lithocyclia angusta < *L. aristolelis* gr.	33.80	RP20	
Eocene/Oligocene boundary	33.9		Coccioni et al., 1988
T *Cryptocarpium ornatum*	33.80		
T *Lophocyrtis jacchia*	34.57		
T *Calocyclas turris*	34.83		
T *Thyrsocyrtis bromia*	35.18		
T *Calocyclas bandyca*	35.30		
T *Calocyclas hispida*	35.30		
T *Cryptocarpium azyx*	35.30		
T *Lychnocanoma bellum*	35.30		
T *Podocyrtis papalis*	35.30		
T *Thyrsocyrtis lochites*	35.40		
T *Thyrsocyrtis rhizodon*	35.40		
Tc *Thyrsocyrtis tetracantha*	35.40	RP19	
T *Thyrsocyrtis triacantha*	35.51		
T *Podocyrtis goetheana*	36.72		
B *Calocyclas bandyca*	36.90	RP18	
T *Podocyrtis chalara*	37.22		
B *Lychnocanoma amphitrite*	37.40		
T *Calocyclas hispida*	37.58		
B *Calocyclas turris*	37.58		
B *Cryptocarpium azyx*	38.00	RP17	
B *Thyrsocyrtis bromia*	38.50		
B *Thyrsocyrtis tetracantha*	38.50		
T *Theocotylissa ficus*	38.95		
B *Lithocyclia aristotelis* gr.	39.30		
B *Dictyoprora armadillo*	39.65		
B *Dictyoprora pirum*	39.65		
B *Podocyrtis goetheana*	39.90	RP16	
T *Phormocyrtis striata striata*	40.65		
B *Tristylospyris triceros*	40.67		
Podocyrtis chalara < *P. mitra*	41.40	RP15	
T *Podocyrtis trachodes*	41.50		
B *Cryptocarpium ornatum*	41.80		
T *Podocyrtis ampla*	42.01		
T *Eusyringium lagena*	42.30		
B *Sethochytris triconiscus*	42.30		
B *Artophormis barbadensi*	42.69		
T *Podocyrtis fasciolata*	42.69		
T *Podocyrtis helenae*	42.69		
B *Thyrsocyrtis lochites*	42.69		
Podocyrtis mitra < *P. sinuosa*	43.38	RP14	
B *Podocyrtis trachodes*	43.59		
T *Podocyrtis dorus*	43.79		
T *Eusyringium fistuligerum*	44.03		
B *Eusyringium lagena*	44.03		
B *Podocyrtis fasciolata*	44.25		
B *Eusyringium fistuligerum*	44.46		
Podocyrtis ampla < *P. phyxis*	44.46		
T *Theocotyle venezuelensis*	44.46	RP13	
T *Lamptonium fabaeforme chaunothorax*	45.63		
T *Lamptonium fabaeforme constrictum*	45.63		
Podocyrtis phyxis < *P. diamesa*	45.63		
T *Theocotyle conica*	45.63		
T *Theocotyle nigriniae*	45.63		
T *Thyrsocyrtis hirsuta*	45.63		
T *Thyrsocyrtis robusta*	45.63		
B *Eusyringium lagena*	46.21		
T *Thyrsocyrtis tensa*	46.21		
B *Thyrsocyrtis triacantha*	46.21	RP12	
T *Lamptonium fabaeforme fabaeforme*	46.80		
B *Podocyrtis dorus*	46.80		
B *Theocotyle conica*	47.39		
T *Theocotyle cryptocephala*	47.39		
B *Dictyoprora mongolfieri*	47.98	RP11	
T *Podocyrtis acalles*	48.13		
B *Podocyrtis sinuosa*	48.13		
B *Thyrsocyrtis robusta*	48.27		
B *Theocotyle venezuelensis*	48.42		
T *Theocotyle nigriniae*	48.57		
B *Theocotyle cryptocephala*	48.57	RP10	
Spongatractus pachystylus < *S. balbis*	48.86		
T *Lamptonium sanfilippoae*	49.16		
B *Thyrsocyrtis rhizodon*	49.46		
B *Podocyrtis diamesa*	49.75		
B *Lamptonium fabaeforme constrictum*	50.05		
B *Lychnocanoma bellum*	50.05		
T *Phormocyrtis cubensis*	50.05		
T *Phormocyrtis striata exquisita*	50.05		
Phormocyrtis striata striata < *P. striata exquisita*	50.05		
B *Podocyrtis acalles*	50.05	RP9	
T *Bekoma bidartensis*	50.87		
T *Buryella tetradica*	50.87		
T *Pterocodon*(?) *ampla*	50.87		
Theocotylissa ficus < *T. alpha*	51.70		
B *Thyrsocyrtis tensa*	51.70		
B *Calocyclas hispida*	52.52		
B *Buryella clinata*	53.35		
B *Lamptonium sanfilippoae*	53.35		
T *Pterocodon* (?) *anteclinata*	53.35		
B *Spongatractus balbis*	53.35		
B *Theocotyle nigriniae*	53.35		
B *Thyrsocyrtis hirsuta*	53.35	RP8	
B *Theocotylissa alpha*	54.04		
B *Lamptonium fabaeforme chaunothorax*	54.74		
B *Calocycloma castum*	55.40		
B *Lophocyrtis jacchia*	55.44		
B *Pterocodon* (?) *anteclinata*	55.44		Sanfilippo and Blome, 2001
T *Lamptonium pennatum*	55.90		
Paleocene/Eocene boundary	56.0		Vandenberghe et al., 2012
B *Lamptonium fabaeforme fabaeforme*	56.14		
T *Bekoma campechensis*	57.53		
B *Bekoma bidartensis*	58.23	RP7	
B *Pterocodon* (?) *poculum*	59.00		Nishimura, 1992
B *Stylotrochus nitidus*	59.00	RP6c	Nishimura, 1992
Ta *Orbula discipulus*	59.00		Nishimura, 1992
Ba *Orbula discipulus*	60.97	RP6b	Nishimura, 1992
T *Peritiviator* (?) *dumitricai*	60.97		Nishimura, 1992
B *Bekoma campechensis*	61.50	RP6a	Nishimura, 1992
B *Buryella tetradic**	62.20	RP5	Hollis, 2002
B *Amphisphaera coronata**	63.00		Hollis, 2002
B *Buryella foremanae**	63.90	RP4	Hollis, 2002

Table T10 (continued).

Event	Age (Ma)	Base of biozone	References for biozones and age estimates
B *Stichomitra granulata**	64.90	RP3	Hollis, 1997
B *Amphisphaera kina**	65.55	RP2	Hollis, 2002
B *Amphisphaera aotea**	66.00	RP1	Hollis, 2002
Late Cretaceous/Paleocene boundary	66.00		Vandenberghe et al., 2012; Husson et al., 2011
T *Afens liriodes*	66.00		Maastrichtian systematics follows Hollis, 2002; De Wever et al., 2001; O'Dogherty et al., 2009
T *Dictyomitra lamellicostata*	66.00		
B *Dictyomitra lamellicostata*	70.60		
B *Orbiculiforma renillaeformis*	70.60		
B *Siphocampe bassilis*	70.60		
B *Siphocampe daseia*	70.60		
B *Theocapsomma teren*	70.60	RK9	

kV. Images were optimized using Adobe Photoshop. SEM analysis was used to confirm species identification.

When radiolarians were diluted with detrital particles, sample residues were observed under a Zeiss Discovery V8 microscope. SEM analysis was used to confirm species identification.

When possible, relative abundances of individual radiolarian taxa were recorded. Abundance estimates, based on one slide of total radiolarian abundance in each sample, were determined using the following criteria:

A = abundant (>30 specimens per slide traverse).
C = common (6–30 specimens per slide traverse).
F = few (>1–5 specimens per slide traverse).
B = barren (no radiolarians present).

Relative preservation of each radiolarian taxon were noted using the following qualitative criteria:

G = good (individual specimens exhibit little overgrowth, dissolution, or abrasion, but delicate parts of the skeleton are preserved).
M = moderate (dissolution and breakage of individual specimens apparent but identification of species not impaired).
P = poor (substantial overgrowth or infilling, dissolution, or fragmentation, where identification of some species is not possible).

Figure F34. Radiolarian biozones and biohorizons defining biozone boundaries, Expedition 362. T = top, B = base. A. 0–23 Ma. (Continued on next page.)

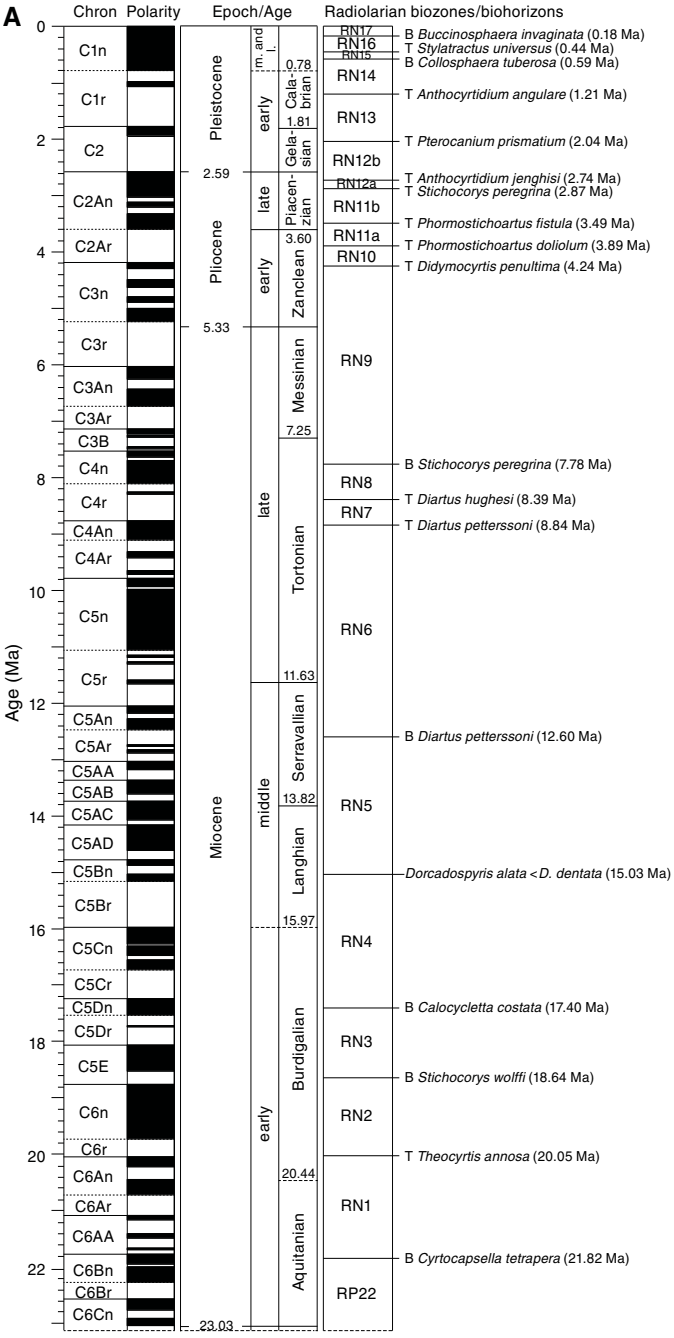

Figure F34 (continued). B. 23–46 Ma. C. 46–70 Ma.

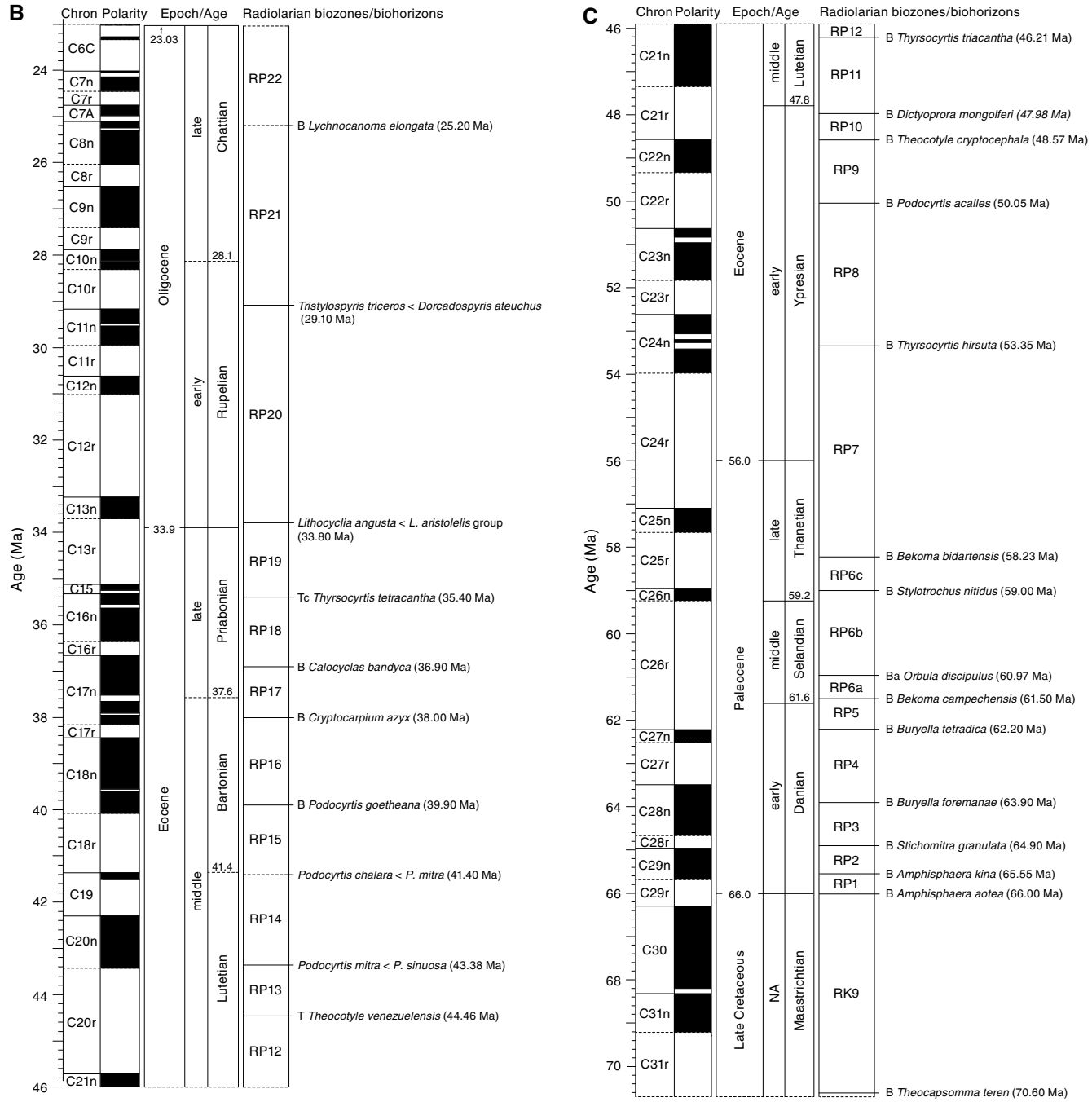

Paleomagnetism

Shipboard paleomagnetism was investigated mainly to determine directions of natural remanent magnetization (NRM) components and downhole variation of magnetic properties. Routine measurements were conducted on archive section halves with stepwise alternating field (AF) demagnetization. Discrete cube and minicore samples were taken from selected working-half sections and measured with stepwise AF and thermal demagnetization. These data were used for core orientation and magnetostratigraphic and relative paleointensity dating (e.g., Guyodo and Valet, 1999; Laj et al., 2000; Channell et al., 2009).

Magnetic measurements

Remanent magnetization was measured using a 2G superconducting rock magnetometer (SRM; 2G Enterprises model 760R) equipped with direct-current superconducting quantum interference devices and an in-line, automated AF demagnetizer capable of reaching a peak field of 80 mT. Ocean drilling cores generally carry secondary overprint remanence components. Common overprints for ocean drilling cores include natural viscous remanent magnetization (VRM) and a steep downward-pointing component imparted by the drill string. To separate overprints from the

characteristic remanence (ChRM), stepwise demagnetization was performed, as described below.

Archive-half sections

Measurements of archive halves were conducted using the new SRM software (IMS-SRM version 9.1) with a nominal sample area parameter of 15.59 cm^2. The interval between measurement points and the measurement speed were selected as 2.5 cm and 10 cm/s, respectively.

We performed successive AF demagnetization using the SRM in-line AF demagnetizer on all split-core archive sections. The in-line AF demagnetizer applies a field to the *x*-, *y*-, and *z*-axes of the SRM in this fixed order (Figure **F35**). Previous reports suggest that higher AF demagnetization fields have produced significant anhysteretic remanent magnetization (ARM) along the *z*-axis of the SRM (e.g., Harris et al., 2013). With this limitation, we used demagnetization steps up to 30 mT to demagnetize the sections. For most of the sediment sections, we performed 4–6 steps from NRM to 25 mT demagnetization. AF demagnetization results were plotted individually as vector plots (Zijderveld, 1967), stereoplots of equal area projections, and downhole variations with depth. We inspected the plots visually to judge whether the remanence after demagnetization at the highest AF step reflects the ChRM and geomagnetic polarity sequence.

Discrete samples

Oriented discrete samples were collected from working-half sections. In soft sediment, discrete samples were taken in plastic "Japanese" Natsuhara-Giken sampling cubes (7 cm^3 sample volume; Figure **F35**). Cubes were pushed into the working half of the core by hand with the "up" arrow on the cube pointing upsection in the core. For indurated intervals, cubes were cut with a table saw and trimmed to fit into the plastic sample cubes. In lithified sediment and hard rock, minicores (~11 cm^3) were taken. Discrete sample locations were chosen in fine-grained intervals where drilling deformation was minimal or not visible.

Discrete samples were subjected to successive AF demagnetization with the DTech AF demagnetizer (model D-2000) and measured on the JR-6A spinner magnetometer before and after 5, 10, 15, 20, 25, 30, 35, 40, 60, and 80 mT AF demagnetization (majority of samples) and to 180 mT (for several high-coercivity samples). We also performed progressive thermal demagnetization using a thermal specimen demagnetizer (ASC Scientific model TD-48SC) for several selected discrete samples up to 575°C. Temperature increments of 25°–100°C were used, depending on the unblocking temperature of each sample. We analyzed the stepwise demagnetization data of the discrete samples by principal component analysis (PCA) to define the ChRM (Kirschvink, 1980). Section-half and discrete data collected on the pass-through SRM and spinner magnetometer, respectively, were uploaded to the LIMS database.

Low-field magnetic susceptibility (κ) measured on whole-round core sections using the WRMSL and archive-half core sections using the SHMSL (see **Physical properties**) was used to reveal the concentration of magnetic minerals and to determine the downhole relative paleointensity (NRM/κ).

Coordinates

All magnetic data are reported relative to the standard IODP orientation conventions: +*x* points into the face of the working half, +*y* points toward the left side of the face of the working half, and +*z* points down section (Figure **F35**). The relationship of the SRM coordinates (*x*-, *y*-, and *z*-axes) to the data coordinates (*x*-, *y*-, and *z*-directions) is as follows: for archive halves, *x*-direction = *x*-axis, *y*-direction = –*y*-axis, and *z*-direction = *z*-axis; for working halves, *x*-direction = –*x*-axis, *y*-direction = *y*-axis, and *z*-direction = *z*-axis. The coordinate systems for the spinner magnetometer (AGICO model JR-6A) and Natsuhara-Giken sampling cubes are shown in Figure **F36**.

Core orientation

Paleomagnetic study of marine sediment cores can be greatly enhanced if the angle between magnetic north and the double-line orientation marked on the core liner can be oriented. Core orientation of APC cores during Expedition 362 was achieved with two orientation tools (Icefield MI-5 multishot and FlexIT tools) mounted on the core barrel. The Icefield MI-5 tool consists of triaxial magnetometers and accelerometers, and the FlexIT tool uses three mutually perpendicular fluxgate magnetic sensors and two perpendicular

Figure F35. A. IODP coordinate systems for paleomagnetic samples (after Richter et al., 2007). B. Natsuhara-Giken sampling cubes (7 cm^3 volume) with sample coordinate system used during Expedition 362. Hatched arrow is parallel to the up arrow on the sample cube and points in the –*z*-direction. C. SRM coordinate system.

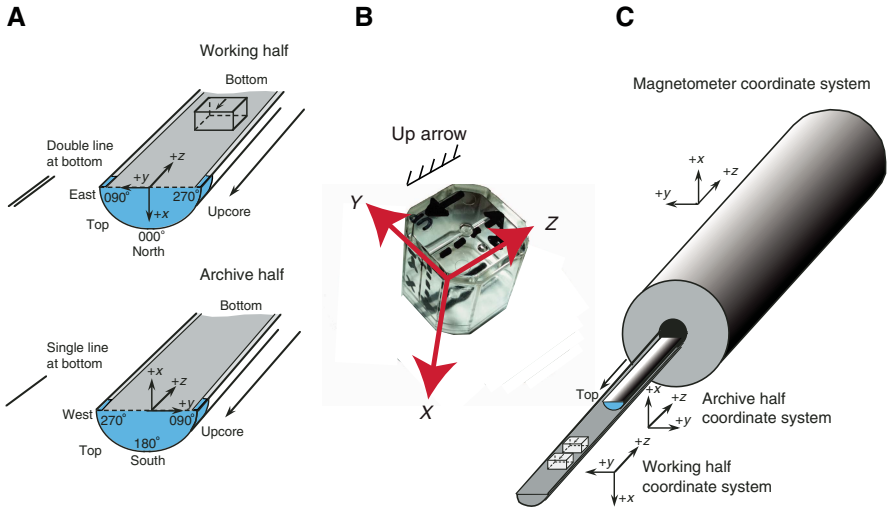

Figure F36. Positioning of discrete samples in the automatic holder of the JR-6A spinner magnetometer.

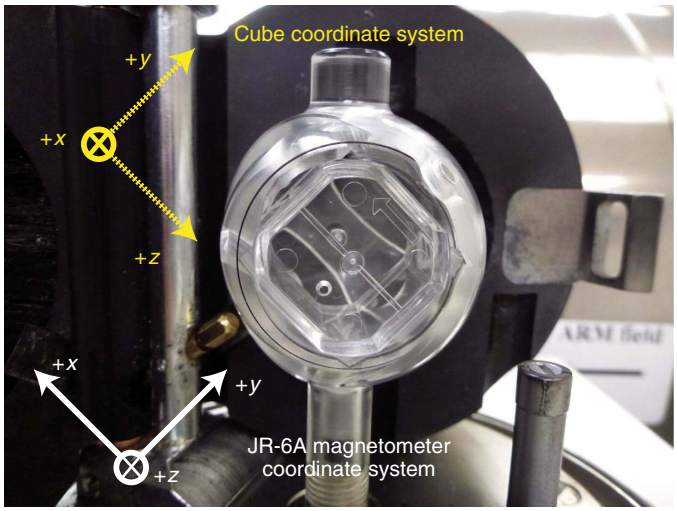

gravity sensors. The information from the magnetometers and sensors allows measuring the azimuth and dip of the hole, as well as the azimuth of the APC core. This azimuth combined with the local magnetic declination allows us to reorient the measured core declinations back to true geographic coordinates. We used the method of Richter et al. (2007) to obtain the azimuthally corrected declination (D_{True}):

$$D_{True} = D_{Observed} + MTF + MIGRF,$$

where

$D_{Observed}$ = the measured declination output from the cryogenic magnetometer.
MTF = the magnetic tool face angle (the angle between magnetic north and the double line orientation mark on the core liner measured in a clockwise manner when the APC fired, see Figure **F37**).
MIGRF = the site-specific deviation of magnetic north from true north.

During orientation, a tool is connected to the core barrel in such a way that the double lines on the core liner are at a fixed and known angle relative to the tool's sensors. This angle has been assumed to be zero as long as these tools have been deployed in ocean drilling history. Previous expeditions have reported that in general these orientation tools have an accuracy of 20°–30°. During Expedition 362, however, a puzzling anomaly was observed in the declinations after core reorientation using the orientation tool data. The declination for the youngest sediment near the seafloor was expected to be near zero based on biostratigraphic and ash ages, yet the corrected declination was near ~180°, indicating an age older than the Bruhnes Chron (0.78 Ma). To track down the possible origin of this anomaly, an experiment with both the Icefield and FlexIT orientation tools was conducted by the IODP technical staff and Siem crew members during the transit back to Site U1481 on 20 September 2016. During the experiment, the tools residing above the core barrel were aligned to the double lines on the core liner (Figure **F37**), which were pointed to the ship's heading direction (which was kept fixed relative to north) (Figure **F38**). The tools were suspended vertically in the derrick. Starting from the zero mark on the ship's heading, four 90° clockwise rotations and four 90° counterclockwise rotations were performed. At each station, the APC assembly was held steady for 2 min to obtain a mean magnetic tool face value at each station. The ship's heading varied only ~3° during the orientation testing experiment. Both tools measured the relative rotations between stations accurately, but both showed an average error of ~150° from the expected value. After analyzing various factors, we concluded that this 150° error is unlikely to be entirely caused by a local distortion of the magnetic field around the rig floor. Rather, we suspect that the magnetic tool face recorded a true deviation of ~180° from the double lines on the core liner. Indications from subsequent expeditions show that the problem was caused when a shock absorber included in the orientation tool's sinker bar assembly periodically failed through shearing or twisting. This element has been removed from the redesigned orientation tool connector.

Figure F37. Relationship between IODP coordinate system, MTF of the orientation tool, and core liner.

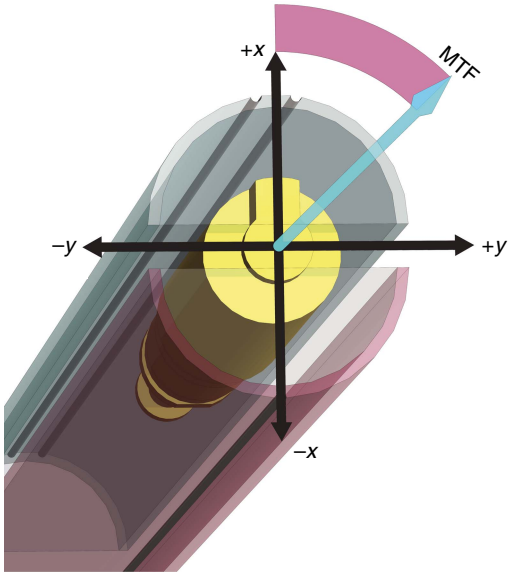

Figure F38. APC assembly used for orientation tool testing, where the working-half double lines were aligned with a pointer that was pointing to the ship's heading.

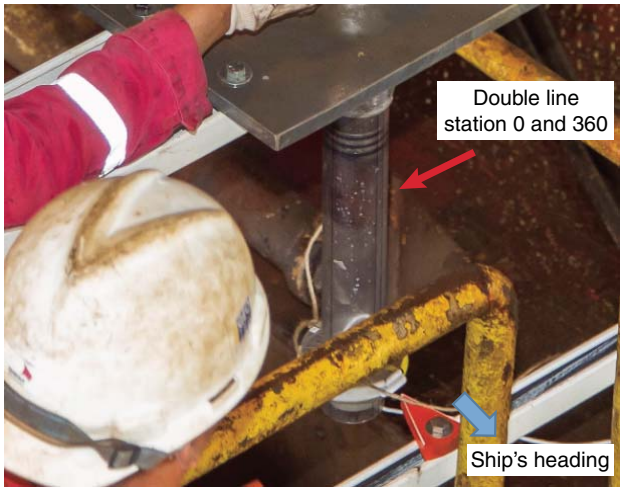

It thus became apparent that measured remanent declinations should be corrected to magnetic north by adding 180° to the magnetic tool face angle. Declinations can also be further corrected to true north by adding the deviation of magnetic north from true north (i.e., local declination, which can be determined from the International Geomagnetic Reference Field coefficients; see above and Richter et al. 2007). The information provided by this experiment contributed greatly to paleomagnetic polarity determinations and magnetostratigraphic interpretations of Expedition 362 cores.

ChRM also provides a reference frame to orient cores (see **Structural geology**). Provided that the reference magnetic pole is known, the orientation of the paleomagnetic vector is then used to restore the azimuth of the core: the horizontal component of the mean ChRM makes an angle with the reference line, which specifies the rotation of the core relative to the geographic coordinates (e.g., Fuller, 1969). The assumptions for orientation are

1. The section has enough measurements to average out geomagnetic secular variation;
2. The original bedding is horizontal;
3. The borehole is vertical; and
4. The sedimentary unit has not experienced any vertical axis rotation.

Assumptions 2 and 3 were confirmed with shipboard structural geologists, seismic profiles across the drill sites, and drilling operational records. Assumptions 1 and 4 will be checked postcruise. For intervals of particular interest for structural geology, we report the ChRMs defined from discrete samples. More detailed demagnetization steps for the discrete samples allowed more accurate ChRMs than those from the archive halves. In addition, well-defined VRM overprints from discrete samples could also be used in orienting observed structures in the core.

Magnetostratigraphy

A magnetostratigraphy was constructed at each site by correlating observed polarity sequences with the geomagnetic polarity timescale (GPTS) in combination with biostratigraphic biohorizons. The chosen GPTS for Expedition 362 is based on the combination of the following data sets (Table **T11**):

- Hilgen et al. (2012) from the top of Chron C1n at 0.00 Ma (Holocene) through the base of Chron C6Cn.2n at 23.03 Ma (base of the Miocene),
- Pälike et al. (2006) from the base of Chron C6Cn.2r at 23.27 Ma (Oligocene) through the base of Chron C19n at 41.41 Ma (middle Eocene),
- Vandenberghe et al. (2012) from the base of Chron C19r at 42.30 Ma (middle Eocene) through the base of Chron C29n at 65.69 Ma (early Paleocene), and
- Husson et al. (2011) from the top of Chron C30n at 66.30 Ma through the base of Chron C31r at 71.40 Ma (Maastrichtian); the Expedition 362 timescale ends at 70.65 Ma, within Chron C31r.

This composite GPTS, together with microfossil biozone summaries, are plotted in Figures **F30**, **F31**, **F32**, **F33**, and **F34**.

For azimuthally unoriented sedimentary samples that formed in low latitudes, such as those retrieved from the Expedition 362 drill sites, determining the polarity of sedimentary units can be difficult. The polarity ambiguity arises when the samples are azimuthally unoriented and the inclination is very shallow near the Equator (the angular distance between reversed and normal polarity inclinations is small). Because paleomagnetic inclinations from any samples will have some degree of dispersion about their mean inclination, it is likely that when the mean inclination is shallow (near zero), the sign of the inclination will not be indicative of the polarity (e.g., McFadden and Reid, 1982; Cox and Gordon, 1984). The sign of the inclination of these samples should be used with caution as a definitive estimate of magnetic polarity.

We applied the following methods to establish magnetozones:

1. Observing near-180° shifts in declinations and significant changes in inclinations (for the deeper section) from pass-through measurements on long coherent core sections after 15 mT demagnetization. The observed magnetozones are then checked with the ChRM directions of the discrete samples from the corresponding intervals as well as taking biostratigraphic age constraints into account.
2. Comparing inclination trends with predicted paleolatitudes of the drill sites according to the absolute plate motion of the Capricorn (Indian) plate following the latest, state-of-the art plate reconstructions (van Hinsbergen et al., 2015). Based on global plate circuit reconstructions, our drill sites have moved northward since the formation of this sediment. Following the reconstructed position of the drill holes for two representative periods at 20 and 40 Ma, the paleolatitudes would be ~5° and ~12° to the south of their present-day positions (3°N), respectively.
3. Using relative paleointensity as a proxy. In recent years, independent records of relative paleointensity (RPI) data from sediment cores in different oceans of the world have been stacked and correlated with magnetic polarity chrons, even down to millennial scale. Several global paleointensity stacks have been produced including GLOPIS (for the last 75 ky; Laj et al., 2004), Sint-800 (for the last 800 ky; Guyodo and Valet, 1999), Sint-2000 (for the last 2000 ky; Valet et al., 2005), and PISO-1500 (for the last 1.5 My, which also combines isotope records; Channell et al., 2009). Regional stacks for the last 75 ky have also been generalized for the North Atlantic (NAPIS; Laj et al., 2000), South Atlantic (SAPIS; Stoner et al., 2002), and western equatorial Pacific (EPAPIS, covering the 0.75–3.0 Ma interval; Yamazaki and Oda, 2005). The RPI stacks provide a stratigraphic template that can be potentially used to correlate the relative paleointensity records from Expedition 362 Indian Ocean sediment and hence help refine the magnetostratigraphy of the drill sites.

Whenever possible, we offer an interpretation of the magnetic polarity, with the naming convention following that of correlative anomaly numbers prefaced by the letter C (Tauxe et al., 1984). Normal polarity subchrons are referred to by adding suffixes (n1, n2) that increase with age. For the younger part of the timescale (Pliocene–Pleistocene), we use the traditional names to refer to the various chrons and subchrons (e.g., Brunhes, Jaramillo, Olduvai, etc.). In general, polarity reversals occurring at core section ends have been treated with extreme caution.

Data reduction and software

Data reduction (Zijderveld demagnetization plots and equal area projections) was conducted using PuffinPlot (Version 1.03, 23 April 2015) (Lurcock and Wilson, 2012), a versatile, user-friendly desktop application. PCA (Kirschvink, 1980) was also performed using PuffinPlot to determine ChRM directions.

Table T11. Data sets used to construct Expedition 362 geomagnetic polarity timescale (GPTS). (Continued on next page.) **Download table in .csv format.**

Polarity chron	Top age (Ma)	Base age (Ma)	Duration (My)	References and notes for boundary age estimates
C1n (Brunhes)	0	0.781	0.781	Start of Hilgen et al. (2012), table 29.3
C1n.1r (Matuyama)	0.781	0.988	0.207	
C1r.1n (Jaramillo)	0.988	1.072	0.084	
C1r.2r	1.072	1.173	0.101	
C1r.2n (Cobb Mountain)	1.173	1.185	0.012	
C1r.3r	1.185	1.778	0.593	
C2n (Olduvai)	1.778	1.945	0.167	
C2r.1r	1.945	2.128	0.183	
C2r.1n (Reunion)	2.128	2.148	0.02	
C2r.2r (Matuyama)	2.128	2.581	0.453	
C2An.1n (Gauss)	2.581	3.032	3.032	
Pliocene/Pleistocene boundary				2.59 Ma, ~2% below top of C2An.1n
C2An.1r (Keana)	3.032	3.116	0.084	
C2An.2n	3.116	3.207	0.091	
C2An.2r (Mammoth)	3.207	3.33	0.123	
C2An.3n (Gauss)	3.33	3.596	0.266	
C2Ar (Gilbert)	3.596	4.187	0.591	
C3n.1n (Cochiti)	4.187	4.3	0.113	
C3n.1r	4.3	4.493	0.193	
C3n.2n (Nunivak)	4.493	4.631	0.138	
C3n.2r	4.631	4.799	0.168	
C3n.3n (Sidufjall)	4.799	4.896	0.097	
C3n.3r	4.896	4.997	0.101	
C3n.4n (Thvera)	4.997	5.235	0.238	
C3r (Gilbert)	5.235	6.033	0.798	
Miocene/Pliocene boundary				5.33 Ma, ~12% below top of C3n.4r
C3An.1n	6.033	6.252	0.219	
C3An.1r	6.252	6.436	0.184	
C3An.2n	6.436	6.733	0.297	
C3Ar	6.733	7.14	0.407	
C3Bn	7.14	7.212	0.072	
C3Br.1r	7.212	7.251	0.039	
C3Br.1n	7.251	7.285	0.034	
C3Br.2r	7.285	7.454	0.169	
C3Br.2n	7.454	7.489	0.035	Base is from Lourens et al. (2004); no data in Hilgen et al. (2012)
C3Br.3r	7.489	7.528	0.039	
C4n.1n	7.528	7.642	0.114	Top is from Lourens et al. (2004); no data in Hilgen et al. (2012)
C4n.1r	7.642	7.695	0.053	
C4n.2n	7.695	8.108	0.413	
C4r.1r	8.108	8.254	0.146	
C4r.1n	8.254	8.3	0.046	
C4r.2r	8.3	8.771	0.471	
C4An	8.771	9.105	0.334	
C4Ar.1r	9.105	9.311	0.206	
C4Ar.1n	9.311	9.426	0.115	
C4Ar.2r	9.426	9.647	0.221	
C4Ar.2n	9.647	9.721	0.074	
C4Ar.3r	9.721	9.786	0.065	
C5n.1n	9.786	9.937	0.151	
C5n.1r	9.937	9.984	0.047	
C5n.2n	9.984	11.056	1.072	
C5r.1r	11.056	11.146	0.09	
C5r.1n	11.146	11.188	0.042	
C5r.2r	11.188	11.263	0.075	
C5r.2r-1n	11.263	11.308	0.045	
C5r.2r-1n.1r	11.308	11.592	0.284	
C5r.2n	11.592	11.657	0.065	
C5r.3r	11.657	12.049	0.392	
C5An.1n	12.049	12.174	0.125	
C5An.1r	12.174	12.272	0.098	
C5An.2n	12.272	12.474	0.202	
C5Ar.1r	12.474	12.735	0.261	
C5Ar.1n	12.735	12.77	0.035	
C5Ar.2r	12.77	12.829	0.059	
C5Ar.2n	12.829	12.887	0.058	
C5Ar.3r	12.887	13.032	0.145	
C5AAn	13.032	13.183	0.151	
C5AAr	13.183	13.363	0.18	
C5ABn	13.363	13.608	0.245	
C5ABr	13.608	13.739	0.131	
C5ACn	13.739	14.07	0.331	
C5ACr	14.07	14.163	0.093	
C5ADn	14.163	14.609	0.446	
C5ADr	14.609	14.775	0.166	
C5Bn.1n	14.775	14.87	0.095	
C5Bn.1r	14.87	15.032	0.162	
C5Bn.2n	15.032	15.16	0.128	
C5Br	15.16	15.974	0.814	
C5Cn.1n	15.974	16.268	0.294	
C5Cn.1r	16.268	16.303	0.035	
C5Cn.2n	16.303	16.472	0.169	
C5Cn.2r	16.472	16.543	0.071	
C5Cn.3n	16.543	16.721	0.178	
C5Cr	16.721	17.235	0.514	
C5Dn	17.235	17.533	0.298	
C5Dr.1r	17.533	17.717	0.184	
C5Dr.1n	17.717	17.74	0.023	
C5Dr.2r	17.74	18.056	0.316	
C5En	18.056	18.524	0.468	
C5Er	18.524	18.748	0.224	
C6n	18.748	19.722	0.974	
C6r	19.722	20.04	0.318	
C6An.1n	20.04	20.213	0.173	
C6An.1r	20.213	20.439	0.226	
C6An.2n	20.439	20.709	0.27	
C6Ar	20.709	21.083	0.374	
C6AAn	21.083	21.159	0.076	
C6AAr.1r	21.159	21.403	0.244	
C6AAr.1n	21.403	21.483	0.08	
C6AAr.2r	21.483	21.659	0.176	
C6AAr.2n	21.659	21.688	0.029	
C6AAr.3r	21.688	21.767	0.079	
C6Bn.1n	21.767	21.936	0.169	
C6Bn.1r	21.936	21.992	0.056	
C6Bn.2n	21.992	22.268	0.276	
C6Br	22.268	22.564	0.296	
C6Cn.1n	22.564	22.754	0.19	
C6Cn.1r	22.754	22.902	0.148	
C6Cn.2n	22.902	23.03	0.128	Base: end of Hilgen et al. (2012), table 29.3
Oligocene/Miocene boundary				23.03 Ma, C6Cn.2n/C6Cn.2r boundary
C6Cn.2r	23.03	23.278	0.248	Base: start of Pälike et al. (2006), Web table S 1 (auto); timescale switch makes C6Cn.2r shorter (4 ky)
C6Cn.3n	23.278	23.34	0.062	
C6Cr	23.34	24.022	0.682	
C7n.1n	24.022	24.062	0.04	
C7n.1r	24.062	24.147	0.085	
C7n.2n	24.147	24.459	0.312	
C7r	24.459	24.756	0.297	
C7An	24.756	24.984	0.228	
C7Ar	24.984	25.11	0.126	
C8n.1n	25.11	25.248	0.138	
C8n.1r	25.248	25.306	0.058	
C8n.2n	25.306	26.032	0.726	
C8r	26.032	26.508	0.476	

Table T11 (continued).

Polarity chron	Top age (Ma)	Base age (Ma)	Duration (My)	References and notes for boundary age estimates
C9n	26.508	27.412	0.904	
C9r	27.412	27.886	0.474	
C10n.1n	27.886	28.126	0.24	
C10n.1r	28.126	28.164	0.038	
C10n.2n	28.164	28.318	0.154	
C10r	28.318	29.166	0.848	
C11n.1n	29.166	29.467	0.301	
C11n.1r	29.467	29.536	0.069	
C11n.2n	29.536	29.957	0.421	
C11r	29.957	30.617	0.66	
C12n	30.617	31.021	0.404	
C12r	31.021	33.232	2.211	
C13n	33.232	33.705	0.473	
C13r	33.705	35.126	1.421	
Eocene/Oligocene boundary				33.90 Ma, ~14% below top of C13r
C15n	35.126	35.254	0.128	
C15r	35.254	35.328	0.074	
C16n.1n	35.328	35.554	0.226	
C16n.1r	35.554	35.643	0.089	
C16n.2n	35.643	36.355	0.712	
C16r	36.355	36.668	0.313	
C17n.1n	36.668	37.52	0.852	
C17n.1r	37.52	37.656	0.136	
C17n.2n	37.656	37.907	0.251	
C17n.2r	37.907	37.956	0.049	
C17n.3n	37.956	38.159	0.203	
C17r	38.159	38.449	0.29	
C18n.1n	38.449	39.554	1.105	
C18n.1r	39.554	39.602	0.048	
C18n.2n	39.602	40.084	0.482	Base: end of Pälike et al. (2006), Web table S 1 (auto)
C18r	40.084	41.358	1.274	Base: start of Vandenberghe et al. (2012), table 28.3
C19n	41.358	41.51	0.152	
C19r	41.51	42.3	0.79	Timescale switch makes C19r shorter (~120 ky)
C20n	42.3	43.43	1.13	
C20r	43.43	45.72	2.29	
C21n	45.72	47.35	1.63	
C21r	47.35	48.57	1.22	
C22n	48.57	49.34	0.77	
C22r	49.34	50.63	1.29	
C23n.1n	50.63	50.83	0.2	
C23n.1r	50.83	50.96	0.13	
C23n.2n	50.96	51.83	0.87	
C23r	51.83	52.62	0.79	
C24n.1n	52.62	53.07	0.45	
C24n.1r	53.07	53.2	0.13	
C24n.2n	53.2	53.27	0.07	
C24n.2r	53.27	53.42	0.15	
C24n.3n	53.42	53.98	0.56	
C24r	53.98	57.1	3.12	
Paleocene/ Eocene boundary				56.0 Ma, ~64% below top of C24r
C25n	57.1	57.66	0.56	
C25r	57.66	58.96	1.3	
C26n	58.96	59.24	0.28	
C26r	59.24	62.22	2.98	
C27n	62.22	62.52	0.3	
C27r	62.52	63.49	0.97	
C28n	63.49	64.67	1.18	
C28r	64.67	64.96	0.29	
C29n	64.96	65.69	0.73	Base: end of Vandenberghe et al. (2012), table 28.3
C29r	65.69	66.3	0.61	Base: start of Husson et al. (2011), table 1, option 2
Late Cretaceous/Paleocene boundary				66.0 Ma, ~50% below top of C29r
C30n	66.3	68.2	1.9	Top: start of Husson et al. (2011), table 1, option 2
C30r	68.2	68.32	0.12	
C31n	68.32	69.22	0.9	
C31r	69.22	71.4	2.18	Expedition 362 GPTS ends at 70.65 Ma, within C31r

Geochemistry

Expedition 362 was designed to establish initial and evolving properties of the incoming section to the North Sumatran subduction zone and their role in shallow seismogenesis and forearc plateau development. The thick input section has likely undergone substantial diagenetic alterations below the trench wedge and just in front of the subduction zone, which may alter mechanical properties of the wedge and so may influence shallow seismogenic slip. Fluids and associated diagenetic reactions, both at the drill sites and reactions expected from the sediment mineralogy and pore fluid chemistry, are thus a key component of this study. The concentration of dissolved species and their isotopic composition provide critical data for identification of fluid–rock reactions, assessment of potential fluid flow through the underlying oceanic crust, and identification of any potential migration pathways and fluid sources within the sediment section. In addition, geochemical data can help characterize biogeochemical cycling, guide paleoceanographic reconstructions, and aid in constraining mass balance inventories operating in this subduction zone.

Interstitial water sampling protocol

During Expedition 362, most of the interstitial water samples were collected from whole-round samples; in addition, fluids were collected using Rhizon samplers inserted into the uncut liner of Cores 362-U1480H-9H, 10H, and 11H. Interstitial water whole-round samples were collected at a frequency of 3–7 samples per core in the first 4 or 5 cores and subsequently at a resolution of 1 or 2 samples per core to the bottom of the hole. The length of the whole rounds used was 10 cm in the shallow cores and increased with depth, depending on interstitial water recovery, to a maximum of 25 cm. Rhizon samples were collected at a resolution of 2 samples per section and yielded pore water volumes from 0 to 12 mL. Details of sampling protocols for each site are given in the corresponding site chapters.

For headspace analyses of gas concentrations, 1 or 2 sediment plugs were routinely collected; one was used for standard hydrocarbon concentration monitoring on board and the other for stable-isotope measurements at onshore laboratories. The headspace samples were collected adjacent to each interstitial water sample when

one was taken. For safety monitoring, purposed headspace samples were also taken from cores with not enough recovery for interstitial water sampling.

Interstitial water collection

Whole-round cores were cut on the catwalk, capped, and taken to the laboratory for processing. In general, samples collected from the seafloor to ~130 mbsf were processed inside a nitrogen bag to avoid oxidation of redox-sensitive elements. All other cores were processed under normal atmospheric conditions. During high-resolution sampling, when there were too many interstitial water cores to process immediately, capped whole-round core sections were stored under a nitrogen atmosphere at 4°C until they were squeezed, which occurred no later than 24 h after core retrieval.

After extrusion from the core liner, the surface of each whole-round interstitial water sample was carefully scraped with a spatula to remove potential contamination from seawater and sediment smearing in the borehole. For APC and most RCB cores, removal of ~0.5 cm of material from the outer diameter, top, and bottom faces was sufficient, whereas in XCB and some RCB cores where borehole contamination seemed higher, as much as two-thirds of the sediment was removed from each whole round. The remaining sediment (~150–300 cm^3) was placed into a titanium squeezer modified after the stainless-steel squeezer of Manheim and Sayles (1974). Samples were squeezed at maximum pressures of 24.5 MPa (gauge forces of up to 35,000 lb). The squeezed interstitial water was filtered through a prewashed Whatman No. 1 filter placed in the squeezers above a titanium screen. The squeezed interstitial water was collected in precleaned, plastic syringes attached to the squeezing assembly and subsequently filtered through a 0.45 µm Gelman polysulfone disposable filter. In the deeper sections of the sites, fluid recovery was as low as 1 mL after squeezing the sediment for up to ~24 h.

Sample allocation was determined based on the recovered interstitial water volume and analytical priorities based on the objectives of the expedition. The shipboard analytical protocols are summarized in the following section.

Shipboard interstitial water analyses

Interstitial water samples were analyzed on board following protocols in Gieskes et al. (1991), Murray et al. (2000), and the IODP user manuals (**http://iodp.tamu.edu/labs/documentation/**).

Salinity, alkalinity, and pH

Salinity, alkalinity, and pH were measured immediately after squeezing. Salinity was measured using a Fisher temperature-compensated handheld refractometer, pH was measured with a combination glass electrode, and alkalinity was determined by Gran titration with an autotitrator (Metrohm 794 basic Titrino) using 0.1 M HCl at 20°C. Certified reference material (CRM) 104 obtained from the laboratory of Andrew Dickson, Marine Physical Laboratory, Scripps Institution of Oceanography (USA), was used for calibration of the acid. International Association for the Physical Sciences of the Oceans (IAPSO) standard seawater was analyzed at the beginning and end of a set of samples for each site and after approximately every 10 samples.

Chloride, sulfate, and bromide

High-precision chloride concentrations were acquired using a Metrohm 785 DMP autotitrator and silver nitrate ($AgNO_3$) solutions that were calibrated against repeated titrations of an IAPSO standard. A 0.1 mL aliquot of sample was diluted with 10 mL of 90 ± 2 mM HNO_3 and titrated with 0. 014 M $AgNO_3$. Repeated analyses of an IAPSO standard yielded a precision better than 0.35%.

In samples from Holes U1480E and U1480F, concentrations of sulfate (SO_4^{2-}), chloride (Cl^-), and bromide (Br^-) were analyzed using 100 µL aliquots diluted 1:100 with deionized water (18 MΩ). Subsequent samples were diluted 1:100 using a 50 µM KNO_3 solution used as an internal standard. In all cases, we used an ion chromatograph (IC; Metrohm 850 Professional) and eluent solutions of 3.2 mM Na_2CO_3 and 1.0 mM $NaHCO_3$. Concentrations were based on peak areas. The analytical protocol used was to run a standard after 5 samples for 6 cycles, after which 3 extra standards were analyzed. The standards used were based on IAPSO dilutions of 50×, 80×, 150×, 250×, 500×, 750×, 1000×, 1200×, 1500×, and 2000×. Sample replicates (N = 5) were analyzed during each run for reproducibility. Reproducibility was also checked based on the interspersed standard samples run throughout the expedition. Analytical precision was 2% for sulfate, chloride, and bromide when no internal standard was used but yielded precision better than 1% when using KNO_3 as an internal standard. Chloride analyses by both titration and IC agree within 2%; for this expedition we report both values but plot only the titration data.

Ammonium, phosphate, and silica

Ammonium, phosphate, and silica concentrations were determined by spectrophotometry using an Agilent Technologies Cary Series 100 UV-Vis spectrophotometer with a sipper sample introduction system following the protocol in Gieskes et al. (1991). Phosphate was measured using the ammonium molybdate method described in Gieskes et al. (1991), using appropriate dilutions. Orthophosphate reacts with Mo(VI) and Sb(III) in an acidic solution to form an antimony-phosphomolybdate complex. Ascorbic acid reduces this complex to form a blue color, and absorbance is measured spectrophotometrically at 885 nm.

The ammonium method is based on diazotization of phenol and subsequent oxidation of the diazo compound by household bleach (sodium hypochlorite) to yield a blue color measured spectrophotometrically at 640 nm. Samples were diluted prior to color development so that the highest concentration was <1000 µM.

Silica was also measured spectrophotometrically using the method based on the production of a yellow silicomolybdate complex. The complex is reduced by ascorbic acid to form molybdenum blue, measured at 812 nm.

Major elements

In past expeditions, major elements (Ca, Mg, K, and Na) were commonly analyzed by inductively coupled plasma–atomic emission spectroscopy (ICP-AES) with a Teledyne Prodigy high-dispersion ICP spectrometer. Samples and standards were diluted 1:100 using 2% HNO_3 spiked with 10 ppm Y as an internal standard. However, because the new IC instrument yields cation concentration data during the standard IC run for anions (sulfate, bromide, and chloride), we compared both analytical approaches by repeated analyses of standards and samples (archived data from IODP Expedition 344 Site U1414 and a dedicated run for samples from Site U1480). The data generated by both approaches agreed to better than 1.5%; therefore, we used the IC data to report major cation concentrations measured during Expedition 362.

IC analyses were conducted using the same aliquot dilutions as the ones used for anions: 1:100 using a 50 µM KNO_3 solution as an internal standard. The eluent solutions used for cation measurements were 3.2 mM Na_2CO_3 and 1.7 mM PDCA (pyridine-2,6-

dicarboxylic acid) supplied by Metrohm (CAS#499-83-2). Concentrations were based on peak areas and corrected against the average area of the KNO_3 internal standard. Analogous to the protocol used for anion measurements, the analytical protocol for cations was to run a standard after 5 samples for 6 cycles, after which 3 extra standards were analyzed. The standards used were based on IAPSO dilutions of 50×, 80×, 150×, 250×, 500×, 750×, 1000×, 1200×, 1500×, and 2000×. Sample replicates (N = 5) were analyzed during each run for reproducibility. Reproducibility was also checked based on the interspersed standard samples run throughout the expedition. Analytical precision was 0.3% for Na and K, 0.6% for Mg, and 1.0% for Ca.

Minor elements

Minor elements (Fe, Li, Ba, B, and Mn) were analyzed by ICP-AES with a Teledyne Prodigy high-dispersion ICP spectrometer. The general method for shipboard ICP-AES analysis of samples is described in Murray et al. (2000) and user manuals for shipboard instrumentation. Each batch of samples run on the ICP spectrometer contains blanks and solutions of known concentrations. Each item aspirated into the ICP spectrometer was counted 4 times from the same dilute solution within a given sample run. Following each instrument run, the measured raw-intensity values were transferred to a data file and corrected for instrument drift and blank. If necessary, a drift correction was applied to each element by linear interpolation between the drift-monitoring solutions.

For the minor element concentration analyses, an interstitial water sample aliquot was diluted by a factor of 20 (0.5 mL sample added to 9.5 mL of a 10 ppm Y solution). Because of the high concentration of matrix salts in the interstitial water samples at a 1:20 dilution, matrix-matching of the calibration standards is necessary to achieve accurate results by ICP-AES. A matrix solution that approximated IAPSO standard seawater major ion concentrations was prepared according to Murray et al. (2000). A stock standard solution was prepared from ultrapure primary standards (SPC Science PlasmaCAL) in a 2% nitric acid solution. The stock solution was then diluted in the same 2% ultrapure nitric acid solution to concentrations of 100%, 75%, 50%, 25%, 10%, 5%, and 1%. In addition to this set of standards, we include dilutions of IAPSO standard to constrain the lower-end range of concentrations measured in interstitial water during Expedition 362. The calibration standards and IAPSO solutions were diluted using the same method as the samples for consistency. The final matrix-matched 100% standard solution contained the following concentrations of elements: B = 1388.9 µM, Li = 288.2 µM, Mn = 54.6 µM, Fe = 17.9 µM, Sr = 228.1 µM, and Ba = 36.4 µM. The 100%, 75%, 50%, 25%, 10%, and 5% standards were repeatedly analyzed for each batch and over the 2-month expedition as a check of analytical precision. The average precision of the minor element analyses were B < 1%, Ba < 1%, Mn < 1%, Li < 1.5%, Si < 1.5%, and Sr <1%.

Fluid organic geochemistry

Routine analysis of hydrocarbon gas in sediment cores is a part of the standard IODP shipboard monitoring of the cores to ensure that the sediments being drilled do not contain greater than the expected amount of hydrocarbons. The most common method of hydrocarbon monitoring used during IODP expeditions is the analysis of gas samples obtained from either sediment samples (headspace analysis) or from gas expansion pockets visible through clear plastic core liners (void gas analysis) following the procedures described by Kvenvolden and McDonald (1986).

When gas pockets were detected, the free gas was drawn from the sediment void using a syringe attached to a hollow stainless-steel tool used to puncture the core liner. The gas then was analyzed on the natural gas analyzer (NGA). For headspace analyses, a 3 cm^3 bulk sediment sample was collected from the freshly exposed top end of a core section and next to the interstitial water sample immediately after core retrieval using a brass boring tool or plastic syringe. The sediment plug was sealed with an aluminum crimp cap with Teflon/silicon septa. The vial was then heated to 70°C for ~30 min to evolve hydrocarbon gases from the sediment plug. When consolidated or lithified samples were encountered, chips of material were placed in the vial and sealed. For gas chromatographic analysis, a 5 cm^3 volume of headspace gas was extracted from the sealed sample vial using a standard gas syringe and analyzed by gas chromatography.

The standard gas analysis program for safety was complemented by collecting an additional headspace sample at the same resolution as described above to measure the stable carbon and hydrogen isotope composition of hydrocarbons at onshore laboratories. The sampling method is the same as that used for the safety analysis, except that the sediment plug is extruded into a 20 cm^3 headspace glass vial filled with 10 cm^3 of a 1 M potassium chloride (KCl) solution containing borosilicate glass beads and immediately sealed with an aluminum crimp cap with Teflon/silicon septa. The vial was then vigorously shaken to help dissociate the sediment. Potassium chloride is toxic and was thus used to stop all microbial activity in the sediment. The glass beads (3 mm diameter) were used to help break up the sediment plug during shaking and liberate gas trapped in sediment pore space or adsorbed on particles. The vials were flushed with N_2 and capped within 1 h prior to sampling in order to remove air from the headspace and ensure the sample is preserved anaerobically.

Headspace and void gas samples were directly injected into the gas chromatograph–flame ionization detector (GC-FID) or into the NGA. The headspace samples were analyzed using an Agilent/HP 6890 Series II gas chromatograph (GC3) equipped with an 8 ft, 2.00 mm inner diameter × ⅛ inch outer diameter stainless steel column packed with 80/100 mesh HayeSep R and an FID set at 250°C. The GC3 oven was programmed to hold temperature at 80°C for 8.25 min, ramp at 40°C/min to 150°C, hold for 5 min, and return to 100°C postrun for a total of 15 min. Helium was used as the carrier gas. The GC3 system determines concentrations of methane (C_1), ethane (C_2), ethene ($C_{2=}$), propane (C_3), and propene ($C_{3=}$).

Data were collected using the Hewlett Packard 3365 Chemstation data processing program. Chromatographic response is calibrated to nine different gas standards with variable quantities of low molecular weight hydrocarbons. The gas concentrations for the required safety analyses are expressed as component parts per million by volume (ppmv) relative to the analyzed gas.

Sediment geochemistry

For the shipboard sediment geochemistry analyses, 5 cm^3 of sediment was freeze-dried for ~24 h, crushed to a fine powder using a pestle and agate mortar, and subsampled to analyze inorganic carbon, total carbon (TC), and total nitrogen (TN).

Elemental analysis

TC and TN of sediment samples were determined with a ThermoElectron Corporation FlashEA 1112 CHNS elemental analyzer equipped with a ThermoElectron CHNS/NCS packed column and a thermal conductivity detector (TCD). Approximately 10–15 mg of

freeze-dried, ground sediment was weighed in a tin cup and the sample was combusted at 900°C in a stream of oxygen. The reaction gases were passed through a reduction chamber to reduce nitrogen oxides to nitrogen and were then separated by gas chromatography before detection by TCD. All measurements were calibrated to a standard soil reference material (soil Standard 33840025) for carbon and nitrogen detection (Thermo), which was run every 6 samples as a verification. The detection limit was 0.001% for TN (instrument limit) and 0.002% for TC (procedural blank; measured as an empty tin cup). Sample replicates (N = 10 for each of 5 samples) yielded precisions of <10% for TN and <7% for TC.

Inorganic and organic carbon content

Total inorganic carbon (TIC) concentrations were determined using a UIC 5011 CO_2 coulometer. Between 10 and 15 mg of freeze-dried, ground sediment was weighed and reacted with 2 M HCl. The liberated CO_2 was titrated and the end-point was determined by a photodetector. Calcium carbonate content expressed as weight percent was calculated from the TIC content assuming that all evolved CO_2 was derived from dissolution of $CaCO_3$, using the following equation:

$$CaCO_3\ (wt\%) = TIC \times 8.33\ (wt\%).$$

No correction was made for the presence of other carbonate minerals. Accuracy during individual batches of analyses was determined by running a carbonate standard (100 wt% $CaCO_3$) every 10 samples. Typical precision, assessed using replicate analyses of a carbonate sample (N = 10 for each of 5 samples), was 2%. The detection limit for $CaCO_3$, defined here as 3 times the standard deviation of the blank (2 M HCl), was 0.1% for 100 mg of pelagic clay. Total organic carbon (TOC) content was calculated as the difference between TC (measured on the elemental analyzer) and inorganic carbon (measured by coulometry):

$$TOC = TC - IC.$$

Physical properties

Core material was characterized by multiple physical property measurements. For soft sediment, the general sample work flow was as follows:

1. Cores were thermally equilibrated to ambient room temperature (20°C) over a period of 1–3 h.
2. Whole-round cores were run on the WRMSL. The WRMSL includes a GRA bulk densitometer, a magnetic susceptibility pass-through loop system (MSL), and a PWL.
3. Whole-round cores were run on the NGRL when the length of an individual section was >50 cm.
4. Thermal conductivity (TCON) was measured on 1 section (typically Section 3) of each core.
5. Cores were split.
6. The archive half of the core was passed through the SHIL for imaging and SHMSL for RSC and MSP.
7. Shipboard samples for MAD analyses were collected (generally 2 per section and adjacent to all whole-round samples). Samples were taken in representative lithologies. In case of delayed sampling, the samples were resaturated.
8. Discrete compressional velocity measurements were made on the working half cores using the *P*-wave velocity gantry.
9. Strength measurements (for soft sediment only) were made on the working half using the Automated Vane Shear and/or a pocket penetrometer.

For hard rock cores, a slightly different sequence was used:

1. Cores were thermally equilibrated to ambient room temperature for at least 2 h.
2. Whole-round cores were run on the WRMSL with the PWL turned off.
3. Whole-round cores were run on the NGRL when the length of an individual section was >50 cm.
4. Cores were split.
5. The archive half of the core was passed through the SHIL for imaging and SHMSL for RSC and MSP.
6. Oriented, discrete cube samples (~2 cm^3) were taken from the working half for *P*-wave velocity and MAD measurements. When taken more than ~12 h after the arrival of the core on deck, the samples were placed in seawater under vacuum for 24 h for resaturation before measurement. The samples were measured for *P*-wave velocity in three orthogonal directions and then processed for MAD measurements. *P*-wave measurements were also made on PMAG samples (but without resaturation).
7. Selected pieces of the core sections >7 cm were measured for thermal conductivity.

All raw data were uploaded to the LIMS database.

Whole-Round Multisensor Logger measurements

The WRMSL was used to measure GRA density, magnetic susceptibility, and *P*-wave velocity nondestructively. The sampling interval for WRMSL measurements was set at 2.5 cm.

GRA bulk density

The GRA densitometer on the WRMSL operates by passing gamma rays from a ^{137}Cs source through a whole-round core and into a 75 mm^3 sodium iodide (NaI) detector located directly below the core. The input gamma ray peak has a principal energy of 0.662 MeV that is attenuated as it passes through the core. Attenuation of gamma rays, mainly by Compton scattering, is related to electron density, which is related to material bulk density by

$$\rho_b = \rho_e w/2\Sigma N,$$

where

ρ_b = bulk density,
ρ_e = electron density,
w = molecular weight, and
N = atomic number of elements in the material.

For the majority of elements and for rock-forming minerals, $w/2\Sigma N$ is ~1; although, $w/2\Sigma N$ for hydrogen is 0.5040. Therefore, for a known sample thickness the gamma ray count is proportional to density. Calibration of the GRA densitometer was performed using a core liner filled with freshwater and aluminum density standards at the beginning of the expedition. Calibration was verified after each core measurement by passing the freshwater-filled core liner through the densitometer. Recalibration was performed if the measured density of the freshwater standard exceeded limits of 1.00 ± 0.02 g/cm^3.

Magnetic susceptibility

Magnetic susceptibility, *K*, is a dimensionless measure of the degree to which a material can be magnetized by an external magnetic field:

$$K = M/H,$$

where *M* is the magnetization induced in the material and *H* is the strength of an external field. Magnetic susceptibility varies in response to the type and concentration of magnetic grains and responds to variations in the magnetic composition of the sediment, both commonly related to variations in mineralogical composition (e.g. terrigenous versus biogenic materials) and diagenetic overprinting. Materials such as clay generally have a magnetic susceptibility several orders of magnitude lower than magnetite and some other iron oxides that are common constituents of igneous and volcanogenic material. Water and plastics (such as the core liner) have a slightly negative magnetic susceptibility.

The WRMSL measures volume magnetic susceptibility using a Bartington Instruments MS2 meter (Bartington instruments, 2011) coupled to an MS2C sensor coil (88 mm diameter). An oscillator circuit in the sensor operates at an alternating field of ~100 mT and frequency of 565 Hz, producing a low-intensity nonsaturating magnetic field. During Expedition 362, the instrument was set to record instrumental units with an integration period of ~1 s, which produced a sensitivity of 1×10^{-5} SI units. No correction was applied for volume effects caused by differing APC, XCB, and RCB core diameters. The spatial resolution of the method is ±4 cm; therefore, core material that is not continuous over an 8 cm interval will underestimate the magnetic susceptibility.

P-wave velocity

P-wave velocity is the rate at which a (compressional) *P*-wave travels through a medium. *P*-wave velocity is dependent on the composition, bulk density, stiffness, fabric, and temperature of the material, which in turn are functions of consolidation and lithification, state of stress, and degree of fracturing. The PWL system on the WRMSL transmits 500 kHz *P*-wave pulses across the core liner and core with a 200 Hz repetition frequency. The pulser and receiver are mounted on a caliper-type device and are aligned in order to make wave propagation perpendicular to the section's long axis. A linear variable differential transducer (LVDT) measures the *P*-wave travel distance between the pulse source and the receiver. Good coupling between transducers and core liner is facilitated with water dripping onto the contact from a peristaltic water pump system. Signal processing software picks the first arrival of the wave at the receiver. Measured travel distance and time are corrected for twice the liner thickness.

A series of acrylic cylinders of varying thicknesses are used to calibrate the PWL system. The regression of traveltime versus travel distance yields the *P*-wave velocity of the standard material, which should be 2750 ± 20 m/s. The calibration is verified by measuring a core liner filled with pure water, and the calibration passes if the velocity is within ± 20 m/s of the expected value for pure water (1480 m/s at 20°C). The calibration of the PWL system was conducted after hardware maintenance, at each drill bit change (APC/XCB to RCB), and at each new hole during the expedition.

Natural Gamma Radiation Logger measurements

The NGRL measures the NGR emitted from whole-round core sections arising primarily from the radioactive decay of ^{238}U, ^{232}Th, and ^{40}K isotopes. The main NGRL detector unit consists of 8 sodium iodide (NaI) scintillator detectors, 7 plastic scintillator detectors, 22 photomultipliers, and passive lead shielding (8 cm). In addition, lead separators (~7 cm of low-background lead) are positioned between the NaI detectors. Half of the lead shielding closest to the NaI detectors is composed of low-background lead, and the outer half is composed of regular (virgin) lead. In addition to passive lead shielding, the NGRL employs a plastic scintillator to suppress the high-energy gamma and muon components of cosmic radiation by producing a canceling signal when these charged particles pass through the plastic scintillators. The NGRL was calibrated using a source consisting of ^{137}Cs and ^{60}Co and identifying the peaks at 662 keV (^{137}Cs) and 1330 keV (^{60}Co). The NGRL installed on the *JOIDES Resolution* was designed and built by IODP-USIO at Texas A&M University (Vasiliev et al., 2011). Calibration materials are provided by Eckert & Ziegler Isotope Products, Valencia, California (USA).

For presentation purposes, the counts were summed over a range from 100 to 3000 keV. Background measurements of an empty core liner counted for 12 h were made before each site. Over the 100–3000 keV integration range, background counts averaged 4–5 count/s.

A measurement run consists of 8 measurements made simultaneously at 20 cm intervals for the section of core, normally 150 cm long, repeated with an offset of 10 cm to give a total of 16 measurements at 10 cm intervals for the section. The core was wiped dry prior to NGR measurement. The quality of the energy spectrum measured in a core depends on the concentration of radionuclides in the sample but also on the counting time, with higher times yielding better spectra. The count time in each position was 5 min.

Section Half Image Logger measurements

The SHIL scans the surface of archive-half cores and creates a digital image. The line-scan camera contains three charge-coupled devices; each charge-coupled device has 1024 arrays. Light reflection from the sample surface passes through the lens and is split into three paths (red, green, and blue) by a beam splitter inside the line-scan camera. Then, each reflection is detected by the corresponding charge-coupled device. Finally, the signals are combined and a digital image is produced. Optical distortion is avoided by precise movement of the camera. Spatial resolution is 100 pixels/cm.

Section Half Multisensor Logger measurements

The SHMSL measures magnetic susceptibility and spectral reflectance on archive-half core sections. The archive half of the split core is placed on the system's core track. An electronic platform moves along a track above the core section, recording the sample height with a laser sensor. The laser establishes the location of the bottom of the section, and the platform reverses the direction of movement, moving from bottom to top, making measurements of point magnetic susceptibility and spectral reflectance data at 2.5 cm intervals.

Reflectance spectrophotometry and colorimetry

Reflectance of visible light from the archive halves of sediment cores was measured using an Ocean Optics USB4000 spectrophotometer mounted on the SHMSL. For sediment and sedimentary rock, freshly split cores were covered with clear plastic wrap. Spectral data are reduced to the L*a*b* colorspace for output and presentation. L* is lightness ranging between 0 (black) and 100 (white), a* is the red–green value ranging between –60 (green) and 60 (red), and b* is the yellow–blue value ranging between –60 (blue) and 60

(yellow). The color reflectance spectrophotometer calibrates on two spectra, pure white (reference) and pure black (dark). Measurements were recorded every 2.5 cm in wide spectral bands from 380 to 900 nm in 2 nm steps. Each measurement took ~5 s.

Point magnetic susceptibility

Point magnetic susceptibility was measured on the SHMSL using a Bartington MS2K point sensor (high-resolution surface-scanning sensor) operating at an alternating field of 100 mT and a frequency of 930 Hz, similar to the Bartington sensor MSL on the WRMSL. The sensor takes and averages 3 measurements at 1 s intervals to an accuracy of 5%. Measurements were made on the archive halves of split cores covered with clear plastic wrap. Measurements were taken at 2.5 cm spacing, integrating over a volume of 10.5 mm × 3.8 mm × 4 mm, where 10.5 mm is the length perpendicular to the core axis, 3.8 mm is the width along the core axis, and 4 mm is the depth. The probe was zeroed in air before each measurement point, and a background magnetic field was measured and removed from the data before being output.

P-wave velocity measurements

Discrete compressional wave (*P*-wave) velocity measurements were obtained on soft-sediment cores at a typical frequency of one per section, where conditions allowed, using the *P*-wave velocity gantry. *X*-axis measurements (Figure **F35**) were acquired with a caliper-type contact probe with one transducer contact on the face of the working half of the core and the other contact against the core liner. To maximize contact with the transducers, deionized water was applied to the sample and transducer surfaces. Measurements along the *y*- and *z*-axes were acquired using two pairs of bayonet probes inserted perpendicular and parallel to the axis of the working half, respectively. The system uses Panametrics-NDT Microscan delay line transducers, which transmit at 500 kHz.

For consolidated samples, the caliper-type contact probe was used to measure the *P*-wave velocity on discrete sample cubes (2 cm × 2 cm × 2 cm or 2 cm × 1 cm × 1 cm) at a typical frequency of 1 per section. The cubes were oriented following standard IODP conventions and then placed on the gantry caliper probe and rotated so that *P*-wave velocity was measured across all three axes (*x*-, *y*-, and *z*-directions; Figure **F35**). Next, these sample cubes were used for MAD measurements. Samples taken >12 h after arrival of the core on the deck, lithified samples, and igneous samples were resaturated in seawater under vacuum for at least 24 h before measurement. The stability of the vacuum was monitored by checking the pressure gauge every 5 h. Additional *P*-wave velocity measurements were conducted on oriented paleomagnetism samples when the PWL of the WRMSL was turned off. These samples were not resaturated prior to measurement.

The initial *P*-wave arrival was identified as the first significant positive amplitude peak (Figure **F39**) by manual picking. This peak is a feature that can be consistently picked even when the signal quality is low. Additionally, a built-in algorithm picked the arrival as the first zero crossing for waveforms with a high signal-to-noise ratio. Both the manual and autopicked arrivals and the complete waveforms are stored in the database in case reanalysis is deemed necessary.

The distance between transducers was measured with a built-in LVDT. Calibration was performed between each site with a series of acrylic cylinders of differing thicknesses and known *P*-wave velocity of 2750 ± 20 m/s for the caliper-type contact probe. Water was used to calibrate the bayonet probes. The system time delay determined

Figure F39. A–C. Examples of good waveforms acquired in Section 362-U1480F-5H-2. Black arrows indicate locations that were picked manually as the *P*-wave arrival on each waveform.

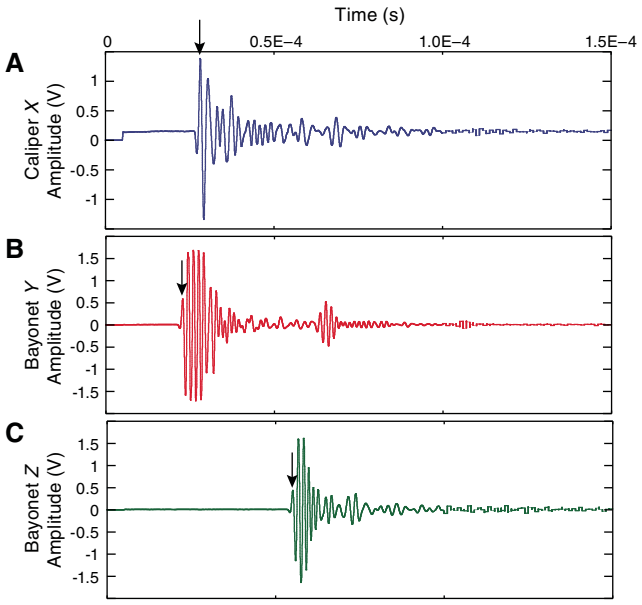

from calibration was subtracted from the picked arrival time to yield a traveltime of the *P*-wave through the sample. The thickness of the sample (from the LVDT) was divided by the traveltime to calculate a *P*-wave velocity.

For noisy waveforms, the automatic picker either generated an unrealistic velocity or did not pick. Comparison of the manual and automatic picks yielded conversions that can be used to shift the manual picks to the zero-crossing location of the autopicks. The conversion for the caliper (*x*-direction and discrete samples [*x*, *y*, and *z*]) is

$$V_{\text{corrected}} = 1.1451 V_{\text{manual}} - 180.52;$$

the conversion for the *y*-bayonet is

$$V_{\text{corrected}} = 1.3131 V_{\text{manual}} - 362.04, \text{ and}$$

the conversion for the *z*-bayonet is

$$V_{\text{corrected}} = 1.0968 V_{\text{manual}} - 104.78,$$

where V_{manual} is the velocity calculated from the manual pick and $V_{\text{corrected}}$ is the shifted velocity, both expressed in meters per second. The average difference between the shifted velocity and the automatic pick is <1.2%.

From these measurements, the *P*-wave anisotropy between the average horizontal and vertical velocities ($\text{Anis}_{(xy)z}$) and horizontal velocities (Anis_{xy}) was calculated as

$$\text{Anis}_{(xy)z} = [\text{mean}(V_x, V_y) - V_z]/\text{mean}(V_x, V_y, V_z) \text{ and}$$

$$\text{Anis}_{xy} = (V_x - V_y)/\text{mean}(V_x, V_y),$$

where V_x and V_y are the transverse core velocities and V_z is the longitudinal core velocity.

MAD measurements

MAD measurements on discrete samples provide several basic physical properties that can be used for characterizing lithostratigraphic units and for correlating cored material with logging data. Most commonly used MAD properties are moisture content, bulk density, porosity, and void ratio. These properties are calculated based on measured wet mass, dry mass, and dry volume. As with most other expeditions, we used Method C (Blum, 1997) as described below.

Sampling procedure

Generally two samples of ~10 cm^3 volume were taken on each sediment core section working half and adjacent to each whole-round sample. The samples were taken using a plastic cylinder syringe in soft sediments, and cubes were cut with a saw in consolidated materials. Each sample was placed in a labeled glass vial of known mass and volume (measured prior to the cruise). The mass and volume were obtained by subtracting the vial mass and volume from the total mass and volume, respectively.

Measurement of mass

The wet sample mass (M_{wet}) was measured using a dual balance system composed of two Mettler-Toledo XS204 electric balances designed to compensate for ship heave. After taring (zeroing) the balances, a reference mass expected to be similar to that of the sample + container was placed on the reference balance as well as the real sample + container on the "unknown mass" balance. After a cycle of weighing, the reference mass was changed for one that was closer to the measured mass of the sample + container. This process was iterated until the difference between reference and measured masses was <5 g. Once the mass was measured, the wet samples were placed in a convection oven for >24 h at 105° ± 5°C to dry. The dry samples were then cooled in a dessicator for at least 1 h before the dry mass and volume measurements. The dry mass (M_{dry}) was determined using the same mass measurement process. To assess the impact of drying technique and time on mass calculations, and thus on grain density and porosity calculations, we completed two separate drying experiments (ODP Information Technology and Data Services, 2007). In one set of experiments we looked at differences caused by freeze drying in comparison to oven drying. In another set of experiments we looked at differences caused by oven drying for 24 h in comparison to drying for >24 h. Results are provided in PHYSPROP in **Supplementary material**.

Measurement of volume

After measuring dry mass, the sample was placed in a chamber of the Micromeretics AccuPyc 1330TC helium-displacement pycnometer, an IODP custom-built system composed of six cell units, electronics, and control programs. The six cells are mounted in a chassis to protect the electronics and to help provide temperature stability. The system measures dry sample volume using pressurized He-filled chambers with a precision of 0.04 cm^3. For each measurement, five unknown cells and one cell with two stainless steel calibration spheres (3 and 7 cm^3) with a total volume of ~10 cm^3 were run. Calibration spheres were cycled through the cells to identify any systematic error and/or instrument drift. Spheres are assumed known to within 1% of their volume. If the volumes of the calibration spheres deviated by >1% of their known volume, then the specific pycnometer cell was recalibrated.

Phase relations in marine sediments

Saturated marine sediments are composed of fluid (water plus dissolved salt) and solid. From the direct measurements of M_{wet}, M_{dry}, and V_{dry}, and assuming known values for salinity and water properties, we can obtain the mass and volume of each component; pore water mass (M_{water}), pore fluid mass (M_f), salt mass (M_{salt}), mass of solids excluding salt (M_s), pore water volume (V_{water}), pore fluid volume (V_f), salt volume (V_{salt}), and volume of solids excluding salt (V_s):

$$M_{water} = M_{wet} - M_{dry},$$

$$M_f = M_{water}/(1 - s),$$

$$M_{salt} = M_f - M_{water} = M_{water} \times s/(1 - s),$$

$$M_s = M_{wet} - M_f = M_{dry} - M_{salt},$$

$$V_{water} = M_{water}/\rho_{water},$$

$$V_f = M_f/\rho_f = M_{water}/[(1 - s) \times \rho_f],$$

$$V_{salt} = M_{salt}/\rho_{salt} = M_{water} \times s/[(1 - s) \times \rho_{salt}], \text{ and}$$

$$V_s = V_{dry} - V_{salt} = V_{dry} - M_{water} \times s/[(1 - s) \times \rho_{salt}],$$

where

M_{wet} = total mass of the wet sample,
M_{dry} = mass of the dried sample,
s = salinity (0.035%),
ρ_f = density of pore fluid (1.024 g/cm^3),
ρ_{salt} = density of salt (2.220 g/cm^3), and
ρ_{water} = density of water (1.0 g/cm^3).

Calculation of physical properties

Bulk density (ρ_b) and grain density (ρ_g) are calculated as follows:

$$\rho_b = M_{wet}/V_{wet} = M_{wet}/(V_{dry} + V_f - V_{salt}) \text{ and}$$

$$\rho_g = M_s/V_s = M_s/(V_{dry} - V_{salt}),$$

where V_{wet} is the bulk volume of the wet sample determined from the pycnometer measurements of dry volume V_{dry} and the calculated volume of the pore fluid (V_f) and salt (V_{salt}). Porosity (ϕ) and void ratio (e) are obtained by

$$\phi = V_f/V_{wet} \text{ and}$$

$$e = V_f/V_s.$$

Velocity-porosity relationships

Empirical relationships for *P*-wave velocity (V_P) and porosity (ϕ) can be compared to the shipboard measurements (Erickson and Jarrard, 1998). The empirical relation is based on global compilations for "normal" consolidation:

$$V_P = 0.739 + 0.552\phi + 0.305/[(\phi + 0.13)^2 + 0.0725] + 0.61(V_{sh} - 1) \times [X_1 - |X_1|],$$

where

$$X_1 = \tanh[40(\phi - 0.31)]$$

and V_{sh} is the volume of the clay or shale fraction.

For "high" consolidation we use

$$V_P = 1.11 + 0.178\phi + 0.305/[(\phi + 0.135)^2 + 0.0775] + 0.61(V_{sh} - 1) \times [X_2 - |X_2|],$$

where

$$X_2 = \tanh[20(\phi - 0.39)].$$

A sediment is normally consolidated if the stress it is currently under is the highest it has experienced. High consolidation, or overconsolidation occurs when the current stress is less than the sediment has previously experienced.

Undrained shear strength

The undrained shear strength of soft sediments in the working half of the core was determined using an AVS device (Giesa AVS) and a pocket penetrometer. Measurements were made at discrete locations on the working halves as long as the materials permitted; this corresponded to a measurable shear strength <260 kPa. Where possible, the measurements were made near MAD samples. Care was taken to conduct tests within minimally disturbed, homogeneous sediments. Measurements were made on the working half of split cores with vane rotation axis and penetrometer penetration direction perpendicular to the *y*–*z* plane of the core (Figure **F35**).

Shear strength with AVS

Vane shear strength ($S_{u[v]}$) can be determined by the torque required to cause failure (T) and a vane constant (K_v):

$$S_{u[v]} = T/K_v.$$

All vane shear strength measurements were obtained using a vane with a height of 12.7 mm and a blade length of 6.35 mm rotating at an angular speed of 1.5°/s. Failure torque was determined by measuring the rotation of a torsional spring using a spring-specific relation between rotation angle and torque. Vane shear strength results were only reliable for samples with vane shear strength <100–150 kPa. When cracking or core separation occurred, measurements were discarded.

Compressive strength with pocket penetrometer

The pocket penetrometer (model ELE 29-3729) is a spring-operated device used to measure compressive strength by pushing a 6.4 mm diameter probe fully into the split-core surface. The pocket penetrometer provides a measure of unconfined compressive strength (q_u), which can be related to undrained shear strength ($S_{u(penet)}$) by

$$S_{u(penet)} = q_u g/2,$$

where g is acceleration due to gravity. For very soft samples, an adapter foot increased the area of the probe by a factor of 16 to improve the accuracy of the readings.

Thermal conductivity

At steady state, thermal conductivity (k; W/[m·K]) is the coefficient of heat transfer that relates heat flow (q) and thermal gradient (dT/dz) by

$$q = -k(dT/dz),$$

which depends on temperature, pressure, type of saturating fluid, composition, distribution, porosity, structure, and alignment of mineral phases.

The TK04 system measures thermal conductivity by transient heating of the sample with a needle of known heating power and geometry. The temperature of the superconductive needle probe has a quasi-linear relationship with the natural logarithm of the time after the initiation of heating (Blum, 1997). Changes in temperature with time during heating are recorded and used to calculate thermal conductivity. Variable heating power is used for soft and lithified sediments. The measurement time depends on the dimensions of the probe (the larger the probe, the longer the required measuring time). The default measuring time for standard laboratory probes is 80 s. The software controlling the TK04 device uses an approximation method to calculate thermal conductivity and to assess the fit of the heating curve. This method (Blum, 1997) fits discrete windows of the heating curve to a theoretical temperature (T) with time (t) function for a constantly heated line source:

$$T(t) = A_1 + A_2 \ln(t) + A_3 \frac{\ln(t)}{t} + \frac{A_4}{t},$$

where $A_{1–4}$ are constants calculated by linear regression over a series of different time windows. A_1 is the initial temperature. A_2, A_3, and A_4 are related to the geometry of the probe and material properties surrounding the needle probe. These constants define a time-dependent apparent thermal conductivity (k_a) given by

$$k_a(t) = \frac{Q}{4\pi}\left(A_2 + A_3\left[1 - \frac{\ln(t)}{t}\right] - \frac{A_4}{t}\right),$$

where Q is the input heat flux. Each fit to the data provides a possible value of the true thermal conductivity k, given by a local maximum in the function k_a. The quality of each measurement is evaluated using the standard deviation of each least-squares fit; the number of valid solutions for k; and t_{max}, the time at which the maximum in k_a occurs in each case. The value of k output is that for which t_{max} is highest. The software also assesses contact resistance between the probe and the sample to ensure good thermal exchange.

All measurements were made after the cores had equilibrated to ambient laboratory temperature. The instrument measures temperature drift within the sample and does not begin a heating run until sufficient thermal equilibrium is attained. The probe was checked every other day using the MACOR ceramic standard.

For soft sediment, a full-space single-needle probe TeKa TK04 unit (Blum, 1997) is utilized to measure thermal conductivity of whole cores. To insert this probe, a hole was made in the core liner at a position based on visual inspection of the core to avoid dis-

turbed regions. Three repeat measurements were made at the same location; typically the sample was left to equilibrate for 10 min between measurements. Initially the heating power was set in a range recommended for soft sediments, typically 3 W/m.

Thermal conductivity on samples too lithified for insertion of the probe was measured on the working half of the split core with the thermal conductivity meter in half-space mode, using a needle probe embedded in the bottom of a Plexiglass block (Vacquier, 1985). Smooth and flat samples were coated with joint compound for adequate contact with the heating needle to ensure good heat transfer. The heating power was typically set to 1 W/m. The TK04 documentation indicates that heat flow through the Plexiglass block itself is only significant for samples with thermal conductivities <1 W/(m·K).

For hard rock, core pieces from the working half were measured at irregular intervals downhole depending on the availability of homogeneous and relatively vein/crack-free pieces long enough to be measured without edge effects (pieces >7 cm long; i.e., longer than the instrument needle). At least three measurements were performed on each sample to verify the consistency of the results and provide an average value. Thermal joint compound was smeared on the probe during measurement to ensure good contact with the sample.

Downhole measurements

In situ pressure and temperature measurements

Measurements of formation temperature and pore pressure were attempted at selected intervals at Site U1480 to assess the thermal structure of the input sediment section and evaluate in situ pore pressure.

The APCT-3 was deployed to measure formation temperature, and the T2P was unsuccessfully deployed once to measure formation pressure and temperature. The T2P was deployed with the Motion Decoupled Hydraulic Delivery System (MDHDS) (Flemings et al., 2013) in order to decouple the probe from the drill string, thereby reducing heave effects and improving reliability of measurements.

The temperature sensors in the APCT-3 record the temperature of the surrounding formation as it recovers from the instantaneous frictional heating generated when inserting the tool. The formation temperature is estimated from the recorded data by fitting model curves that are specific to the sensor and to the probe geometry (Heesemann et al., 2007). The small size of the T2P tip creates very little frictional heating, and the location of the temperature sensor at its end allows a direct measure of the formation temperature. All successful temperature measurements were used to estimate geothermal gradients, which were combined with the thermal conductivity measurements made on core samples (see **Physical properties**) to provide an estimate of the local vertical heat flow.

Advanced piston corer temperature tool

The APCT-3 fits directly into a modified coring shoe of the APC (Figure **F40**) and consists of a battery pack, data logger, and platinum resistance-temperature device calibrated over a temperature range from 0° to 30°C. Before entering the borehole, the tool is stopped at the seafloor for 5 min to thermally equilibrate with bottom water. After the APC penetrates the sediment, it is held in place for ~10 min as the APCT-3 records the temperature of the cutting shoe every second. Shooting the APC into the formation generates

Figure F40. Tools deployed to measure formation temperature and pore pressure during Expedition 362. A. APCT-3. B. T2P deployed with the MDHDS.

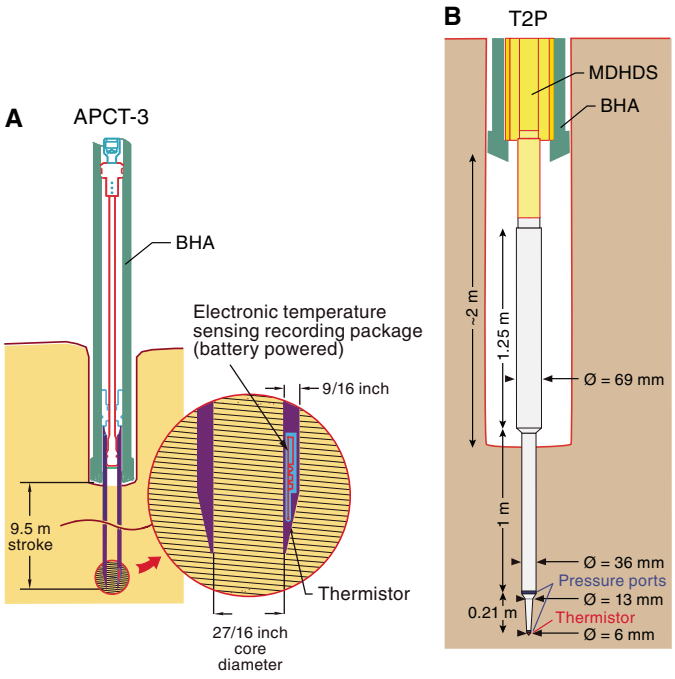

an instantaneous temperature rise from frictional heating. This heat dissipates into the surrounding sediment as the temperature at the APCT-3 equilibrates toward the temperature of the sediment. A model fit of this temperature decay curve provides an estimate of the formation temperature (Heesemann et al., 2007).

Temperature dual-pressure tool

The T2P is a narrow-diameter penetration probe with one temperature sensor and two pressure sensors developed by the University of Texas at Austin to evaluate in situ fluid pressure, hydraulic conductivity, and temperature in low-permeability sediment (Flemings et al., 2006). The T2P measures pressure and temperature at the tool tip and pressure 21 cm up-probe from the tip (Figure **F40B**). The slim design of the T2P facilitates rapid, high-quality measurements of in situ conditions in low-permeability sediment by minimizing pressure and temperature pulses generated during penetration. The two pressure sensors have different dissipation rates because they are at locations on the tool with different diameters (Flemings et al., 2008). Comparison of the dissipation curves allows equilibrium pressure to be interpreted from a shorter part of the recorded dissipation than if only one sensor was used.

The T2P is deployed on a dedicated wireline run including several stations at predefined depths for pressure calibration. Once the MDHDS/T2P assembly reaches the bottom of the BHA, the MDHDS is released using the electronic release system, and the probe is initially driven into the formation by its own mass. It is driven further into the formation by pressuring up the MDHDS. Once the tool is inserted in the formation, the bit is raised by ~2 m for maximum heave accommodation facilitated by the MDHDS, and pressure and temperature are recorded for >30 min. Pressure and temperature data are recorded at a sampling rate of 1 Hz.

Wireline logging

Wireline logs are measurements of physical, chemical, and structural properties of the formation surrounding a borehole that are made by lowering sondes with an electrical wireline in the hole after completion of drilling. The data are acquired continuously with depth (at vertical sampling intervals ranging from 2.5 mm to 15 cm) and are measured in situ. The sampling and depth of investigation are intermediate between laboratory measurements on core samples and geophysical surveys, and provide a link for the integrated understanding of physical properties on a wide range of scales.

Logs can be interpreted in terms of stratigraphy, lithology, mineralogy, physical properties, and geochemical composition. They also provide information on the status and size of the borehole and on possible deformation induced by drilling or formation stress. In intervals where core recovery is incomplete, log data may provide the only way to characterize the formation, and can be used to determine the actual thickness of individual units or lithologies when contacts are not recovered, to pinpoint the actual depth of features in cores with incomplete recovery, or to identify and characterize intervals that were not recovered. Where core recovery is good, log and core data complement one another and may be interpreted jointly.

Operations

Logs are recorded with a variety of tools combined into strings. The measurements planned for Expedition 362 included a full suite of tools to measure spectral gamma ray, porosity, density, resistivity, sonic velocity, acoustic and electrical images of the borehole, and seismic transit times. Because of hole instability and time constraints, only a limited set of data was recorded at each site (Figure **F41**; Tables **T12**, **T13**).

After completion of coring, the bottom of the drill string was set high enough above the bottom of the casing for the longest tool string to fit inside the casing before entering the open hole. The main data were recorded in the open hole section. The gamma ray tool (see below) is the only tool that provides meaningful data inside the drill pipe or casing (mostly qualitative). Such data are used primarily to identify the depth of the seafloor but can also be used for stratigraphic characterization.

Each deployment of a tool string is a logging run, starting with the assembly of the tools and the necessary calibrations. The tool string is then lowered to the bottom of the hole while recording a partial set of data and pulled back uphole at a constant speed, typically 250–500 m/h, to record the main data. During each run, tool strings can be lowered and pulled up several times for control on repeatability or to try to improve quality or coverage of the data. Each lowering or raising of the tool string while collecting data constitutes a pass. During each pass the incoming data are monitored in real time and recorded on the surface system.

Logged properties and tool measurement principles

The main logs recorded during Expedition 362 are listed in Table **T13**. More detailed information on individual tools and their geological applications may be found in Ellis and Singer (2007), Goldberg (1997), Rider (1996), Schlumberger (1989), and Serra (1984, 1986). A complete online list of acronyms for the Schlumberger tools and measurement curves is available at **http://www.apps.slb.com/cmd/index.aspx**.

Figure F41. Wireline tool strings used during Expedition 362. A. Hole U1480G. B. Hole U1481A. See Table **T13** for tool acronyms.

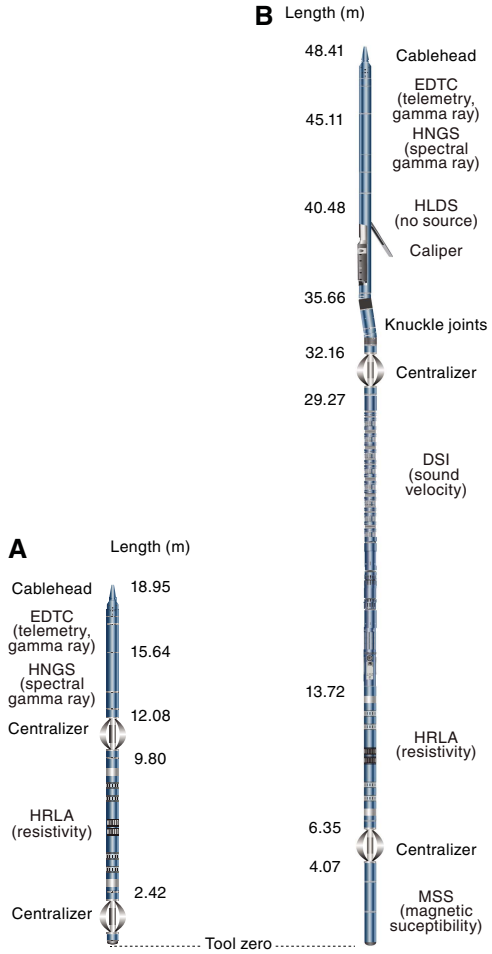

Table T12. Downhole measurements made by wireline tool strings during Expedition 362. All tool names are trademarks of Schlumberger. Sampling interval based on optimal logging speed. For definitions of tool acronyms, see Table **T13**. **Download table in .csv format.**

Tool	Measurement	Sampling interval (cm)	Vertical resolution (cm)	Depth of investigation (cm)
EDTC	Total gamma ray	5 and 15	30	61
HNGS	Spectral gamma ray	15	20–30	61
HRLA	Resistivity	15	30	50
DSI	Acoustic velocity	15	107	23
MSS	Magnetic susceptibility	2.54	40	20

Natural radioactivity

The Hostile Environment Natural Gamma Ray Sonde (HNGS) was used on all tool strings to measure natural radioactivity in the formation. The HNGS uses two bismuth germanate scintillation detectors and five-window spectroscopy to determine concentrations of K, Th, and U, whose radioactive isotopes dominate the natural radiation spectrum.

The enhanced telemetry cartridge (EDTC; see **Telemetry cartridges**), which is used primarily to communicate data to the sur-

Table T13. Acronyms and units used for downhole wireline tools, data and measurements. **Download table in .csv format.**

Tool	Output	Description	Unit
EDTC		Enhanced Digital Telemetry Cartridge	
	GR	Total gamma ray	gAPI
	ECGR	Environmentally corrected gamma ray	gAPI
	EHGR	High-resolution environmentally corrected gamma ray	gAPI
HNGS		Hostile Environment Gamma Ray Sonde	
	HSGR	Standard (total) gamma ray	gAPI
	HCGR	Computed gamma ray (HSGR minus uranium contribution)	gAPI
	HFK	Potassium	Wt%
	HTHO	Thorium	ppm
	HURA	Uranium	ppm
HLDS		Hostile Environment Litho-Density Sonde	
	LCAL	Caliper (measure of borehole diameter)	Inch
HRLA		High-Resolution Laterolog Array	
	RLA*x*	Apparent resistivity from mode *x* (*x* from 1 to 5, shallow to deep)	Ωm
	RT	True resistivity	Ωm
	MRES	Borehole fluid resistivity	Ωm
DSI		Dipole Sonic Imager	
	DTCO	Compressional wave slowness	µs/ft
	DTST	Stonely wave slowness	µs/ft
	DT1	Shear wave slowness, lower dipole	µs/ft
	DT2	Shear wave slowness, upper dipole	µs/ft
MSS		Magnetic susceptibility sonde	
	LSUS	Magnetic susceptibility, deep reading	Uncalibrated units

face, includes a sodium iodide scintillation detector to measure the total natural gamma ray emission. It is not a spectral tool, but it provides an additional high-resolution total gamma ray measurement for each pass.

Density

The Hostile Environment Litho-Density Sonde (HLDS) normally uses a radioactive cesium (^{137}Cs) gamma ray source to measure the formation density. Because of concerns about hole stability, the HLDS was run without the source in Hole U1481A, using its extended arm to provide a caliper log of the size of the borehole that can be used to assess the data quality and the reliability of measurements that could be affected by an enlarged or irregular borehole.

Electrical resistivity

The High-Resolution Laterolog Array (HRLA) provides six resistivity measurements with different depths of investigation (including the borehole fluid or mud resistivity and five measurements of formation resistivity with increasing penetration into the formation). The sonde sends a focused current beam into the formation and measures the intensity necessary to maintain a constant drop in voltage across a fixed interval, providing a direct resistivity measurement. The array has one central source electrode and six electrodes above and below it, which serve alternately as focusing and returning current electrodes. By rapidly changing the role of these electrodes, a simultaneous resistivity measurement is achieved at six penetration depths.

Typically, minerals found in sedimentary and crustal rocks are electrical insulators, whereas ionic solutions like pore water are conductors. In most rocks, electrical conduction occurs primarily by ion transport through pore fluids and is strongly dependent on the porosity, the type of pores and connectivity, the permeability, and the pore fluid.

Acoustic velocity

The Dipole Shear Sonic Imager (DSI) generates acoustic pulses from various sonic transmitters and records the waveforms with an array of eight receivers. The waveforms are then used to calculate the sonic velocity in the formation. The omnidirectional monopole transmitter emits high-frequency (5–15 kHz) pulses to extract the compressional velocity (V_P) of the formation, as well as the shear velocity (V_S) when it is faster than the sound velocity in the borehole fluid. The same transmitter can be fired in sequence at a lower frequency (0.5–1 kHz) to generate Stoneley waves that are sensitive to fractures and variations in permeability. The DSI also has two dipole transmitters generating flexural waves along the borehole that allow the measurement of shear wave velocity in "slow" formations, where V_S is slower than the velocity in the borehole fluid.

Magnetic susceptibility

The Magnetic Susceptibility Sonde, a tool designed by Lamont-Doherty Earth Observatory (LDEO), measures the ease with which formations are magnetized when subjected to the Earth's magnetic field. This is ultimately related to the concentration and composition (size, shape, and mineralogy) of magnetizable material within the formation. These measurements provide one of the best methods for investigating stratigraphic changes in mineralogy and lithology because the measurement is quick, repeatable, and because different lithologies often have strongly contrasting susceptibilities. In particular, volcanoclastic deposits can have a very distinct magnetic susceptibility signature. The data can be compared to the susceptibility measurements made on the recovered core by the WRMSL and the point magnetic susceptibility measurements of the SHMSL (see **Physical properties**). The sensor used during Expedition 362 was a dual-coil sensor providing deep-reading measurements, with a vertical resolution of ~40 cm.

Auxiliary logging equipment

Cable head

The Schlumberger logging equipment head (or cable head) measures tension at the very top of the wireline tool string, which diagnoses difficulties in running the tool string up or down the borehole or when exiting or entering the drill string or casing.

Telemetry cartridges

Telemetry cartridges are used in each tool string to transmit the data in real time from the tools to the surface. The EDTC also includes a sodium iodide scintillation detector to measure the total natural gamma ray emission of the formation, which can be used to help match depths between the different passes and runs.

Joints and adapters

Because the tool strings combine tools of different generations and with various designs, they include several adapters and joints between individual tools to allow communication, provide isolation, avoid interferences (mechanical and acoustic), terminate wirings, or position the tool properly in the borehole. Knuckle joints in particular were used to allow some of the tools such as the HRLA to remain centralized in the borehole while the overlying HLDS sonde was pressed against the borehole wall.

All these additions are included and contribute to the total length of the tool strings in Figure **F41**.

Log data quality

The principal factor in the quality of log data is the condition of the borehole. If the borehole diameter varies over short intervals because of washouts or ledges, the logs from tools that require good contact with the borehole wall may be degraded. Deep investigation measurements such as gamma ray, resistivity, and sonic velocity, which do not require contact with the borehole wall, are generally less sensitive to borehole conditions. Very narrow ("bridged") sections will also cause irregular log results.

The accuracy of the logging depth depends on several factors. The depth of the logging measurements is determined from the length of the cable spooled out from the winch on the ship. Uncertainties in logging depth occur because of ship heave, cable stretch, cable slip, or even tidal changes. Similarly, uncertainties in the depth of the core samples occur because of incomplete core recovery or incomplete heave compensation. All these factors generate some depth discrepancy between core samples and logs, and between individual logging passes. The gamma ray log recorded during each logging pass is used to match the logging depths (see below) and provide depth consistency across all logging data. To minimize the effect of ship heave, a hydraulic wireline heave compensator (WHC) was used to adjust the wireline length for rig motion during wireline logging operations.

Wireline heave compensator

The WHC system is designed to compensate for the vertical motion of the ship and maintain a steady motion of the logging tools. It uses vertical acceleration measurements made by a Motion Reference Unit located under the rig floor near the ship's center of gravity to calculate the vertical motion of the ship. It then adjusts the length of the wireline by varying the distance between two sets of pulleys through which the wireline passes.

Logging data flow and processing

Data from each logging run were monitored in real time and recorded using the Schlumberger MAXIS 500 system. The data were shortly thereafter transferred to LDEO for standardized processing, formatting for the online logging database, and archiving. The processed data were returned to the ship and made available to the shipboard scientists within a couple of days.

The processing includes several stages. First, using the gamma ray logs recorded by every tool string, a visually interactive program is used to match the depths of recognizable features across all the passes to a reference curve, commonly the gamma ray log of the longest upward pass. After depth matching, all the logging depths are shifted to the seafloor based on the seafloor identified by a step in the gamma ray profile. All the processed data are made available in ASCII and DLIS formats for most logs and in GIF for the images.

Core-log-seismic integration

During Expedition 362, we carried out two primary core-log-seismic integration activities. First, at Site U1480 where multiple holes were drilled, we used physical property measurements made on the cores to establish a depth correlation between holes and to build a composite depth scale. Second, we used information from the cores and from wireline logs to establish links to the seismic reflection data used for site selection (Gaedicke, 2007; Geersen et al., 2013). This information includes both continuous and discrete physical property measurements on the cores, wireline log data, and a detailed interpretation of the seismic profiles at the site.

Interhole depth correlations

The principal physical properties used to establish depth correlations between holes were NGR and magnetic susceptibility. These are volume-averaging measurements that are likely to be less affected by drilling disturbance than *P*-wave velocity or bulk density data. The color reflectance values measured on the split cores were also used. The depth model was generated using Correlator version 2.1rc2, and the resulting affine tables were uploaded into the LIMS database. Finally, the full range of physical property data was checked using the constructed affine table.

Seismic reflection data

The primary seismic reflection data for Sites U1480 and U1481 were collected on FS *Sonne* during the SEACAUSE campaign in 2006 (Gaedicke, 2007) using a tuned array of 16 air guns with total volume of 50.4 L, towed at 6 m depth and fired every 50 m, and a 3 km 240 channel hydrophone streamer towed at 9 m depth. The data were stacked and migrated using a Kirchhoff poststack time migration. Because of the water depth at the sites, the first seafloor multiple is beyond the zone of interest. The data have a dominant period of 20 ms, which is approximately constant throughout the sediment column; hence, the vertical resolution estimated from the data (quarter wavelength) is 7.5 m at the seafloor increasing to 15–20 m in the deepest sediments. The width of the first Fresnel zone at the seafloor is 120 m, and the horizontal resolution based on residual diffracted energy at fault planes is 50 m. Although this is a 2-D data set, the expected lateral variability is limited, and there is little evidence of out-of-the-plane energy close to the sites. A secondary data set used in assessing site locations was collected on the R/V *Marion Dufresne* during Cruise MD 116 in 2000 (Chamot-Rooke, 2000).

Correlation between seismic data and holes

The key task of correlation between the seismic data (recorded in time) and the borehole data (measured in depth) is to determine a time-depth relationship. This can best be achieved by using downhole logs and particularly a vertical seismic profile. Unfortunately, a combination of hole conditions and time constraints resulted in a limited set of logs at both sites. No sonic logs were recorded at Site U1480. A time-depth relationship was established for this site using a combination of the lithology and physical properties measured on core samples to determine ties between changes in these properties and characteristic seismic reflections. At Site U1481, sonic logs were successfully collected throughout the uncased interval to the bottom of the hole, and the time offset from the seabed through the cased interval was determined by comparing the logs with the seismic reflection data.

Seismic reflectivity

At Site U1480, we made additional ties between the cores and the seismic reflection data by comparing the reflectivity with the acoustic impedance (product of *P*-wave velocity and density) using the best available values for *P*-wave velocity and density to determine the impedance. Seismic velocity data were selected from PWL and PWC *P*-wave velocity, using a 5 m median filter to exclude outliers and extract trends on a scale similar to the seismic reflection

wavelengths. Bulk density values from both GRA density data and from MAD core sample measurements were then used to make correlations between intervals in the core that would produce strong reflections in the seismic profiles, giving additional time-depth tie points.

At Site U1481, the cored section of the hole started at 1150 mbsf, so there was no fix at the seafloor. Sonic logs were available from the bottom of the casing at ~730 mbsf to just above the base of the hole (1494 mbsf), but the traveltime to 730 mbsf is unknown. The sonic logs were used to create synthetic seismograms with bandwidth equivalent to the seismic reflection profiles, and these were compared against the seismic profiles to determine the depth-time tie based on correlation between predicted and observed reflectivity.

Correlation to coring data

Once a satisfactory correlation between the seismic, log, and core data was established, intervals with complementary data were examined. This included the main unit boundaries (unconformity below the recent trench-wedge material, onset of Nicobar Fan deposition, and the sediment/basement interface), as well as other key reflections such as Horizon C, which correlates with the Dean et al. (2010) high-amplitude negative polarity event nearer the subduction zone and is a potential décollement horizon.

References

Agini, C., Fornaciari, E., Raffi, I., Catanzariti, R., Pälike, H., Backman, J., and Rio, D., 2014. Biozonation and biochronology of Paleogene calcareous nannofossils from low and middle latitudes. *Newsletters on Stratigraphy,* 47(2):131–181. **http://dx.doi.org/10.1127/0078-0421/2014/0042**

Anthonissen, D.E., and Ogg, J.G., 2012. Appendix 3—Cenozoic and Cretaceous biochronology of planktonic foraminifera and calcareous nannofossils. *In* Gradstein, F.M., Ogg, J.G., Schmitz, M.D., and Ogg, G.M., (Eds.), *The Geologic Time Scale 2012:* Amsterdam (Elsevier), 1083–1127. **http://dx.doi.org/10.1016/B978-0-444-59425-9.15003-6**

Backman, J., Raffi, I., Rio, D., Fornaciari, E., and Pälike, H., 2012. Biozonation and biochronology of Miocene through Pleistocene calcareous nannofossils from low and middle latitudes. *Newsletters on Stratigraphy,* 45(3):221–244. **http://dx.doi.org/10.1127/0078-0421/2012/0022**

Baldauf, J.G., 1985. A high resolution late Miocene–Pliocene diatom biostratigraphy for the eastern equatorial Pacific. *In* Mayer, L., Theyer, F., Thomas, E., et al., *Initial Reports of the Deep Sea Drilling Project,* 85: Washington, DC (U.S. Government Printing Office), 457–475. **http://dx.doi.org/10.2973/dsdp.proc.85.109.1985**

Barron, J., Bukry, D., and Gersonde, R., 2014. Diatom and silicoflagellate biostratigraphy for the late Eocene: ODP 1090 (sub-Antarctic Atlantic). *In* Kociolek, J.P., Kulikovskiy, M.S., Witkowski, J.A., and Harwood, D.M. (Eds.), *Nova Hedwigia Beihefte Series* (Volume 143): *Diatom Research over Time and Space*: Stuttgart, Germany (Schweizerbart Science Publishers), 1–31.

Barron, J.A., 1992. Neogene diatom datum levels in the equatorial and North Pacific. *In* Ishizaki, K., and Saito, T. (Eds.), *Centenary of Japanese Micropaleontology:* Tokyo (Terra Scientific Publishing Company), 413–425. **http://www.terrapub.co.jp/e-library/cjm/pdf/0413.pdf**

Barron, J.A., 2006. Diatom biochronology for the early Miocene of the equatorial Pacific. *Stratigraphy,* 2(4):281–309. **http://sedis.iodp.org/pub-catalogue/index.php?id=2006-071151**

Barron, J.A., Fourtanier, E., and Bohaty, S.M., 2004. Oligocene and earliest Miocene diatom biostratigraphy of ODP Leg 199 Site 1220, equatorial Pacific. *In* Wilson, P.A., Lyle, M., Janecek, T.R., and Firth, J.V. (Eds.), *Proceedings of the Ocean Drilling Program, Scientific Results,* 199: College Station, TX (Ocean Drilling Program), 1–25. **http://dx.doi.org/10.2973/odp.proc.sr.199.204.2004**

Barron, J.A., and Gladenkov, A.Y., 1995. Early Miocene to Pleistocene diatom stratigraphy of Leg 145. *In* Rea, D.K., Basov, I.A., Scholl, D.W., and Allan, J.F. (Eds.), *Proceedings of the Ocean Drilling Program, Scientific Results,* 145: College Station, TX (Ocean Drilling Program), 3–19. **http://dx.doi.org/10.2973/odp.proc.sr.145.101.1995**

Barron, J.A., Stickley, C.E., and Bukry, D., 2015. Paleoceanographic, and paleoclimatic constraints on the global Eocene diatom and silicoflagellate record. *Palaeogeography, Palaeoclimatology, Palaeoecology,* 422:85–100. **http://dx.doi.org/10.1016/j.palaeo.2015.01.015**

Bartington Instruments, Ltd., 2011. *Operation Manual for MS2 Magnetic Susceptibility System:* Oxford, United Kingdom (Bartington Instruments, Ltd.). **http://www.bartington.com/Literaturepdf/Operation%20Manuals/om0408%20MS2.pdf**

Berggren, W.A., Kent, D.V., Swisher, C.C., III, and Aubry, M.-P., 1995. A revised Cenozoic geochronology and chronostratigraphy. *In* Berggren, W.A., Kent, D.V., Aubry, M.-P., and Hardenbol, J. (Eds.), *Geochronology, Time Scales and Global Stratigraphic Correlation.* Special Publication - SEPM (Society for Sedimentary Geology), 54:129–212. **http://dx.doi.org/10.2110/pec.95.04.0129**

Berggren, W.A., and Pearson, P.N., 2005. A revised tropical to subtropical Paleogene planktonic foraminiferal zonation. *Journal of Foraminiferal Research,* 35(4):279–298. **http://dx.doi.org/10.2113/35.4.279**

Bjornsson, E., Hucik, B., Szutiak, G., Brown, L.A., Jr., Evans, H., Curry, D., and Perry, P., 2004. Drilling optimization using bit selection expert system and ROP prediction algorithm improves drilling performance and enhances operational decision making by reducing performance uncertainties [paper presented at the SPE Annual Technical Conference and Exhibition, Houston, Texas, 26–29 September 2004]. (Abstract SPE-90752-MS) **http://dx.doi.org/10.2118/90752-MS**

Blenkinsop, T.G., and Doyle, M.G., 2010. A method for measuring the orientations of planar structures in cut core. *Journal of Structural Geology,* 32(6):741–745. **http://dx.doi.org/10.1016/j.jsg.2010.04.011**

Blow, W.H., 1979. *The Cainozoic Foraminifera* (Volumes 1–3): Leiden, The Netherlands (E.J. Brill).

Blum, P., 1997. *Technical Note 26: Physical Properties Handbook—A Guide to the Shipboard Measurement of Physical Properties of Deep-Sea Cores.* Ocean Drilling Program. **http://dx.doi.org/10.2973/odp.tn.26.1997**

Bolli, H.M., and Saunders, J.B., 1985. Oligocene to Holocene low latitude planktic foraminifera. *In* Bolli, H.M., Saunders, J.B., and Perch-Nielsen, K. (Eds.), *Plankton Stratigraphy* (Volume 1): *Planktic Foraminifera, Calcareous Nannofossils and Calpionellids:* Cambridge, United Kingdom (Cambridge University Press), 155–262.

Bown, P.R. (Ed.), 1998. *Calcareous Nannofossil Biostratigraphy:* London (Chapman and Hall).

Bown, P.R., 2005. Palaeogene calcareous microfossils from the Kilwa and Lindi areas of coastal Tanzania (Tanzania Drilling Project 2003–4). *Journal of Nannoplankton Research,* 27(1):21–95.

Burckle, L.H., 1972. Late Cenozoic planktonic diatom zones from the eastern equatorial Pacific. *In* Simonsen, R. (Ed.), *First Symposium on Recent and Fossil Marine Diatoms* (Bremenhaven, Germany, 21–26 September 1970). Beihefte zur Nova Hedwigia, 39:217–249.

Burnett, J.A., 1998. Upper Cretaceous. *In* Bown, P.R. (Ed.), *Calcareous Nannofossil Biostratigraphy:* Dordrecht, The Netherlands (Kluwer Academic Publishing), 132–199.

Caicedo, H.U., Calhoun, W.M., and Ewy, R.T., 2005. Unique ROP predictor using bit-specific coefficient of sliding friction and mechanical efficiency as a function of confined compressive strength impacts drilling performance [paper presented at SPE/IADC Drilling Conference, Amsterdam, The Netherlands, 23–25 February 2005]. (Abstract SPE-92576-MS) **http://dx.doi.org/10.2118/92576-MS**

Caron, M., 1985. Cretaceous planktic foraminifera. *In* Bolli, H.M., Saunders, J.B., and Perch-Nielsen, K. (Eds.), *Plankton Stratigraphy:* Cambridge, United Kingdom (Cambridge University Press), 17–86.

Chamot-Rooke, N., 2000. MD 116/ANDAMAN cruise report, RV *Marion Dufresne*. **http://dx.doi.org/10.17600/200030**

Channell, J.E.T., Xuan, C., and Hodell, D.A., 2009. Stacking paleointensity and oxygen isotope data for the last 1.5 Myr (PISO-1500). *Earth and Plane-*

tary Science Letters, 283(1–4):14–23. **http://dx.doi.org/10.1016/j.epsl.2009.03.012**

Clemens, S.C., Kuhnt, W., LeVay, L.J., Anand, P., Ando, T., Bartol, M., Bolton, C.T., Ding, X., Gariboldi, K., Giosan, L., Hathorne, E.C., Huang, Y., Jaiswal, P., Kim, S., Kirkpatrick, J.B., Littler, K., Marino, G., Martinez, P., Naik, D., Peketi, A., Phillips, S.C., Robinson, M.M., Romero, O.E., Sagar, N., Taladay, K.B., Taylor, S.N., Thirumalai, K., Uramoto, G., Usui, Y., Wang, J., Yamamoto, M., and Zhou, L., 2016. Expedition 353 methods. *In* Clemens, S.C., Kuhnt, W., LeVay, L.J., and the Expedition 353 Scientists, *Indian Monsoon Rainfall*. Proceedings of the International Ocean Discovery Program, 353: College Station, TX (International Ocean Discovery Program). **http://dx.doi.org/10.14379/iodp.proc.353.102.2016**

Coccioni, R., Monaco, P., Monechi, S., Nocchi, M., and Parisi, G., 1988. Biostratigraphy of the Eocene-Oligocene boundary at Massignano (Ancona, Italy). *In* Premoli Silva, I., Coccioni, R., and Montanari, A. (Eds.), *The Eocene-Oligocene Boundary in the Marche-Umbria Basin (Italy):* Ancona, Italy (International Union of Geological Sciences), 59–80.

Cox, A., and Gordon, R.G., 1984. Paleolatitudes determined from paleomagnetic data from vertical cores. *Reviews of Geophysics and Space Physics,* 22(1):47–71. **http://dx.doi.org/10.1029/RG022i001p00047**

De Wever, P., Dumitrica, P., Caulet, J.-P., Nigrini, C., and Caridroit, M., 2001. *Radiolarians in the Sedimentary Record:* New York (Gordon and Breach Science Publishers).

Dean, S.M., McNeill, L.C., Henstock, T.J., Bull, J.M., Gulick, S.P.S., Austin, J.A., Jr., Bangs, N.L.B., Djajadihardja, Y.S., and Permana, H., 2010. Contrasting décollement and prism properties over the Sumatra 2004–2005 earthquake rupture boundary. *Science,* 329(5988):207–210. **http://dx.doi.org/10.1126/science.1189373**

Droser, M.L., and Bottjer, D.J., 1986. A semiquantitative field classification of ichnofabric. *Journal of Sedimentary Research,* 56(4):558–559. **http://dx.doi.org/10.1306/212F89C2-2B24-11D7-8648000102C1865D**

Droser, M.L., and Bottjer, D.J., 1991. Trace fossils and ichnofabric in Leg 119 cores. *In* Barron, J., Larsen, B., et al., *Proceedings of the Ocean Drilling Program, Scientific Results,* 119: College Station, TX (Ocean Drilling Program), 635–641. **http://dx.doi.org/10.2973/odp.proc.sr.119.206.1991**

Dupriest, F.E., and Koederitz, W.L., 2005. Maximizing drill rates with real-time surveillance of mechanical specific energy [paper presented at the SPE/IADC Drilling Conference, Amsterdam, The Netherlands, 23–25 February 2005]. (Abstract SPE-92194-MS) **http://dx.doi.org/10.2118/92194-MS**

Dupriest, F.E., Witt, J.W., and Remmert, S.M., 2005. Maximizing ROP with real-time analysis of digital data and MSE [paper presented at the International Petroleum Technology Conference, Doha, Qatar, 21–23 November 2005]. (Abstract IPTC-10706-MS) **http://dx.doi.org/10.2523/IPTC-10607-MS**

Ellis, D.V., and Singer, J.M., 2007. *Well Logging for Earth Scientists* (2nd edition): New York (Elsevier).

Erickson, S.N., and Jarrard, R.D., 1998. Velocity-porosity relationships for water-saturated siliciclastic sediments. *Journal of Geophysical Research: Solid Earth,* 103(B12):30385–30406. **http://dx.doi.org/10.1029/98JB02128**

Expedition 334 Scientists, 2012. Methods. *In* Vannucchi, P., Ujiie, K., Stroncik, N., Malinverno, A., and the Expedition 334 Scientists, *Proceedings of the Integrated Ocean Drilling Program,* 334: Tokyo (Integrated Ocean Drilling Program Management International, Inc.). **http://dx.doi.org/10.2204/iodp.proc.334.102.2012**

Fisher, R.V., and Schmincke, H.-U., 1984. *Pyroclastic Rocks:* Berlin (Springer-Verlag). **http://dx.doi.org/10.1007/978-3-642-74864-6**

Flemings, P.B., Long, H., Dugan, B., Germaine, J., John, C.M., Behrmann, J.H., Sawyer, D., and IODP Expedition 308 Scientists, 2008. Pore pressure penetrometers document high overpressure near the seafloor where multiple submarine landslides have occurred on the continental slope, offshore Louisiana, Gulf of Mexico. *Earth and Planetary Science Letters,* 269(3–4):309–325. **http://dx.doi.org/10.1016/j.epsl.2007.12.005**

Flemings, P.B., Polito, P.J., Pettigrew, T.L., Iturrino, G.J., Meissner, E., Aduddell, R., Brooks, D.L., Hetmaniak, C., Huey, D., Germaine, J.T., and the IODP Expedition 342 Scientists, 2013. The Motion Decoupled Delivery System: a new deployment system for downhole tools is tested at the New Jersey margin. *Scientific Drilling,* 15:51–56. **http://dx.doi.org/10.2204/iodp.sd.15.07.2013**

Folk, R.L., 1980. *Petrology of Sedimentary Rocks* (2nd edition): Austin, TX (Hemphill's).

Fourtanier, E., 1991a. Diatom biostratigraphy of equatorial Indian Ocean Site 758. *In* Weissel, J., Peirce, J., Taylor, E., Alt, J., et al., *Proceedings of the Ocean Drilling Program, Scientific Results,* 121: College Station, TX (Ocean Drilling Program), 189–208. **http://dx.doi.org/10.2973/odp.proc.sr.121.137.1991**

Fourtanier, E., 1991b. Paleocene and Eocene diatom biostratigraphy and taxonomy of eastern Indian Ocean Site 752. *In* Weissel, J., Peirce, J., Taylor, E., Alt, J., et al., *Proceedings of the Ocean Drilling Program, Scientific Results,* 121: College Station, TX (Ocean Drilling Program), 171–187. **http://dx.doi.org/10.2973/odp.proc.sr.121.136.1991**

France-Lanord, C., Spiess, V., Klaus, A., Adhikari, R.R., Adhikari, S.K., Bahk, J.-J., Baxter, A.T., Cruz, J.W., Das, S.K., Dekens, P., Duleba, W., Fox, L.R., Galy, A., Galy, V., Ge, J., Gleason, J.D., Gyawali, B.R., Huyghe, P., Jia, G., Lantzsch, H., Manoj, M.C., Martos Martin, Y., Meynadier, L., Najman, Y.M.R., Nakajima, A., Ponton, C., Reilly, B.T., Rogers, K.G., Savian, J.F., Schwenk, T., Selkin, P.A., Weber, M.E., Williams, T., and Yoshida, K., 2016. Expedition 354 methods. *In* France-Lanord, C., Spiess, V., Klaus, A., Schwenk, T., and the Expedition 354 Scientists, *Bengal Fan.* Proceedings of the International Ocean Discovery Program, 354: College Station, TX (International Ocean Discovery Program). **http://dx.doi.org/10.14379/iodp.proc.354.102.2016**

Fuller, M., 1969. Magnetic orientation of borehole cores. *Geophysics,* 34(5):772–774. **http://dx.doi.org/10.1190/1.1440047**

Gaedicke, C., 2007. SEACAUSE Cruise SO186-2 report. **http://www.bgr.bund.de/EN/Themen/MarineRohstofforschung/Projekte/HC-Potential-of-continental-margins/Abgeschlossen/forschungsfahrt_SO_186_2_en.html**.

Gartner, S., 1974. Nannofossil biostratigraphy, Leg 22, Deep Sea Drilling Project. *In* von der Borch, C.C., Sclater, J.G., et al., *Initial Reports of the Deep Sea Drilling Project,* 22: Washington, DC (U.S. Government Printing Office), 577–599. **http://dx.doi.org/10.2973/dsdp.proc.22.126.1974**

Gee, J.S., Tauxe, L., and Constable, C., 2008. AMSSpin: a LabVIEW program for measuring the anisotropy of magnetic susceptibility with the Kappabridge KLY-4S. *Geochemistry, Geophysics, Geosystems,* 9(8):Q08Y02. **http://dx.doi.org/10.1029/2008GC001976**

Geersen, J., McNeill, L., Henstock, T.J., and Gaedicke, C., 2013. The 2004 Aceh-Andaman earthquake: early clay dehydration controls shallow seismic rupture. *Geochemistry, Geophysics, Geosystems,* 14(9):3315–3323. **http://dx.doi.org/10.1002/ggge.20193**

Gieskes, J.M., Gamo, T., and Brumsack, H., 1991. *Technical Note 15: Chemical Methods for Interstitial Water Analysis Aboard JOIDES Resolution.* Ocean Drilling Program. **http://dx.doi.org/10.2973/odp.tn.15.1991**

Goldberg, D., 1997. The role of downhole measurements in marine geology and geophysics. *Reviews of Geophysics,* 35(3):315–342. **http://dx.doi.org/10.1029/97RG00221**

Graber, K.K., Pollard, E., Jonasson, B., and Schulte, E. (Eds.), 2002. *Technical Note 31: Overview of Ocean Drilling Program engineering tools and hardware.* Ocean Drilling Program. **http://dx.doi.org/10.2973/odp.tn.31.2002**

Guyodo, Y., and Valet, J.-P., 1999. Global changes in intensity of the Earth's magnetic field during the past 800 kyr. *Nature,* 399(6733):249–252. **http://dx.doi.org/10.1038/20420**

Harris, R.N., Sakaguchi, A., Petronotis, K., Baxter, A.T., Berg, R., Burkett, A., Charpentier, D., Choi, J., Diz Ferreiro, P., Hamahashi, M., Hashimoto, Y., Heydolph, K., Jovane, L., Kastner, M., Kurz, W., Kutterolf, S.O., Li, Y., Malinverno, A., Martin, K.M., Millan, C., Nascimento, D.B., Saito, S., Sandoval Gutierrez, M.I., Screaton, E.J., Smith-Duque, C.E., Solomon, E.A., Straub, S.M., Tanikawa, W., Torres, M.E., Uchimura, H., Vannucchi, P., Yamamoto, Y., Yan, Q., and Zhao, X., 2013. Methods. *In* Harris, R.N., Sakaguchi, A., Petronotis, K., and the Expedition 344 Scientists, *Proceedings of the Integrated Ocean Drilling Program,* 344: College Station, TX

(Integrated Ocean Drilling Program). **http://dx.doi.org/10.2204/iodp.proc.344.102.2013**

Heard, T.G., Pickering, K.T., and Clark, J.D. 2014. Ichnofabric characterization of a deep-marine clastic system: a subsurface study of the middle Eocene Ainsa System, Spanish Pyrenees. *Sedimentology,* 61(5):1298–1331. **http://dx.doi.org/10.1111/sed.12101**

Heard, T.G., Pickering, K.T., and Robinson, S.A., 2008. Milankovitch forcing of bioturbation intensity in deep-marine thin-bedded siliciclastic turbidites. *Earth and Planetary Science Letters,* 272(1–2):130–138. **http://dx.doi.org/10.1016/j.epsl.2008.04.025**

Heesemann, M., Villinger, H., Fisher, A.T., Tréhu, A.M., and White, S., 2006. Data report: testing and deployment of the new APCT-3 tool to determine in situ temperatures while piston coring. *In* Riedel, M., Collett, T.S., Malone, M.J., and the Expedition 311 Scientists. *Proceedings of the Integrated Ocean Drilling Program,* 311: Washington, DC (Integrated Ocean Drilling Program Management International, Inc.). **http://dx.doi.org/10.2204/iodp.proc.311.108.2006**

Hilgen, F.J., Lourens, L.J., and Van Dam, J.A., 2012. The Neogene period. With contributions by A.G. Beu, A.F. Boyes, R.A. Cooper, W. Krijgsman, J.G. Ogg, W.E. Piller, and D.S. Wilson. *In* Gradstein, F.M., Ogg, J.G., Schmitz, M.D., and Ogg, G.M. (Eds.), *The Geologic Time Scale:* Oxford, United Kingdom (Elsevier), 923–978. **http://dx.doi.org/10.1016/B978-0-444-59425-9.00029-9**

Hollis, C.J., 2002. Biostratigraphy and paleoceanographic significance of Paleocene radiolarians from offshore eastern New Zealand. *Marine Micropaleontology,* 46:265–316. **http://dx.doi.org/10.1016/S0377-8398(02)00066-X**

Husson, D., Galbrun, B., Laskar, J., Hinnov, L.A., Thibault, N., Gardin, S., and Lockair, R.E., 2011. Astronomical calibration of the Maastrichtian (Late Cretaceous). *Earth and Planetary Science Letters,* 305(3–4):328–340. **http://dx.doi.org/10.1016/j.epsl.2011.03.008**

Johnson, D.A., and Nigrini, C.A., 1985. Synchronous and time-transgressive Neogene radiolarian datum levels in the equatorial Indian and Pacific Oceans. *Marine Micropaleontology,* 9(6):489–524. **http://dx.doi.org/10.1016/0377-8398(85)90015-5**

Jutzeler, M., White, J.D.L., Talling, P.J., McCanta, M., Morgan, S., Le Friant, A., and Ishizuka, O., 2014. Coring disturbances in IODP piston cores with implications for offshore record of volcanic events and the Missoula megafloods. *Geochemistry, Geophysics, Geosystems,* 15(9):3572–3590. **http://dx.doi.org/10.1002/2014GC005447**

Kamikuri, S., and Wade, B.S., 2012. Radiolarian magnetobiochronology and faunal turnover across the middle/late Eocene boundary at Ocean Drilling Program Site 1052 in the western North Atlantic Ocean. *Marine Micropaleontology,* 88–89:41–53. **http://dx.doi.org/10.1016/j.marmicro.2012.03.001**

Kennett, J.P., and Srinivasan, M.S., 1983. *Neogene Planktonic Foraminifera: A Phylogenetic Atlas:* Stroudsburg, PA (Hutchinson Ross).

Kirschvink, J.L., 1980. The least-squares line and plane and the analysis of palaeomagnetic data. *Geophysical Journal of the Royal Astronomical Society,* 62(3):699–718. **http://dx.doi.org/10.1111/j.1365-246X.1980.tb02601.x**

Koederitz, W.L., 2005. A real-time implementation of MSE [paper presented at the AADE 2005 National Technical Conference and Exhibition, Houston, Texas, 5–7 April 2005]. (Abstract AADE-05-NTCE-66) **http://www.aade.org/app/download/7238811258/AADE-05-NTCE-66+-+Koedertiz.pdf**

Kvenvolden, K.A., and McDonald, T.J., 1986. *Technical Note, 6: Organic Geochemistry on the JOIDES Resolution—An Assay.* Ocean Drilling Program. **http://dx.doi.org/10.2973/odp.tn.6.1986**

Laj, C., Kissel, C., and Beer, J., 2004. High resolution global paleointensity stack since 75 kyr (GLOPIS-75) calibrated to absolute values. *In* Channell, J.E.T., Kent, D.V., Lowrie, W., and Meert, J.G. (Eds.), *Timescales of the Paleomagnetic Field.* Geophysical Monograph, 145:255–266. **http://dx.doi.org/10.1029/145GM19**

Laj, C., Kissel, C., Mazaud, A., Channell, J.E.T., and Beer, J., 2000. North Atlantic palaeointensity stack since 75 ka (NAPIS-75) and the duration of the Laschamp Event. *Philosophical Transactions of the Royal Society, A: Mathematical, Physical & Engineering Sciences,* 358(1768):1009–1025. **http://dx.doi.org/10.1098/rsta.2000.0571**

Lazarus, D., Spencer-Cervato, C., Pika-Biolzi, M., Beckmann, J.P., von Salis, K., Hilbrecht, H., and Thierstein, H., 1995. *Technical Note, 24: Revised chronology of Neogene DSDP holes from the world ocean.* Ocean Drilling Program. **http://dx.doi.org/10.2973/odp.tn.24.1995**

Lourens, L., Hilgen, F., Shackleton, N.J., Laskar, J., and Wilson, D., 2004. The Neogene period. *In* Gradstein, F.M., Ogg, J.G., and Smith, A. (Eds.), *A Geologic Time Scale 2004:* Cambridge, United Kingdom (Cambridge University Press), 409–440. **http://dx.doi.org/10.1017/CBO9780511536045.022**

Lurcock, P.C., and Wilson, G.S., 2012. PuffinPlot: a versatile, user-friendly program for paleomagnetic analysis. *Geochemistry, Geophysics, Geosystems,* 13(6):Q06Z45. **http://dx.doi.org/10.1029/2012GC004098**

MacKenzie, W.S., Donaldson, C.H., and Guilford, C., 1982. *Atlas of Igneous Rocks and Their Textures:* Essex, United Kingdom (Longman Group UK Limited).

Manheim, F.T., and Sayles, F.L., 1974. Composition and origin of interstitial waters of marine sediments, based on deep sea drill cores. *In* Goldberg, E.D. (Ed.), *The Sea* (Volume 5): *Marine Chemistry: The Sedimentary Cycle:* New York (Wiley), 527–568.

Marsaglia, K., Milliken, K., and Doran, L., 2013. *Technical Note 1: IODP digital reference for smear slide analysis of marine mud—Part 1: Methodology and atlas of siliciclastic and volcanogenic components.* Integrated Ocean Drilling Program. **http://dx.doi.org/10.2204/iodp.tn.1.2013**

Marsaglia, K., Milliken, K., Leckie, R.M., Tentori, D., and Doran, L., 2015. *Technical Note 2: IODP smear slide digital reference for sediment analysis of marine mud, Part 2: Methodology and atlas of biogenic components.* International Ocean Discovery Program. **http://dx.doi.org/10.2204/iodp.tn.2.2015**

Mazzullo, J., and Graham, A.G. (Eds.), 1988. *Technical Note 8: Handbook for shipboard sedimentologists.* Ocean Drilling Program. **http://dx.doi.org/10.2973/odp.tn.8.1988**

McFadden, P.L., and Reid, A.B., 1982. Analysis of paleomagnetic inclination data. *Geophysical Journal of the Royal Astronomical Society,* 69(2):307–319. **http://dx.doi.org/10.1111/j.1365-246X.1982.tb04950.x**

Mulder, T., and Alexander, J., 2001. The physical character of subaqueous sedimentary density flows and their deposits. *Sedimentology,* 48(2):269–299. **http://dx.doi.org/10.1046/j.1365-3091.2001.00360.x**

Murray, R.W., Miller, D.J., and Kryc, K.A., 2000. *Technical Note 29: Analysis of Major and Trace Elements in Rocks, Sediments, and Interstitial Waters by Inductively Coupled Plasma–Atomic Emission Spectrometry (ICP-AES).* Ocean Drilling Program. **http://dx.doi.org/10.2973/odp.tn.29.2000**

Nigrini, C., and Moore, T.C., Jr., 1979. A Guide to Modern Radiolaria. *Special Publication - Cushman Foundation for Foraminiferal Research*, 16. **http://www.cushmanfoundation.org/specpubs/sp16.pdf**

Nigrini, C., and Sanfilippo, A., 2001. *Technical Note 27: Cenozoic radiolarian stratigraphy for low and middle latitudes with descriptions of biomarkers and stratigraphically useful species.* Ocean Drilling Program. **http://dx.doi.org/10.2973/odp.tn.27.2001**

Nigrini, C., Sanfilippo, A., and Moore, T.C., Jr., 2006. Cenozoic radiolarian biostratigraphy: a magnetobiostratigraphic chronology of Cenozoic sequences from ODP Sites 1218, 1219, and 1220, equatorial Pacific. *In* Wilson, P.A., Lyle, M., and Firth, J.V. (Eds.), *Proceedings of the Ocean Drilling Program, Scientific Results,* 199: College Station, TX (Ocean Drilling Program), 1–76. **http://dx.doi.org/10.2973/odp.proc.sr.199.225.2006**

O'Dogherty, L., Carter, E.S., Dumitrica, P., Goriččan, Š., De Wever, P., Bandini, A.N., Baumgartner, P.O., and Matsuoka, A., 2009. Catalogue of Mesozoic radiolarian genera. Part 2: Jurassic–Cretaceous. *Geodiversitas,* 31(2):271–356. **http://dx.doi.org/10.5252/g2009n2a4**

ODP Information Technology and Data Services, 2007. *Technical Note 37: ODP prime scientific data: collection, archive, and quality.* Ocean Drilling Program. **http://dx.doi.org/10.2973/odp.tn.37.2007**

Pälike, H., Norris, R.D., Herrle, J.O., Wilson, P.A., Coxall, H.K., Lear, C.H., Shackleton, N.J., Tripati, A.K., and Wade, B.S., 2006. The heartbeat of the Oligocene climate system. *Science,* 314(5807):1894–1898. **http://dx.doi.org/10.1126/science.1133822**

Pearson, P.N., Olsson, R.K., Hemleben, C., Huber, B.T., and Berggren, W.A., 2006. Atlas of Eocene planktonic foraminifera. *Special Publication - Cushman Foundation for Foraminiferal Research,* 41.

Perch-Nielsen, K., 1985a. Cenozoic calcareous nannofossils. *In* Bolli, H.M., Saunders, J.B., and Perch-Nielsen, K. (Eds.), *Plankton Stratigraphy:* Cambridge, United Kingdom (Cambridge University Press), 427–554.

Perch-Nielsen, K., 1985b. Mesozoic calcareous nannofossils. *In* Bolli, H.M., Saunders, J.B., and Perch-Nielsen, K. (Eds.), *Plankton Stratigraphy:* Cambridge, United Kingdom (Cambridge University Press), 329–426.

Pessler, R.C., and Fear, M.J., 1992. Quantifying common drilling problems with mechanical specific energy and a bit-specific coefficient of sliding friction [paper presented at the SPE Annual Technical Conference and Exhibition, Washington, DC, 4–7 October 1992]. (Abstract SPE-24584) **http://dx.doi.org/10.2118/24584-MS**

Pickering, K.T., and Hiscott, R.N., 2015. *Deep Marine Systems: Processes, Deposits, Environments, Tectonics and Sedimentation:* Chichester, United Kingdom (Wiley-Blackwell).

Raffi, I., Mozzato, C., Fornaciari, E., Hilgen, F.J., and Rio, D., 2003. Late Miocene calcareous nannofossil biostratigraphy and astrobiochronology for the Mediterranean region. *Micropaleontology,* 49(1):1–26. **http://dx.doi.org/10.2113/49.1.1**

Reagan, M.K., Pearce, J.A., Petronotis, K., Almeev, R., Avery, A.A., Carvallo, C., Chapman, T., Christeson, G.L., Ferré, E.C., Godard, M., Heaton, D.E., Kirchenbaur, M., Kurz, W., Kutterolf, S., Li, H.Y., Li, Y., Michibayashi, K., Morgan, S., Nelson, W.R., Prytulak, J., Python, M., Robertson, A.H.F., Ryan, J.G., Sager, W.W., Sakuyama, T., Shervais, J.W., Shimizu, K., and Whattam, S.A., 2015. Expedition 352 methods. *In* Reagan, M.K., Pearce, J.A., Petronotis, K., and the Expedition 352 Scientists, *Izu-Bonin-Mariana Fore Arc.* Proceedings of the International Ocean Discovery Program, 352: College Station, TX (International Ocean Discovery Program). **http://dx.doi.org/10.14379/iodp.proc.352.102.2015**

Richter, C., Acton, G., Endris, C., and Radsted, M., 2007. *Technical Note 34: Handbook for Shipboard Paleomagnetists.* Ocean Drilling Program. **http://dx.doi.org/10.2973/odp.tn.34.2007**

Rider, M.H., 1996. *The Geological Interpretation of Well Logs* (2nd edition): Caithness, Scotland (Whittles Publishing).

Robaszynski, F., Caron, M., Gonzales-Donoso, J.-M., Wonders, A.A.H., and the European Working Group on Planktonic Foraminifera, 1984. Atlas of Late Cretaceous globotruncanids. *Revue de Micropaleontologie,* 26(3–4):145–305.

Rothwell, R.G., 1989. *Minerals and Mineraloids in Marine Sediments: An Optical Identification Guide:* London (Elsevier).

Sanfilippo, A., and Nigrini, C., 1998. Code numbers for Cenozoic low latitude radiolarian biostratigraphic zones and GPTS conversion tables. *Marine Micropaleontology,* 33(1–2):109–117, 121–156. **http://dx.doi.org/10.1016/S0377-8398(97)00030-3**

Sanfilippo, A., Westberg-Smith, M.J., and Riedel, W.R., 1985. Cenozoic Radiolaria. *In* Bolli, H.M., Saunders, J.B., and Perch-Nielsen, K. (Eds.), *Plankton Stratigraphy* (Vol. 2): *Radiolaria, Diatoms, Silicoflagellates, Dinoflagellates, and Ichthyoliths:* Cambridge, UK (Cambridge University Press), 631–712.

Schlumberger, 1989. *Log Interpretation Principles/Applications:* Houston (Schlumberger Education Services), SMP–7017.

Schrader, H.-J., 1974. Cenozoic marine planktonic diatom stratigraphy of the tropical Indian Ocean. *In* Fisher, R.L., Bunce, E.T., et al., *Initial Reports of the Deep Sea Drilling Project,* 24: Washington, DC (U.S. Government Printing Office), 887–967. **http://dx.doi.org/10.2973/dsdp.proc.24.122.1974**

Schmitt, D.R., Currie, C.A., and Zhang, L., 2012. Crustal stress determination from boreholes and rock cores: fundamental principles. *Tectonophysics,* 580:1–26. **http://dx.doi.org/10.1016/j.tecto.2012.08.029**

Serra, O., 1984. *Fundamentals of Well-Log Interpretation* (Volume 1): *The Acquisition of Logging Data:* Amsterdam (Elsevier).

Serra, O., 1986. *Fundamentals of Well-Log Interpretation* (Volume 2): *The Interpretation of Logging Data:* Amsterdam (Elsevier).

Shepard, F.P., 1954. Nomenclature based on sand-silt-clay ratios. *Journal of Sedimentary Research,* 24(3):151–158. **http://dx.doi.org/10.1306/D4269774-2B26-11D7-8648000102C1865D**

Shipboard Scientific Party, 1993. Explanatory notes. *In* Gillis, K., Mével, C, Allan, J., et al., *Proceedings of the Ocean Drilling Program, Initial Reports,* 147: College Station, TX (Ocean Drilling Program), 15–42. **http://dx.doi.org/10.2973/odp.proc.ir.147.102.1993**

Stoner, J.S., Laj, C., Channell, J.E.T., and Kissel, C., 2002. South Atlantic and North Atlantic geomagnetic paleointensity stacks (0–80 ka): implications for inter-hemispheric correlation. *Quaternary Science Reviews,* 21(10):1141–1151. **http://dx.doi.org/10.1016/S0277-3791(01)00136-6**

Takahashi, K., 1991. *Radiolaria: Flux, Ecology, and Taxonomy in the Pacific and Atlantic.* Ocean Biocoenosis Series, 3. **http://hdl.handle.net/1912/408**

Tauxe, L., Tucker, P., Peterson, N.P., and LaBrecque, J.L., 1984. Magnetostratigraphy of Leg 73 sediments. *In* Hsü, K.J., LaBrecque, J.L., et al., *Initial Reports of the Deep Sea Drilling Project,* 73: Washington, DC (U.S. Government Printing Office), 609–621. **http://dx.doi.org/10.2973/dsdp.proc.73.123.1984**

Teale, R., 1965. The concept of specific energy in rock drilling. *International Journal of Rock Mechanics and Mining Sciences & Geomechanics Abstracts,* 2(1):57–73. **http://dx.doi.org/10.1016/0148-9062(65)90022-7**

Terry, R.D., and Chilingar, G.V., 1955. Summary of "Concerning some additional aids in studying sedimentary formations," by M. S. Shvetsov. *Journal of Sedimentary Research,* 25(3):229–234. **http://jsedres.geoscienceworld.org/cgi/content/abstract/25/3/229**

Thibault, N., Husson, D., Harlou, R., Gardin, S., Galbrun, B., Huret, E., and Minoletti, F., 2012. Astronomical calibration of upper Campanian–Maastrichtian carbon isotope events and calcareous plankton biostratigraphy in the Indian Ocean (ODP Hole 762C): implication for the age of the Campanian–Maastrichtian boundary. *Palaeogeography, Palaeoclimatology, Paleoecology,* 337–338:52–71. **http://dx.doi.org/10.1016/j.palaeo.2012.03.027**

Toumarkine, M., and Luterbacher, H., 1985. Paleocene and Eocene planktic foraminifera. *In* Bolli, H.M., Saunders, J.B., and Perch-Nielsen, K. (Eds.), *Plankton Stratigraphy:* Cambridge, United Kingdom (Cambridge University Press), 87–154.

Vacquier, V., 1985. The measurement of thermal conductivity of solids with a transient linear heat source on the plane surface of a poorly conducting body. *Earth and Planetary Science Letters,* 74(2–3):275–279. **http://dx.doi.org/10.1016/0012-821X(85)90027-5**

Valet, J.-P., Meynadier, L., and Guyodo, Y., 2005. Geomagnetic dipole strength and reversal rate over the past two million years. *Nature,* 435(7043):802–805. **http://dx.doi.org/10.1038/nature03674**

van Hinsbergen, D.J.J., de Groot, L.V., van Schaik, S.J., Sparkman, W., Biji, P.K., Sluijs, A., Langeris, C.G., and Brinkhuis, H., 2015. A paleolatitude calculator for paleoclimate studies. *PLoS One,* 10(6):e0126946. **http://dx.doi.org/10.1371/journal.pone.0126946**

Vandenberghe, N., Hilgen, F.J., and Speijer, R.P., 2012. The Paleogene Period. With contribution by J.G. Ogg, F.M. Gradstein, O. Hammer, Hollis C.J., and J.J. Hooker. *In* Gradstein, F.M., Ogg, J.G., Schmitz, M.D., and Ogg, G.M. (Eds.), *The Geological Time Scale 2012:* Amsterdam (Elsevier), 855–921. **http://dx.doi.org/10.1016/B978-0-444-59425-9.00028-7**

Vasiliev, M.A., Blum, P., Chubarian, G., Olsen, R., Bennight, C., Cobine, T., Fackler, D., Hastedt, M., Houpt, D., Mateo, Z., and Vasilieva, Y.B., 2011. A new natural gamma radiation measurement system for marine sediment and rock analysis. *Journal of Applied Geophysics,* 75:455–463. **http://dx.doi.org/10.1016/j.jappgeo.2011.08.008**

Wade, B.S., Pearson, P.N., Berggren, W.A., and Pälike, H., 2011. Review and revision of Cenozoic tropical planktonic foraminiferal biostratigraphy and

calibration to the geomagnetic polarity and astronomical time scale. *Earth-Science Reviews,* 104(1–3):111–142. **http://dx.doi.org/10.1016/j.earscirev.2010.09.003**

Warren, T.M., 1981. Drilling model for soft-formation bits. *Journal of Petroleum Technology,* 33(6):963–970. **http://dx.doi.org/10.2118/8438-PA**

Waughman, R.J., Kenner, J.V., and Moore, R.A., 2002. Real-time specific energy monitoring reveals drilling inefficiency and enhances the understanding of when to pull worn PDC bits [paper presented at the IADC/SPE Drilling Conference, Dallas, Texas, 26–28 February 2002]. (Abstract SPE-74520-MS) **http://dx.doi.org/10.2118/74520-MS**

Wentworth, C.K., 1922. A scale of grade and class terms for clastic sediments. *Journal of Geology,* 30(5):377–392. **http://dx.doi.org/10.1086/622910**

Yamazaki, T., and Oda, H., 2005. A geomagnetic paleointensity stack between 0.8 and 3.0 Ma from equatorial Pacific sediment cores. *Geochemistry, Geophysics, Geosystems,* 6(11):Q11H20. **http://dx.doi.org/10.1029/2005GC001001**

Zijderveld, J.D.A., 1967. AC demagnetization of rocks: analysis of results. *In* Collinson, D.W., Creer, K.M., and Runcorn, S.K. (Eds.), *Methods in Palaeomagnetism:* Amsterdam (Elsevier), 254–286.